



FLEXIBLE OPTICAL CROSS-CONNECT NODES ENABLING NEXT GENERATION FLEXIBLE OPTICAL NETWORKING

FP7-ICT-GA 318415

SPECIFIC TARGETED RESEARCH PROJECT (STREP) INFORMATION & COMMUNICATION TECHNOLOGIES (ICT)



Flexible transceiver subsystems: Alternative designs, characteristics, specifications and comparison

D3.5

Document Type: Deliverable
Dissemination Level: PU¹
Lead Beneficiary: ETH
Contact Person: Juerg Leuthold Leuthold@ethz.ch
Delivery Due Date: 31/10/2014
Submission date: 25/03/2015
Contributing institutes: ETHZ, Tyndall-UCC, ASTON, FT
Authors: Benedikt Baeuerle bbaeuerle@ethz.ch
Arne Josten ajosten@ethz.ch
Jian Zhao
Erwan Pincemin
Son Thai Le
Mary Mc.Carthy
T. Kanesan
S. Sygletos

¹ PU = Public

PP = Restricted to other programme participants (including the Commission Services)

RE = Restricted to a group specified by the consortium (including the Commission Services)

CO = Confidential, only for members of the consortium (including the Commission Services)

A. D. Ellis

Reviewers: José M. Rivas-Moscoso jmrivas@ait.gr (AIT)

Shalva Ben-Ezra (Finisar)

shalva.ben-ezra@finisar.com

Abstract

This deliverable covers the description of the different flexible transceiver subsystems. We will cover latest results and also give an insight into alternative designs that came up while developing the transceiver subsystems and techniques under investigation.

The FOX-C Project Consortium

No	Partner Name	Short Name	Country
1	OPTRONICS TECHNOLOGIES A.B.E.T.E.	OPTRONICS	Greece
2	FINISAR ISRAEL LTD	FINISAR	Israel
3	W-ONE SYS SL	WONE	Spain
4	FRANCE TELECOM SA	FT	France
5	RESEARCH AND EDUCATION LABORATORY IN INFORMATION TECHNOLOGIES	AIT	Greece
6	THE HEBREW UNIVERSITY OF JERUSALEM	HUJI	Israel
7	EIDGENOESSISCHE TECHNISCHE HOCHSCHULE ZURICH	ETH	Switzerland
8	UNIVERSITY COLLEGE CORK, NATIONAL UNIVERSITY OF IRELAND, CORK	Tyndall-UCC	Ireland
9	ASTON UNIVERSITY	ASTON	United Kingdom

“The research leading to these results has received funding from the European Community's Seventh Framework Program (FP7/2007-2013) under grant agreement n° 318415”.

Table of Contents

Executive Summary	4
1 Introduction.....	6
2 Transmission Formats and Discussion of Measurement Results	8
2.1 Optical Multiplexing without Spectral Overlap	8
2.1.1 Nyquist WDM	8
2.1.2 Nyquist FDM	11
2.1.3 Real-Time DSP for NWDM/NFDM Receiver	14
2.1.4 Electrical Fast OFDM	20
2.1.5 Multi-Band OFDM.....	25
2.1.6 Offset-QAM OFDM	29
2.1.7 References.....	38
2.2 Advanced Transceiver Technologies for CO-OFDM Super-Channels	40
2.2.1 Non-Rectangular Perfect Reconstruction of Pulse Shaping Based ICI Reduction in CO-OFDM	40
2.2.2 Comparison of Bit Error Rate Estimation Methods for QPSK CO-OFDM Transmission	48
2.2.3 Decision-Directed-Free Blind Phase Noise Estimation for CO-OFDM	53
2.2.4 Quasi-Pilot Aided Phase Noise Estimation for CO-OFDM Systems	56
2.2.5 Phase-Conjugated Pilots for Fiber Nonlinearity Compensation.....	63
2.2.6 References.....	73
3 Summary and Conclusions	78

Executive Summary

In this deliverable we present the characteristics of the transceiver subsystems which have been investigated in work package three (WP3). We summarize the respective designs and specifications and compare the different parameters.

For the characterization of the Nyquist wavelength division multiplexing (N-WDM) transceiver subsystem we performed back to back measurements with different noise loading in order to analyze the resilience to additive white Gaussian noise (AWGN). Additionally, we compared implementations with different pulse shapes. We used square root raised cosine (SRRC) pulse shaped signal and varied the roll-off factor (ROF) between 0.05 and 0.25. An increasing roll-off factor leads to a more relaxed signal to noise ratio (SNR) penalty. However, an increasing ROF is accompanied by a decreasing spectral efficiency (SE). Furthermore, we characterized the N-WDM transceiver subsystem with different symbol rates and modulation formats. The measurements show that higher order modulation formats like 16QAM suffer more from an increasing symbol rate than QPSK. This is due to the limited effective number of bits (ENOB) of the digital to analog (D/A) and analog to digital (A/D) converters at higher frequencies.

The Nyquist frequency division multiplexing (N-FDM) transceiver subsystem was also characterized concerning its resilience to AWGN. We demonstrated the transceiver with five sub-channels. The performance of the individual sub-channel decreases with higher frequencies because of the system's low pass characteristic. Different modulation formats have been utilized as well. Additionally, we developed an alternative design with asynchronous sub-channel spacing in order to achieve a flexible operation scheme. Sub-channels with smaller bandwidth suffer more from the crosstalk of neighboring channels.

We presented the results of a newly developed phase recovery algorithm and characterized it concerning laser phase noise (LPN), implementation parameters and AWGN. The real-time implementation on a field-programmable gate array (FPGA) chip shows practicability for symbol rates of up to 38 GBd. We also discuss our implementation for a real-time timing recovery. Here an adaptive resampling filter is used in combination with Gardner timing recovery to correct wrong sampling phases.

For the characterization of the fast orthogonal frequency division multiplexing (F-OFDM) transceiver subsystem, we investigated multi-tap equalization to enhance its performance. It is shown in a 16-QAM F-OFDM system with 1020-km SMF transmission that this technique can exhibit significant benefits in a continuous-mode optical system using low-cost lasers, including improved receiver sensitivity and reduced overhead for the carrier frequency offset (CFO) estimation. It is also shown that multi-tap equalization is more effective in optical F-OFDM than in conventional OFDM (C-OFDM) for the CFO mitigation, implying that optical F-OFDM may be a more potential multicarrier solution for wavelength-selective optical packet networks.

We also evaluated the robustness of 200 Gbit/s coherent 16QAM MB-OFDM to practical implementation impairments, and proved that these impairments are fully manageable in practice by measuring an extra-OSNR implementation penalty of 0.8 dB only in BtB with respect to theory between 100 Gbit/s QPSK-OFDM and 200 Gbit/s 16QAM-OFDM. Likewise, we have also demonstrated the ability of legacy fiber infrastructures to carry 200 Gbit/s 16QAM-OFDM over ~1000 km of uncompensated transmission links equipped with EDFA only. This work has also inspired a contribution given recently in the carriers group of Optical InternetWorking Forum (OIF) promoting the advantages of MB-OFDM for 400 Gbit/s WDM transmission.

In section 2.1.6 we present offset-QAM OFDM as an alternative design for a flexible transceiver subsystem.

Section 2.2 is focused on advanced transceiver technologies for coherent optical orthogonal frequency division multiplexing (CO-OFDM) super-channels. A number of topics have been investigated.

In section 2.2.1 we propose a new pulse shaping method, which achieves suppression of the residual carrier frequency offset induced penalty at the receiver without requiring any additional overhead and

exhaustive signal processing. The Q-factor improvement contributed by the proposed method is 1.6 dB and 1.8 dB for time-frequency localization maximization and out-of-band energy minimization pulse shapes, respectively. The transmission span gain under the influence of residual carrier frequency offset is ~62% with out-of-band energy minimization pulse shape.

Section 2.2.2 is an experimental study on the statistical properties of a received QPSK modulated signal, where we compare various bit error rate (BER) estimation methods for CO-OFDM transmission. We show that BER estimation method based on the probability density function of the received QPSK symbols offers the most accurate estimate of the system performance.

Due to the long symbol duration CO-OFDM is sensitive to laser phase noise, which changes rapidly symbol-by-symbol. The impact of laser phase noise will introduce both common phase error (CPE) and intercarrier interference, which significantly degrades the system performance. Therefore, it is crucial that the laser phase noise is rigorously tracked, estimated and effectively compensated. In section 2.2.3 we demonstrate an effective decision-directed-free blind phase noise compensation method for CO-OFDM transmission. By applying this technique, the CPE can be accurately estimated using as few as three test phases.

In section 2.2.4 a novel phase noise estimation scheme is proposed for CO-OFDM systems: the quasi-pilot aided method. In this method the phases of transmitted pilot subcarriers are deliberately correlated to the phases of data subcarriers. Accounting for this correlation in the receiver allows the required number of pilots needed for a sufficient estimation and compensation of phase noise to be reduced by a factor of 2 in comparison with traditional pilot-aided phase noise estimation method. We carried out numerical simulation of a 40 Gbit/s single polarization transmission system, and the outcome of the investigation indicates that by applying quasi-pilot aided phase estimation, only 4 pilot subcarriers (PS) are needed for effective phase noise compensation. Experimental results have confirmed that by setting PSs in correlation with data subcarriers the overhead of pilot aided carrier phase estimation may be reduced by a factor of 2 for two different correlation techniques, conjugated pilots and phase parity pilots.

Finally in section 2.2.5 we demonstrate a novel fiber nonlinearity compensation technique for CO-OFDM systems based on the transmission of phase-conjugated pilots (PCPs). In this scheme, a portion of OFDM subcarriers (up to 50%) is transmitted with its phase-conjugates, which is used at the receiver to estimate the nonlinear distortions in the respective subcarriers and other subcarriers, which are not accompanied by PCPs. Simulation and experimental results show that, by varying the PCP overhead a performance improvement of up to 4 dB can be achieved. In addition, the proposed technique can be effectively applied in both single polarization and polarization division multiplexed (PDM) systems, in both single channel and wavelength division multiplexing (WDM) systems, thus, offering highest flexibility in implementations.

1 Introduction

As an introduction we will offer a short overview of the different multiplexing schemes and modulation formats of FOX-C, graphically summarized in Figure 1.1, in order to classify the different transceiver subsystems, which will be discussed in this report.

The green labeled schemes are grouped as different optical multiplexing systems, the blue labeled schemes as electrical multiplexing systems and the orange labeled schemes as single carrier modulation formats. The different flexible transceiver subsystems which will be discussed in this deliverable are summarized in the level 1 stage of Figure 1.1. We can distinguish between two groups of subsystems. The first group of subsystems is used for optical multiplexing without spectral overlap (level 2) and is presented in section 2.1. The second group of subsystems is used for optical multiplexing with spectral overlap (level 2) and is presented in section 2.2. The multiplexing scheme without spectral overlap is utilized with four different transceiver subsystems. One subsystem is the N-FDM transceiver, which exploits additionally electrical multiplexing and QAM modulation formats. A further subsystem is Nyquist WDM (N-WDM) which exploits in level 1 dual quadrature QAM with spectral shaping and in level 2 optical multiplexing without spectral overlap. In this report we consider only its single carrier characteristics. In deliverable D5.2 we will embed this subsystem in a WDM system and further analyze it. The two subsystems which utilize electrical OFDM multiplexing with spectral overlap in level 1 are electrical fast OFDM (F-OFDM) and conventional electrical OFDM (C-OFDM). In this report the electrical OFDM transceiver will be even investigated as a multi-band OFDM (MB-OFDM) subsystem. Additionally, we suggested an alternative design called offset-QAM OFDM in section 2.1.6. The second group of optically multiplexed schemes is coherent optical OFDM (CO-OFDM) multiplexing with spectral overlap. It is presented in section 2.2. Here we consider an optical fast OFDM scheme with single quadrature PAM as modulation format and an optical OFDM scheme with dual quadrature QAM.

Level 3:
Fiber link
Multiples of Tbits/s

Level 2:
Super-Channel
10s of Gb/s to 1Tb/s

Level 1:
Band (Flex-Channel)
few Gb/s to 100Gb/s

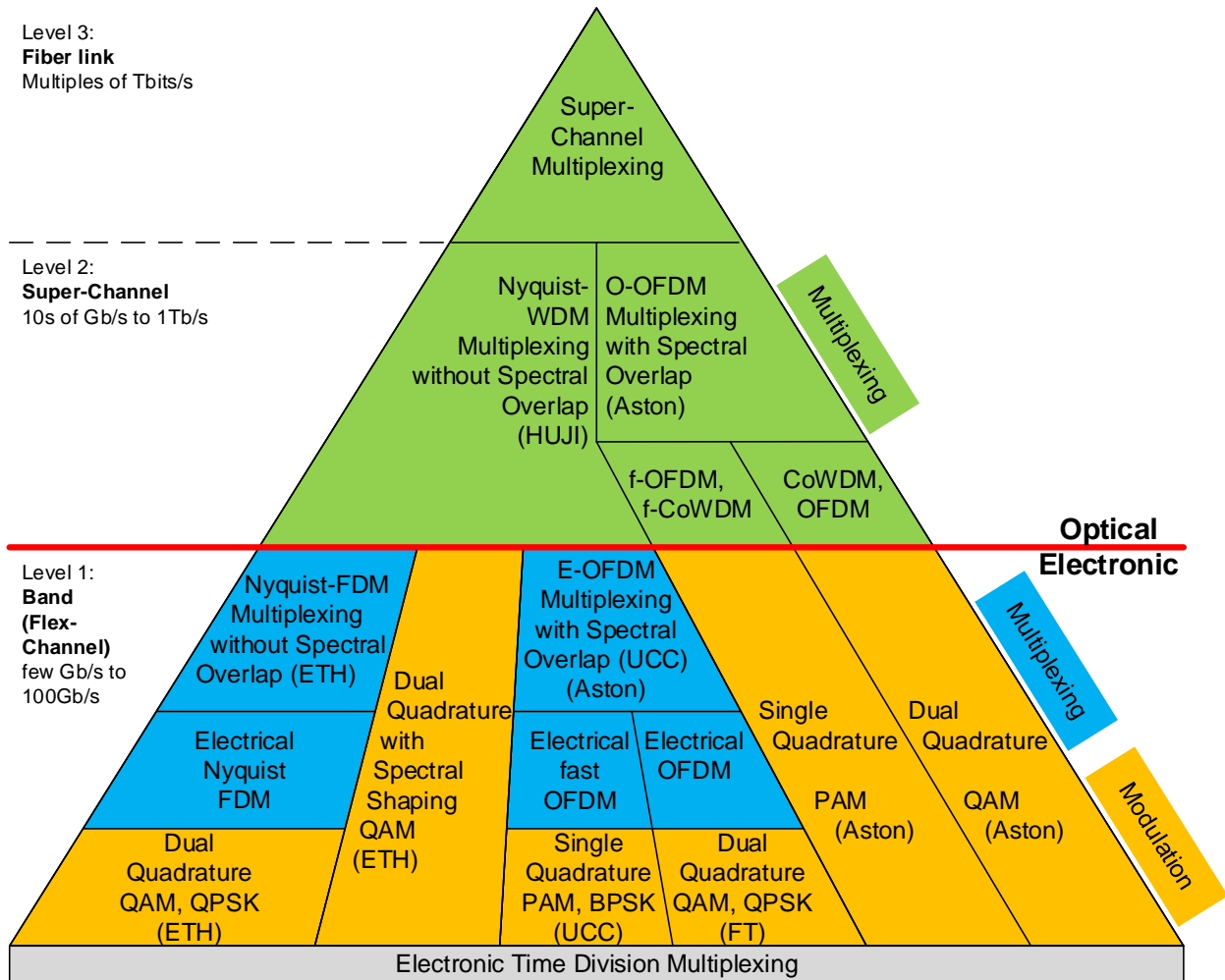


Figure 1.1: Overview of multiplexing schemes investigated in Fox-C (in green) and the targeted modulation formats.

2 Transmission Formats and Discussion of Measurement Results

2.1 Optical Multiplexing without Spectral Overlap

In this section we describe the transceiver subsystems which will be combined with optical multiplexing without spectral overlap. Firstly, we describe Nyquist WDM (N-WDM) and Nyquist FDM (N-FDM). In this deliverable N-WDM will be treated as an optical single carrier Nyquist shaped channel. This scheme will be further evaluated in a WDM scheme in WP5. Additionally, we describe the characteristics of our implemented real-time algorithms for the reception of Nyquist shaped signals. The last three transceiver subsystems which will be presented in this section are electrical fast OFDM (F-OFDM), multi-band OFDM (MB-OFDM) and offset-QAM OFDM. In all cases, experimental BER vs signal-to-noise ratio results are presented considering single polarization transmission systems.

2.1.1 Nyquist WDM

The results of the characterization of our N-WDM transceiver subsystem will be discussed in this section. Our subsystem is utilized in a single carrier case during this characterization. In the final experiments it will be integrated in a WDM system. Nyquist shaped signals are inter-symbol interference (ISI) free and in frequency domain they are rectangular shaped and allocate the Nyquist band. A square root raised cosine (SRRC) shaped signal with a roll-off factor (ROF) of zero is equal to a Nyquist shaped signal. A theoretical Nyquist pulse is not causal and therefore cannot be practically implemented. Consequently, we used in our subsystem SRRC shaped signals with ROFs larger than zero. In order to achieve an ISI-free operation we used a SRRC filter as a pulse shaping filter at the transmitter and as matched filter at receiver. With a ROF of 0.05 we are still very close to an ideal Nyquist shaped signal and can therefore achieve almost highest spectral efficiency. Besides that, we used ROFs of 0.125 and 0.25. Additionally, we characterized our N-WDM transceiver subsystem with different modulation formats, such as QPSK and 16QAM, and with different symbol rates, such as 10 GBd, 20 GBd and 28 GBd. This should demonstrate practicability of our subsystem in flexible networks with changing demands. For this deliverable we characterized the subsystem in a back to back and measured under the influence of additive white Gaussian noise (AWGN).

In the following we summarize our characterization setup. More details about the characterization setup can be found in deliverable D3.4.

Our characterization setup consisted of three distinct components: the transmitter, the noise loading stage, and the receiver. The setup is depicted in Figure 2.1

Our transmitter comprises an optical IQ-Mach-Zehnder-modulator (IQ-MZM), an external cavity laser (ECL), an arbitrary waveform generator (AWG) and a polarization division multiplexing emulator (PDME). In our experiments, we used a prototype AWG (Keysight M8195A) as the production unit was delayed. It has a sampling rate of up to 65 GS/s and an analog bandwidth of 20 GHz. Two outputs, each of them differential, generate the in-phase and quadrature component of our complex signal. The transmitter generates optical dual-polarization single carrier signal at 1550nm. The electrical signal can be programmably adapted to different modulation formats (QPSK and 16QAM) and different pulse shapes, which are precalculated with MATLAB.

The noise source generates noise by amplified spontaneous emission (ASE) in an erbium doped fiber amplifier (EDFA). Noise and signal are then combined in a 3dB coupler. One output of the 3 dB coupler is connected to an optical spectrum analyzer (OSA). The OSA was used to determine the OSNR of the signal at the input to the coherent receiver. The second output of the 3 dB coupler is fed into an optical coherent polarization sensitive receiver.

The signal is finally recovered by an optical polarization diverse coherent receiver. The electrical signals are digitized in a real-time oscilloscope with an electrical bandwidth of 33 GHz and a sampling rate of 80 GSa/s. Demodulation is performed offline in digital signal processing on a PC. This comprises filtering, IQ-imbalance compensation, re-sampling, timing recovery, adaptive filtering for polarization de-

multiplexing, frequency offset compensation, phase offset compensation, symbol decision, and bit error ratio (BER) calculation.

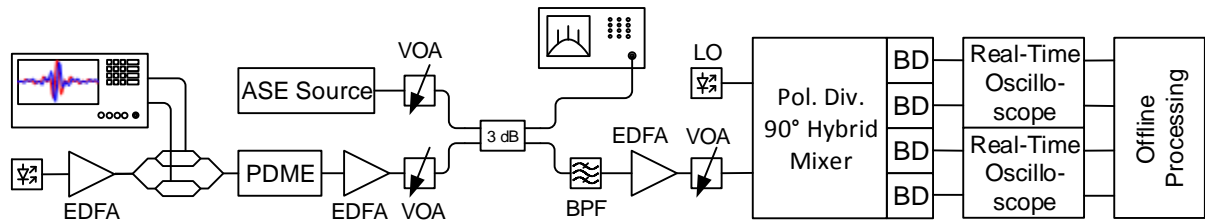


Figure 2.1: Experimental setup: EDFA: Erbium doped fiber amplifier, PDME: Polarization division multiplexing emulator, ASE: Amplified spontaneous emission, VOA: Variable optical attenuator, BPF: Band pass filter, LO: Local oscillator, BD: Balanced detector

The results of the signal-to-noise ratio (SNR) performance measurements are summarized in Figure 2.2 where the BER is plotted as a function of SNR. We characterized our N-WDM transceiver subsystem with three different symbol rates. Figure 2.2 a), b) and c) depict respectively the results for a symbol rate of 10 GBd, 20 GBd and 28 GBd. QPSK and 16QAM have been used as modulation formats. 16QAM has an additional theoretic SNR penalty of 6.8 dB concerning QPSK at a BER of 10^{-3} . Besides, the characterized signals have a SRRC pulse shape with three different ROFs, 0.05, 0.125 and 0.25 respectively. The signal with a ROF of 0.05 can be considered as a practical Nyquist signal. In theory a Nyquist signal is not causal which cannot be implemented practically. The detailed signal parameters can be found in deliverable D3.4. In short, in the case of the 28 GS/s signal a net bit rate of 100Gbit/s for PDM-QPSK and 200 Gbit/s for PDM-16QAM can be achieved considering a data overhead of 12% for FEC.

In Figure 2.2 it can be observed that for a decreasing roll-off factor (from ROF=0.25 to ROF=0.05) the SNR penalty increases for all kinds of signals. In the case of 10 GBd the SNR penalty is between 0.3 dB (ROF: 0.25) and 1.2 dB (ROF: 0.05) for QPSK and between 1 dB (ROF: 0.25) and 2.6dB (ROF: 0.05) for 16QAM. In the case of 20 GBd signals the SNR penalties behaves in similar manner. For QPSK a SNR penalty between 0.7 dB (ROF: 0.25) and 1.7 dB (ROF: 0.05) can be measured and for 16QAM between 1.6 dB (ROF: 0.25) and 2.8 dB (ROF: 0.05). The AWGN resilience for 28 GBd signals with QPSK modulation is similar to the signals with lower symbol rates. But the AWGN resilience for 28 GBd with 16QAM modulation decreases clearly. For QPSK the SNR penalty is between 0.7 dB (ROF: 0.25) and 1.7 dB (ROF: 0.05), and for 16QAM it is between 2.3 dB (ROF: 0.25) and 4.1 dB (ROF: 0.05).

An increasing ROF which goes along with a decreasing spectral efficiency has also a decreasing SNR penalty. This can be understood by an observation of the respective eye diagram (see Figure 2.3). A RC signal with a very small ROF which is close to a Nyquist signal has steeper slopes and therefore a smaller horizontal eye opening than an SRRC signal with a larger ROF. Consequently, sampling with a timing error leads, for RC signals with a smaller ROF, to larger amplitude errors. This is related to the larger SNR penalty for signals with a smaller ROF.

The 16QAM signals suffer much more from an increasing symbol rate than QPSK signals. This is related to the frequency dependent characteristic of the electrical signal generator and detector. Especially, the frequency dependent effective number of bits (ENOB) of the AWG and the oscilloscopes. For higher frequency which goes along with larger symbol rates the ENOB of the AWG and the oscilloscopes decrease. 16QAM signals have four amplitude levels instead of two for QPSK. Consequently, more bits are required to sample 16QAM signals efficiently. To sum up, 16QAM signals suffer more from larger symbol rates because of the limited ENOB at larger frequencies.

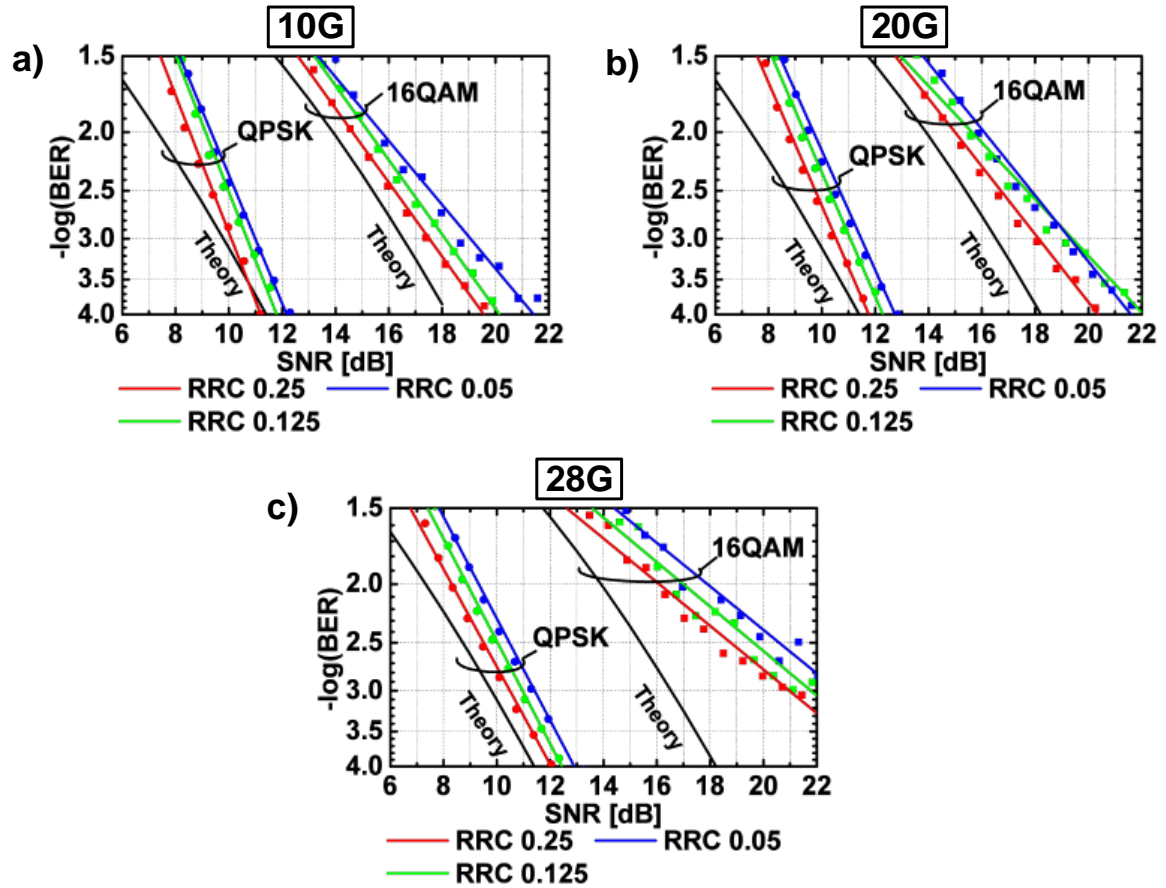


Figure 2.2: Experimental results: $-\log(\text{BER})$ is plotted as a function of SNR. The black curves describe the theoretical BER limit for QPSK and 16QAM for gray-mapping. The signals are square root raised cosine shaped with three different roll-off factors (ROF) and are either modulated with QPSK or 16QAM. Red curves: ROF = 0.25. Green curves: ROF = 0.125. Blue curves: ROF = 0.05. In the different plots measured signals with different symbol rates are depicted: a) 10 GS/s b) 20 GS/s c) 28 GS/s.

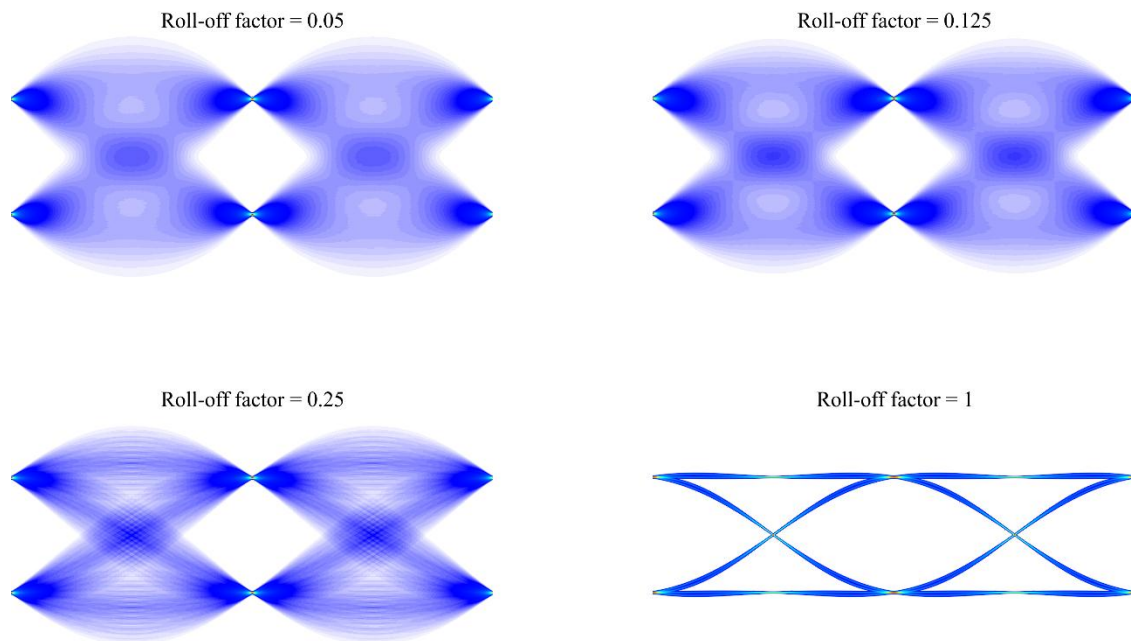


Figure 2.3: Simulation of eye diagrams with different roll-off factors.

2.1.1.1 Discussion

We characterized our N-WDM transceiver subsystem concerning its resilience to AWGN. Additionally, we implemented SRRC signals with different kinds of ROF and different symbol rates. We observed a trade-off between spectral efficiency and AWGN resilience. Instead of using Nyquist shaped pulses it can be also an opportunity to use larger ROFs in order to increase the AWGN resilience. We demonstrated our subsystem with different symbol rates and modulation formats. This can also be implemented in further WDM experiments with asynchronous channels, in order to show its feasibility for flexible and elastic optical networks. We recognized performance losses for 16QAM at larger symbol rates, which is related to the limited ENOB of the D/A and A/D converters at higher frequencies. Consequently we suggest using also 8QAM as an alternative modulation format. The SNR penalty for 8QAM is estimated to be between QPSK and 16QAM. If the SNR penalty is too large to achieve transmission of 16QAM we can additionally switch to 8QAM instead of switching directly to QPSK and losing spectral efficiency. As a further result the granularity of flexibly utilized spectral efficiency in terms of the modulation format can be increased.

Our transceiver subsystem has been demonstrated for flexible networks in terms of versatile modulation formats, symbol rates and ROFs.

In the next steps our N-WDM transceiver subsystem will be integrated in the final test bed at Orange Labs in France. We are then able to test this subsystem in WDM experiment and investigate its behavior under nonlinear impairments in transmission experiments.

2.1.2 Nyquist FDM

N-FDM comprises several digitally multiplexed sub-channels. The different sub-channels are Nyquist shaped and without spectral overlap. Here, we demonstrated, besides standard digitally multiplexing, a full flex-grid operation with N-FDM. This section summarizes the characteristics of our N-FDM subsystem. The results have been published in [1]. We showed high spectral efficiency, asynchronous operation of channels, variable channel loading with different modulation formats and dynamic bandwidth allocation. Data from different sources with different bit and symbol rates are encoded onto electrical Nyquist pulses with different electrical subcarrier frequencies, and then transmitted optically.

We investigated and demonstrated N-FDM with up to 5 independent sub-carriers (SC). All SCs are encoded with Nyquist sinc-shaped pulses, resulting in rectangular non-overlapping spectra, each representing one electrical N-FDM channel. Like OFDM, N-FDM supports variable channel loading, i.e., choosing the channel modulation formats individually. However, N-FDM offers truly independent SCs offering flexible symbol rate per channel. As SC bands are near the fundamental Nyquist limit, no guard bands are required. Synchronization of different transmitters is not required thanks to the non-overlapping spectra. In addition, the narrow shape of each SC offers a high chromatic dispersion (CD) and polarization mode dispersion (PMD) tolerance inside each electrical SC band. As an advantage, no CP is needed for dispersion compensation. Due to the versatility of the concept, both constant and flexible electrical subcarrier grids are supported.

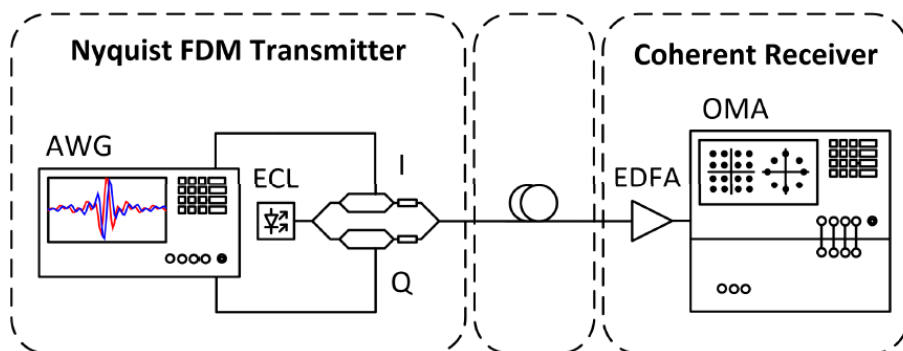


Figure 2.4: Experimental setup to determine the implementation penalties of N-FDM. An arbitrary waveform generator (AWG) drives an optical I/Q-modulator. N-FDM data are encoded on an external cavity laser (ECL), the output of which is amplified by an erbium doped fiber amplifier (EDFA) and coherently received by an optical modulation analyzer (OMA).

A distinct feature of N-FDM is the support of so-called flex-grid operation, i.e., the N-FDM channel position and bandwidth can be chosen at will. In order to demonstrate this capability an aggregate N-FDM signal is created consisting of five individual channels. We first assess the back-to-back performance at high OSNR and demonstrate the feasibility of flex-grid operation within an experiment using the setup of Figure 2.4. We then simulate the performance and depict the bit error ratio (BER) as a function of the SNR per bit [2]. For the experiment and the simulation, the DSP transceivers were implemented using MATLAB. Each of the five channels carries de-correlated pseudo-random binary sequences (PRBS) mapped with either QPSK or 16QAM. The measured channel spectra transporting 16QAM signals are depicted in Figure 2.5(a) along with their back-to-back constellation diagrams. In order to illustrate the flex-grid feature, the N-FDM channels were chosen to have an arbitrary bandwidth and center frequency. The symbol rates are chosen as fraction of the AWG sampling rate 12 GS/s: $f_s/15$ (black), $f_s/32$ (red), $f_s/8$ (green), $f_s/16$ (blue), and $f_s/10$ (cyan). The length of the finite impulse response (FIR) filter's impulse response used for pulse shaping is $L = 128 \times T_s$. We see that the performance of the channel depends on its width. The finite length of the filter results in a non-ideal out-of-band suppression and thus in an overlap with neighboring channels. The smaller the channel is, the larger the de-correlated interchannel interference (ICI) becomes. It can be represented by Gaussian noise and causes the significant increase of the BER for the red channel.

In a next step, the BER of the individual channels as a function of the SNR per bit was determined by simulations. For varying the SNR, AWGN with different power was superimposed to the aggregate N-FDM signal. The results for QPSK and 16QAM modulation formats are shown in Figure 2.5(b). As expected, the SNR per bit is independent of the channel bandwidth, but depends strongly on the modulation format. The experiment as well as the simulation shows that the properties of all the channels can indeed be chosen independently proving that N-FDM offers full flex-grid capability without significant ICI penalties if appropriate FIR filters are used. Still, measurements and simulations differ due to implementation penalties mainly at the receiver in this measurement, causing the increase of BER for the narrow channels.

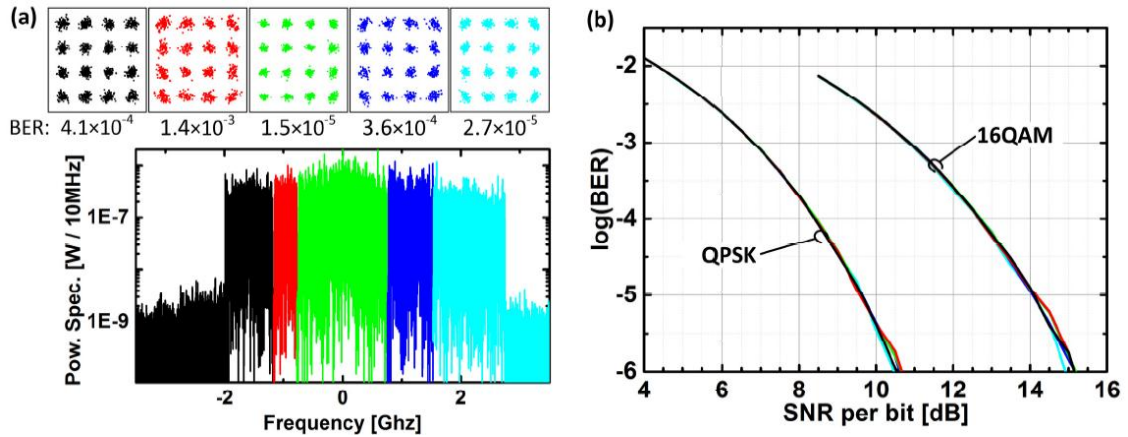


Figure 2.5: Flex-grid scenario of five N-FDM channels with varying bandwidth for transporting 16QAM signals. (a) Lower graph: Measured compound spectrum with color-coded channel spectra. Upper row: Measured back-to-back constellation diagrams and bit error ratio (BER) with identical color coding as the channel spectra. The order R of the filter's impulse response is set to $R=128$ ($R+1=129$ taps). The finite filter order causes channel spectra to overlap, introducing ICI, thus channels have varying performance linked to their spectral width. The smallest channels suffer strongest. (b) Simulated BER for the five channels for QPSK and 16QAM formats as a function of the SNR per bit [2]. As expected, the different color-coded curves virtually coincide. Implementation penalties mainly at the receiver cause the performance difference between experiment and simulation.

In the following we present the results of the performance analysis of an N-FDM signal with five equal channels. An optical coherent receiver is used for achieving the optimum performance.

A coherent receiver enables the reception of complex data encoded by an optical I/Q modulator on an optical carrier, Figure 2.6(a). In this case, upper and lower optical sidebands are uncorrelated and transmit the real (I) and imaginary parts (Q) of complex N-FDM data. The pre-computed signals are stored in two synchronized FPGAs each driving a high-speed Micram DAC. The OSNR is adjusted by a VOA in front of the

EDFA. The OMA coherently receives the N-FDM waveforms. Intradyn reception is performed with OMA-internal ECL used as local oscillator. Further processing is performed offline including BER and error vector magnitude (EVM) assessment. The measured aggregate signal spectrum is depicted in Figure 2.6(b). The signal comprises five independent channels, each having a symbol rate of 3.125 GBd in a 3.125 GHz optical bandwidth. The resulting data rates are $5 \times 3.125 \text{ GBd} \times 2 \text{ bit} = 31.25 \text{ Gbit/s}$ for QPSK, and 62.5 Gbit/s for 16QAM (with 4 bit/symbol), respectively. This corresponds to spectral efficiencies of 2 bit/s/Hz (QPSK) and 4 bit/s/Hz (16QAM). The spectral efficiencies can be doubled if PDM is applied. The roof-shaped spectral roll-off in Figure 2.6(b) is due to the combined electrical frequency responses of Tx and Rx. The roll-off can be compensated at the Tx by a pre-emphasis. Here, we have decided to perform equalization at the Rx instead, for not wasting effective resolution of the DACs to the pre-compensation.

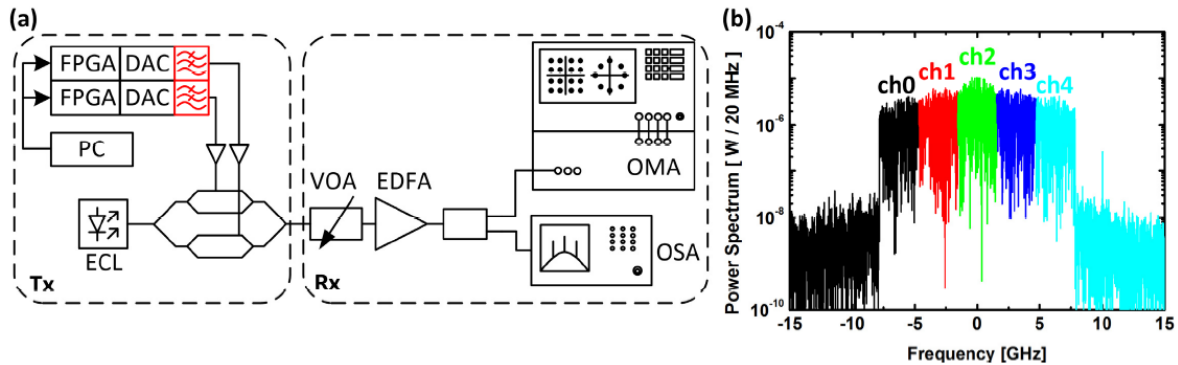


Figure 2.6: Experimental setup and spectra for coherently received N-FDM signals. (a) Experimental setup. Two synchronized FPGAs store pre-computed N-FDM wave-forms. Together with the DACs they again act as an AWG. The amplified outputs drive an optical I/Q-modulator that encodes the waveform onto an ECL. As in the previous setup the OSNR measured by the OSA can be adjusted with a VOA and EDFA pair. The OMA coherently receives and decodes the signals. (b) Measured N-FDM signal spectrum comprising 5 independently modulated channels. The modulation format is either QPSK or 16QAM. The spectral roll-off is due to the combined frequency response of Tx and Rx and can be compensated for by means of a pre-emphasis or equalization. Here it will be equalized in the receiver.

The measured BER (squares) and the equivalent BER obtained from EVM measurements (lines) [3] of QPSK modulated N-FDM signals at different OSNR are depicted in Figure 2.7(a). Channel ch2 located in the center of the spectrum (Figure 2.6(b), green spectrum) performs best as expected, because for this channel the highest SNR is observed since it is not significantly suffering from the roll-off. We virtually find the same performance for corresponding channels (i.e. ch1 and ch3 as well as ch0 and ch4) due to the symmetry of the spectrum resulting in the same SNR. For 16QAM modulated N-FDM signals the BER vs. OSNR results are shown in Figure 2.7(b). The OSNR is once more measured for the total signal, but the BER is determined for each channel individually. Due to the roll-off over the spectrum, the SNR of the center channel is higher than that of the outer channels. Thus we give also the mean BER for comparison. The mean BER is nearly identical to the performance of ch2 and ch3, which is once more due to the roll-off of the spectrum. Again measured BER (squares) and equivalent BER (lines) coincide. An increased error floor is observed. The roll-off could be compensated for by applying a pre-emphasis. However, this pre-emphasis would reduce the ENOB by at least one bit.

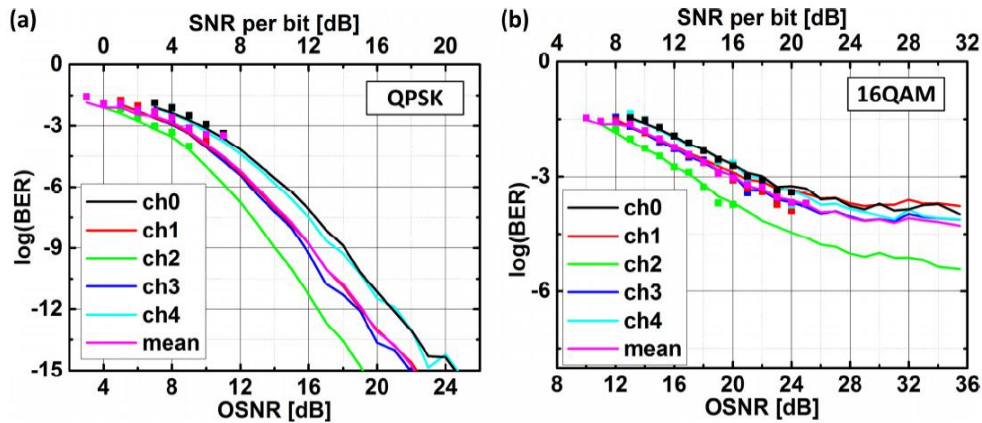


Figure 2.7: Intradyn reception of N-FDM signals. Measured BER (squares) and BER calculated from measured EVM (lines) as a function of OSNR (reference bandwidth 0.1 nm) and SNR per bit of the complete spectrum. All 5 channels are either modulated with (a) QPSK or (b) 16QAM. The center channel (ch2) performs best as it has the highest SNR, see Figure 2.6(b). All measured BER coincide with the equivalent BER obtained from EVM measurements. The OSNR was measured for the complete spectrum, but is not the same for each channel due to the spectral roll-off. The mean BER is depicted as a magenta-colored line for comparison.

2.1.2.1 Discussion

We characterized our N-FDM transceiver subsystem concerning its reliability under the condition of AWGN. Each of the five sub-channels have been analyzed individually in order to demonstrate the feasibility of digital multiplexing. In the case of N-FDM subsystems the outer sub-channels suffer more from the system's low-pass characteristic. However, our N-FDM subsystem offers the utilization of bit loading. Consequently, sub-channels which suffer more from the low-pass characteristic can be modulated with lower-order formats such as QPSK and sub-channels which are close to the optical carrier can be modulated with higher-order formats such as 16QAM. This property of our N-FDM subsystems will be further investigated in deliverable D5.2. In this report we present the subsystem's characteristics either with QPSK or with 16QAM. Furthermore, we utilized an alternative enhanced design for our N-FDM transceiver subsystems which works with asynchronous sub-channels. Each individual sub-channel can exploit a variable bandwidth and channel spacing. In comparison to OFDM it offers an advantage since in OFDM the channel spacing of each sub-carrier needs to be the same. N-FDM with asynchronous sub-channels enables a fine flex-grid operation.

2.1.3 Real-Time DSP for NWDM/NFDM Receiver

In this section we discuss the characteristics of our real-time processing units, which are part of the N-WDM/N-FDM receiver subsystem. The real-time DSP units can be alternatively used in offline DSP done in MATLAB.

The digital part of the receiver with each of its blocks is shown in Figure 2.8. At every clock cycle, a block containing 128 samples, each with real and imaginary parts, is fed into the receiver's DSP unit. After the timing correction block the sampling of the signal can be reduced to one sample per symbol as this is sufficient for the subsequent algorithms for carrier recovery. The carrier recovery is split in two parts, one for phase recovery and one for frequency recovery. Both are performed in polar coordinates. After the signal is recovered from all impairments introduced by the channel, the symbols can be demodulated according to the chosen modulation scheme.

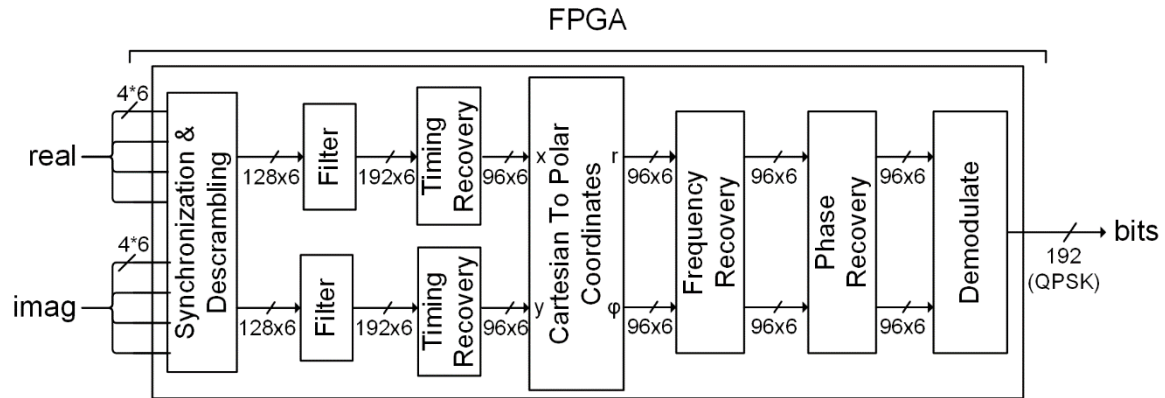


Figure 2.8: Block diagram of the receiver's DSP unit. The input consists of blocks of 128 complex samples with 4/3 samples per symbol. After the timing correction the block contains 96 samples with one sample per symbol. Each sample is 6 bit wide.

In the following sub-sections we will describe in more detail the main blocks of the digital part of the receiver.

2.1.3.1 Timing Recovery Block

The timing recovery block basically consists of four different parts (Figure 2.9). The FIR filter is in charge of resampling the signal according to the current timing correction and has to provide a signal with an oversampling of two samples per symbol in order for the Gardner algorithm to work. This equals to 192 samples for the real as well as the imaginary part. The 2-fold oversampled signal is then fed into the timing estimation block. There it is fed into the Gardner block (timing error detection block), which is calculating the timing estimate either via amplitude or power of the signal. The resulting direction of correction is then averaged (in the averaging block) and used as input to the filter block. At the same time the samples fed into the timing estimation block are resampled to achieve one sample per symbol resulting in 96 samples for both parts. This is done to provide the proper signal for the following blocks.

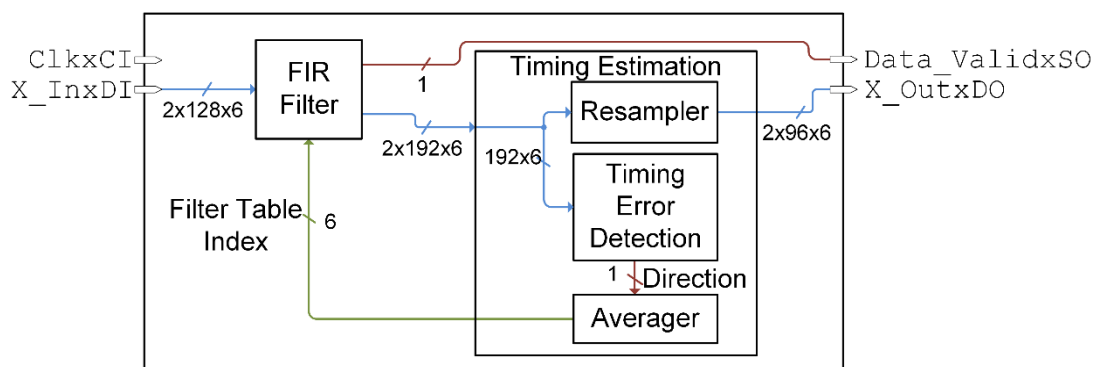


Figure 2.9: Simplified block diagram of the timing recovery block consisting mainly of the filter and the timing error detector.

As can be seen from the block diagram, the timing error detector uses only one part, the real part, of the signal. This is done in order to reduce the used hardware resources.

In the following we will provide a thorough description of the FIR filter block, the timing estimation block and the averaging block.

2.1.3.1.1 FIR filter

The FIR filter block implements the variable filter needed for the resampling with the corrected sampling times and ensures the oversampling needed for the timing error detection algorithm can be adapted. The filter consists of a wrapper which contains the two actual filter instances. The wrapper feeds the real part into one of the instances and the imaginary part into the other one. The block diagram of one filter instance can be seen in Figure 2.10.

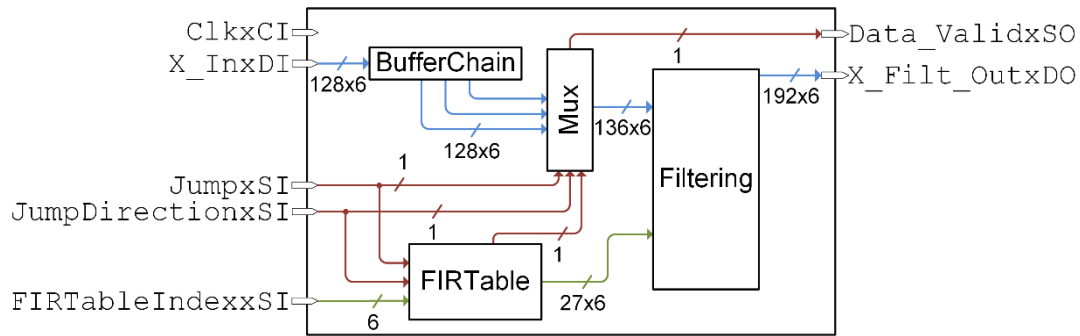


Figure 2.10: Simplified block diagram of the FIR filter. Only important data and control signals are shown.

The input of the filter instances is written into a first in first out (FIFO) like buffer chain. This is done because the filter needs additional samples for buffering. A two stage multiplexer will then choose the needed sample from the buffer chain. For this implementation eight additional samples are used as buffers, four on either side of the block.

Only the entries of the result matrix needed after the division by three are calculated. This can be done because the non-integer oversampling is always the same. Another benefit of doing this is to simplify the optimization process of the synthesis tool. The filter coefficients are taken from the `FIRTable` according to the current correction of the sampling instant.

Besides the input signal the filter needs a filter table index. This index indicates which row of the filter coefficient table should be taken. The filter table consists of all the filter tap coefficients (column wise) for all different possibilities of timing errors (row wise). Because of this structure the FIR table index can also be translated directly to the desired timing correction. The filter is able to resample the signal with correction of the sampling instant between 0.484375 and -0.5 with respect to the sampling period.

2.1.3.1.2 Timing Estimation Block

The timing estimation block includes the timing error detection block. This block either implements the Gardner via amplitude (Figure 2.11) or the Gardner via power (Figure 2.12). In order to enable the implementation on an FPGA, some simplifications have to be made which are discussed in the following paragraphs.

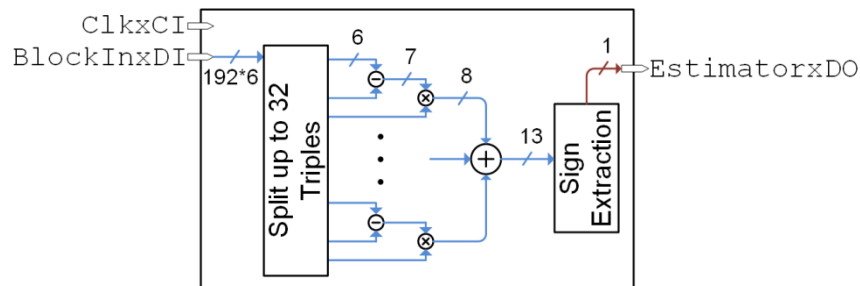


Figure 2.11: Simplified block diagram of the Gardner via amplitude. Out of all possible triples of sample only the first 32 are taken into account for the algorithm. All the weighted differences are then summed up, which is done in an adder tree. At the end the sign of the estimate is extracted and visible at the output. Pipeline registers are not shown for simplification reasons.

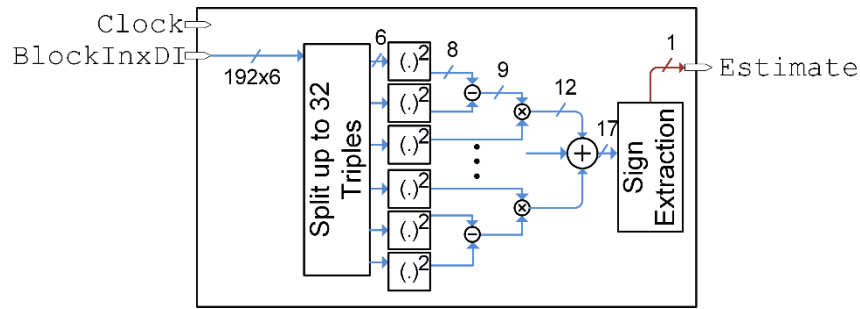


Figure 2.12: Simplified block diagram of the Gardner via power. Out of all possible triples of sample only the first 32 are taken into account for the algorithm. They are then first of all squared. All the weighted differences are then summed up, which is done in an adder tree. Because squaring and weighting includes an additional multiplication, the bitwidth of the signals is larger for this version. At the end the sign of the estimate is extracted and visible at the output. Pipeline registers are not shown for simplification reasons.

Simplify Algorithm

To limit the amount of hardware resources needed, the algorithm does not use all of the samples per block, but uses the first 32 triples instead. This is a tradeoff between the ability of averaging over as many triples as possible and the used resources as well as the performance. The performance of the algorithm was determined with the help of the S-curve. These 32 triples are currently optimized for QPSK modulation and the use of the Gardner via power. For 16-QAM and the Gardner algorithm via amplitude this number needs to be changed to a bigger amount of triples, because more are needed for the averaging.

Only One Bit Output

The output of the Gardner algorithm is basically the direction in which the current sampling instants are shifted as seen from the optimal one. Even though the result of the summation is several bits wide it is only the most significant bit (MSB) that contains valid information. Therefore the output of the block consists only of one bit, the sign bit of the result. A 1 implies that the current sampling instants are left of the optimal ones, i.e. the signal is sampled too early. The correction has to be done in opposite direction therefore. For a 0 the sampling instants are too late and have to be earlier.

Because only the sign bit is important, almost a third of the fractional bits are cut off after each of the multiplications to spare additional resources.

2.1.3.1.3 Averaging Block

The averaging block is used to complete two tasks. On the one hand, as already mentioned, it has to ensure stability within the feedback loop. On the other hand, the block is used to translate the output of the Gardner algorithm into a timing correction with respect to the sampling period. This correction is then used as input for the variable filter. In other words, the averaging block translates the one bit wide output of the Gardner algorithm into a six bit wide correction factor, used by the filter. This is achieved by a weighted cumulative sum, supplemented by an adaptive weight changing.

Weighted Cumulative Sum

The formula of the cumulative sum is quite simple and well known:

$$\varepsilon_{k+1} = \varepsilon_k + \alpha \cdot dir$$

for $k > 0$, where dir is the value of the current output of the Gardner algorithm, α is the weight, ε_k is the cumulative estimate at time k and $\varepsilon_0 = 0$. In other words: the current weight is added or subtracted depending on the sign of the current estimate. This results in a stable ε as long as the mean of dir regarding the last clock cycles is zero.

Adaptive Weight Changing

In order to be able to follow fast changes of the timing error but also stable settlement for non-changing timing errors the weight adapts itself to the situation at hand. To achieve this, the last outputs of the

Gardner algorithm have to be considered. If they are all the same, the loop has not yet settled around the optimal timing instant and the weight can be increased. Toggling outputs on the other hand indicate that the loop is settled at the optimal position and the weight should be decreased to reduce ripples and overshoots. The weight starts at the upper boundary after a reset and the changes in weight are always by a factor of two, as long as the boundaries are not violated.

2.1.3.2 Carrier Phase Recovery

We developed a new carrier phase recovery (CPR) algorithm. In order to implement the algorithm on FPGA chip for a coherent digital real-time receiver we were constrained by hardware resource. Consequently we designed a CPR algorithm which works without multiplication which makes it feasible for a FPGA implementation. Furthermore, we analyzed the performance characteristics of our CPR algorithm. This includes its reliability concerning increasing laser phase noise, additive white Gaussian noise and different modulation formats. Besides, we characterized the algorithm's performance concerning design parameters as processing block length. The results of this section have been published in [4].

Firstly, we start with a little explanation of the algorithm's design. The block diagram of the blind phase search (BPS) multi-format CPR is depicted in Figure 2.13. We use polar coordinates instead of Cartesian [4] in order to implement a multiplier free system. The BPS principle enables a block-by-block and parallelized processing, which facilitates a practical implementation.

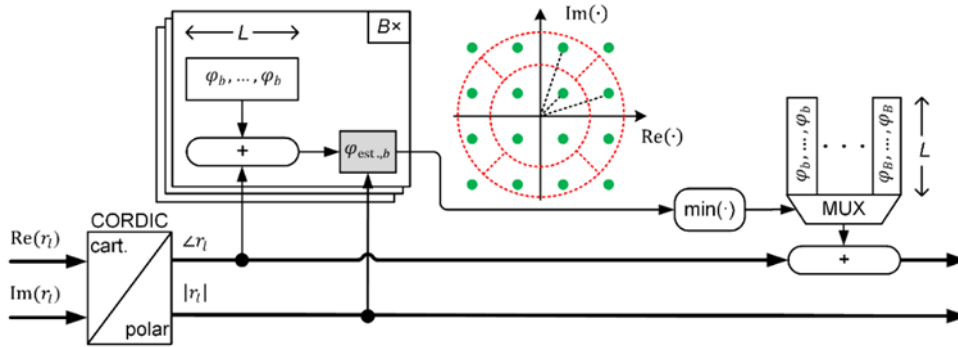


Figure 2.13: Block diagram of the proposed carrier phase recovery (CPR) algorithm consisting of four steps. First, coordinate transformation from Cartesian ($\text{Re}(r_l)$, $\text{Im}(r_l)$) to polar coordinates ($|r_l|$, $\angle r_l$) of L samples by the CORDIC algorithm. Second, parallel summation of B test phases ϕ_b to the received phase $\angle r_l$ and computation of the cost function $\phi_{est,b}$. Third, selection of the smallest cost function $\phi_{est,b}$ to determine the optimum test phase and fourth correction of the received phase $\angle r_l$.

The CPR algorithm corrects the phase offset in four steps. In a first step the Cartesian coordinates of the incoming signal are converted to polar coordinates. Then, test phases are added. Third, the optimum phase is detected and last, the signal phase is corrected. We will now describe this processing blocks in more detail.

In the first step, the received symbols represented by inphase and quadrature component of the received signal (r_l) are converted to polar coordinates with amplitude ($|r_l|$) and phase ($\angle r_l$). The conversion is performed by the CORDIC algorithm [5]. This algorithm avoids multiplications and uses only bit shifts and additions instead. While the phase information is used for processing in all following steps, the amplitude is only needed for the partitioning in the case of 16QAM.

Second, we add a number of B test-phases ($\phi_b = \phi_1, \dots, \phi_B$) to B copies of received phase values ($\angle r_l$) in a block of length L , which results in an amount of $B \cdot L$ estimated phases ϑ_{test} .

Third, we select the correct phase out of all test phases. This is realized through a cost function $\phi_{est,b}$ that performs an averaging over the phase difference to one or multiple reference phases ϕ_{ref} :

$$\varphi_{\text{est},b} = \frac{1}{L} \sum_{l=1}^L (|\vartheta_{\text{test},l,b} - \varphi_{\text{ref}}(|r_l|, \vartheta_{\text{test},l,b})|),$$

$$\text{with } \vartheta_{\text{test},l,b} = \text{mod} \left(\angle r_l + \varphi_b, \frac{\pi}{2} \right)$$

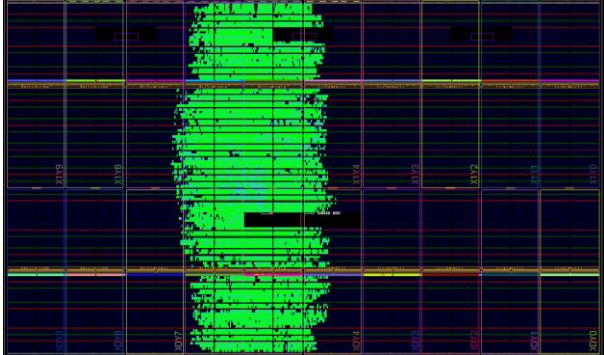
For QPSK, no partitioning is needed and the reference phase is $\varphi_{\text{ref}} = \pi/4$. In the case of 16QAM, the reference phases are $\varphi_{\text{ref}} = \text{atan}(1/3)$, $\pi/4$, $\text{atan}(3/1)$. The reference phase is selected by an amplitude and subsequent phase partitioning as illustrated in Figure 2.13. First, a decision is made if the symbols are part of the inner, middle, or outer ring. For the middle ring a second stage phase decision with a threshold of $(\pi/4)$ is needed. As we use a block length of $L = 2^n$, the phase estimate can be calculated by additions and bit-shifting only. For a correct estimate, an average over a sufficiently long sequence of symbols is needed. Higher order modulation formats require larger blocks due to their reduced phase noise tolerance. For the correct carrier phase, $\varphi_{\text{est},b}$ is minimized.

In the final step, the carrier phase is corrected by adding the selected test phase to the received phase value. As all values are available in polar coordinates, this can be realized with minimum effort.

Real-time Implementation

We implemented the proposed CPR in VHDL and synthesized the design in order to evaluate the hardware consumption on an FPGA chip. The hardware design processes 128 complex symbols during each clock cycle, so no oversampling is used for our CPR stage. Each symbol has a bit resolution of 6 bit. The design has been optimized for a maximum clock rate of 300 MHz according to the synthesizing tool (Xilinx Vivado). According to the timing analysis, a signal with a maximum symbol rate of 38.4 Gbd can be processed. The FPGA used in our simulations and experiments is a Xilinx Virtex 7. The hardware requirements for the full system for QPSK signals with a window length of 32 are presented Tab. 1. The implementation utilizes no DSP units as expected.

Tab. 1. FPGA chip utilization (% of Xilinx xc7vx690t).

Visualized chip utilization	Hardware Design	Clock frequency	Slice LUT	Slice Registers	DSPs
	QPSK, Window Length: 32	300 MHz	50181 (11.58%)	59197 (6.83%)	0 (0%)
	QPSK, Window Length: 64	300 MHz	49286 (11.37%)	58735 (6.77%)	0 (0%)

Simulation Results and Analysis

We studied the performance of our proposed algorithm by MATLAB simulations. We modeled AWGN and combined laser phase noise (LPN) from the transmitter and receiver as impairment factors. The LPN has been modeled as suggested in [6]. To focus on the limiting factors of the CPR, other impairments like timing offset, frequency offset, chromatic dispersion, and polarization mode dispersion were excluded from the simulation. The simulation was performed with a PRBS sequence of length $2^{15} - 1$, which is repeated multiple times to generate a sequence with more than 10^5 symbols. The algorithm has been analyzed for QPSK and 16QAM. The Simulation results are depicted in Figure 2.14.

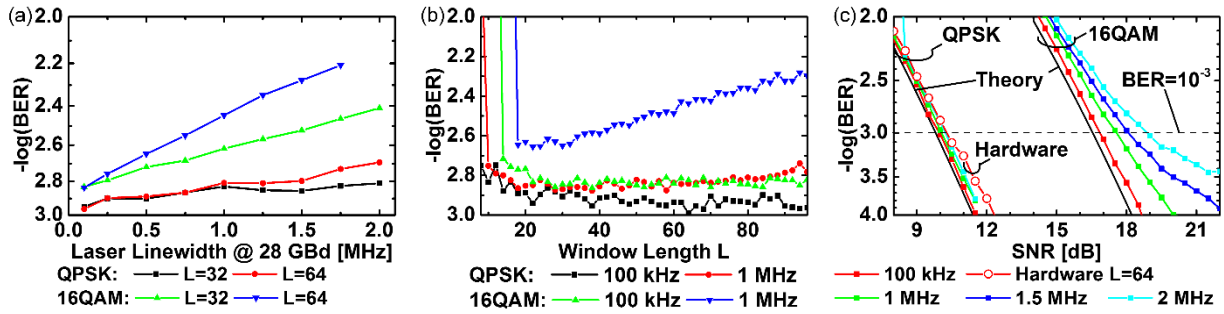


Figure 2.14: Simulation results. (a) BER over laser linewidth for symbol rate of 28 GBd for different modulation formats and window lengths. (b) BER over window length for QPSK and 16QAM and laser linewidth of 100 kHz and 1 MHz. (c) BER over SNR for QPSK and 16 QAM. MATLAB simulation and hardware implementation results are shown together with the theoretical limit.

Figure 2.14a shows the BER results under the condition of different laser linewidths for a 28 GBd signal at the SNR theoretically required for a BER of 10^{-3} . It can be seen that the signals with larger window lengths L are more affected by larger LPN. Figure 2.14b shows the influence of the window length L on the algorithm performance for a 28 GBd signal at the SNR theoretically required for a BER of 10^{-3} . Depending on the laser linewidth, different window lengths offer advantages in performance. For low LPN, long window lengths L are beneficial, as AWGN related errors average out. For larger LPN, shorter window lengths L are required because here the phase development due to LPN would have a big influence on too long windows. Since the influence of LPN does not average out like in the case of AWGN. For the smallest window lengths, the algorithm is unable to calculate any reliable result as the AWGN cannot be reduced by averaging anymore. We consider a window length of 32 and 64. Subsequently, we studied the reliability of our hardware implementation and the SNR penalty compared to the MATLAB simulations. The results are depicted in Figure 2.14c.

To verify the algorithm for its performance in hardware, the design for QPSK was tested with ModelSim. The robustness of the carrier phase estimation (CPE) was tested by adding AWGN and LPN to a 28 GBd signal. As a result an SNR penalty at a BER of 10^{-3} of 0.5 dB was found for a combined laser linewidth of 100 kHz.

2.1.3.3 Discussion

We developed and implemented a new algorithm for the phase recovery in digital real-time receiver. The algorithm is optimized for low complexity and its implementation on an FPGA chip. The entire chain of phase recovery avoids multiplication in order to save important hardware resources which are required for other algorithms on the same FPGA chip. The algorithm has been characterized concerning combined LPN and processing block length. Besides, we tested the algorithm's resilience to AWGN. The CPR algorithm is implemented on a FPGA chip and tested under the influence of AWGN. The characterization has proven its practicability for a real-time implementation for symbol rate up to 38 GBd.

2.1.4 Electrical Fast OFDM

The implementation principle of F-OFDM has been reported in D.3.1 and D.3.4. In this report, we improve the performance by using multi-tap equalizers at the receiver [7]. A narrow-linewidth laser with excellent frequency stability is firstly used to identify the enhanced tolerance to CFO and phase noise using multi-tap equalization. Then, a system using commercial lasers with a wider linewidth is investigated. It is shown that multi-tap equalizers can greatly improve the receiver sensitivity and reduce the overhead for CFO estimation in a continuous-mode optical system. Transmission over 1020-km SMF was successfully demonstrated.

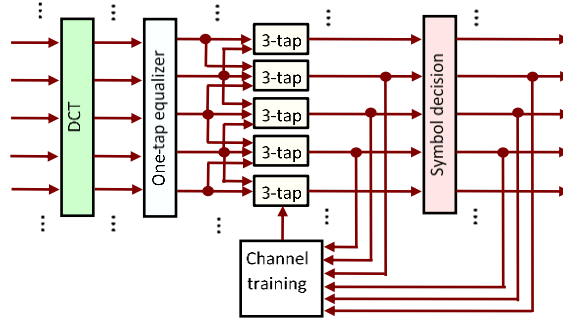


Figure 2.15: Configuration of F-OFDM decoding with three-tap equalizers

Figure 2.15 depicts an example of decoding with three-tap equalizers. In conventional F-OFDM, one-tap equalizers are commonly used after subcarrier demultiplexing (i.e. discrete cosine transform, DCT) to compensate the channel response [8]. In the investigated system, frequency-domain multi-tap equalizers are employed to improve the system performance. Assuming that the inputs of multi-tap equalizers are b_k , the outputs, c_k , are represented as:

$$c_k = \sum_{i=-(m-1)/2}^{(m-1)/2} b_{k-i} q_i \quad m=1, 3, 5... \quad (1)$$

where q_i and m are the coefficients and the number of taps, respectively. The initial value of q_i can be obtained by re-using the training sequence for channel estimation. These coefficients are updated using the least-mean-square algorithm during the signal detection process:

$$q_i^{k+1} = q_i^k + \Delta \cdot \sigma_i^{k+1} \quad \sigma_i^{k+1} = 0.5 \times \sigma_i^k + 0.5 \times (a_{est,k} - c_k) \cdot b_{k-i} \quad (2)$$

where σ_i^{k+1} represents the mean square error, and the convergence parameter Δ is optimized and set to be 0.0005 in the off-line processing. $a_{est,k}$ is the decoded data and can be replaced by a_k in the training sequence at the initial stage.

Figure 2.16 shows the experimental setup. Two bi-polar four-amplitude-shift-keying (4-ASK) data sequences were encoded with Gray coding in Matlab. The inverse-DCT (IDCT) and DCT used 256 points, of which 200 subcarriers were used for data modulation. The subcarriers in the zero-frequency region were not modulated, allowing for AC-coupled amplifiers and insertion of pilot tones for phase estimation. The last 40 subcarriers were zero-padded to avoid aliasing. After IDCT and parallel-to-serial (P/S) conversion, 16 samples were added to each symbol as a symmetric-extension based guard interval (GI). The peak-to-average power ratio was controlled to be 11 dB by clipping. The generated signal was downloaded to a 12-GS/s arbitrary waveform generator (AWG). The signal rate including the GI and forward error correction overhead was ~ 38 Gbit/s.

Two types of lasers with different levels of frequency stability were used in the experiments. The first type of lasers had a 5-kHz laser linewidth while the second type had a 100-kHz laser linewidth and less frequency stability (± 60 MHz per minute and ± 300 MHz per day). Two 4-ASK electrical F-OFDM signals were fed into the in-phase and quadrature arms of a 10-GHz optical I/Q modulator to generate an optical 16QAM F-OFDM signal. The input signals had a peak-to-peak driving swing of $0.5 V_\pi$ to reduce the nonlinear effect. The generated optical signal was amplified by an erbium doped fiber amplifier (EDFA), filtered by a 0.8-nm optical band-pass filter (OBPF), and transmitted over a re-circulating loop comprising 60-km single-mode fiber (SMF) with 15-dB fiber loss. The noise figure of the EDFA was 5 dB and another 0.8-nm OBPF was used in the loop to suppress the amplified spontaneous emission noise. The launch power per span was optimized to be -8 dBm.

At the receiver, the signal was detected with a pre-amplified coherent receiver, the variable optical attenuator (VOA) was used to vary the optical signal-to-noise ratio (OSNR) for the bit error rate (BER) vs. OSNR measurements. The pre-amplifier was followed by an OBPF with a 3-dB bandwidth of 0.64 nm, a

second EDFA, and another optical filter with a 3-dB bandwidth of 1 nm. A polarization controller (PC) was used to align the polarization of the filtered F-OFDM signal before entering the signal path of a 90° optical hybrid. The optical outputs of the hybrid were connected to two balanced photodiodes with 40-GHz 3-dB bandwidths, amplified by 40-GHz electrical amplifiers, and captured using a 50-GS/s real-time oscilloscope. The off-line algorithms included interpolation, identification of the start-of-frame (SOF) symbol, synchronization, integer and fraction CFO estimation, phase estimation, one-tap equalization for dispersion compensation, and finally multi-tap equalizers.

In all cases, the fraction CFO was estimated based on the Schmidl & Cox algorithm. The integer CFO estimation was integrated to the fine symbol synchronization stage and searched the optimal value in the range of [-2GHz 2GHz]. CFO estimation and synchronization were realized simultaneously using one SOF symbol, with the CFO estimation accuracy similar to the Schmidl & Cox algorithm and the synchronization accuracy of < 2.2 ps for OSNR values as low as 3 dB [9]. On the other hand, phase estimation was realized using pilot tones. When the 5-kHz lasers were applied, the residual effects of CFO and phase noise arising from hardware were small. We then emulated the CFO and phase noise in the offline processing to identify the tolerance to these impairments:

$$r_{n,emulated} = r_n \cdot \exp(j \cdot 2\pi f_{CFO} \cdot T \cdot n + j \cdot \varphi_n) \quad (3)$$

where r_n , f_{CFO} , φ_n are the received time-domain signal in the oscilloscope, the CFO, and the phase noise, respectively. T is the time interval between samples. φ_n was modelled to obtain different laser linewidths.

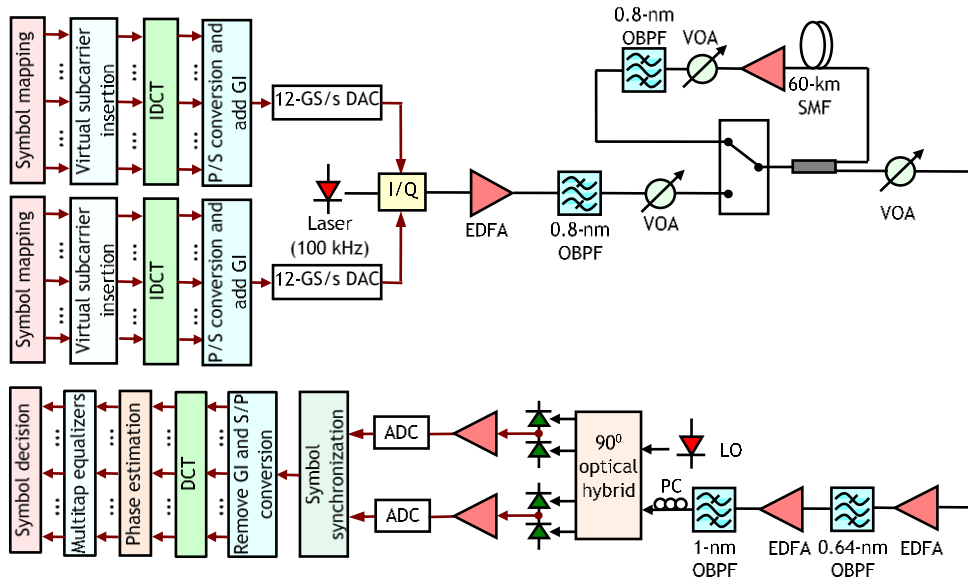


Figure 2.16: Experimental Setup

Figure 2.17(a)-(b) show the performance when the 5-kHz lasers were used and no additional impairments were added in the offline processing. Figure 2.17 (a) depicts the BER versus the number of taps at 0 and 1020 km. It can be seen that the use of multi-tap equalizers can improve the performance somewhat even for near-ideal lasers. This might be attributed to the mitigation of the ICI arising from the nonlinear effects during electrical amplification. The selection of the number of taps depends on a balance between the complexity and performance. In the following discussion, seven taps are selected unless otherwise stated, because it can compensate most of the ICI as will be confirmed later. Figure 2.17 (b) shows the performance versus the received OSNR under -8-dBm signal launch power with one- or seven-tap equalizers. The required OSNR to achieve a BER of 10^{-3} is around 14 dB at 0 km. A slight penalty of < 1 dB is observed after 1020 km. It is also seen that seven-tap equalizers may improve the performance slightly even for near-ideal lasers with compensated CFO and phase noise.

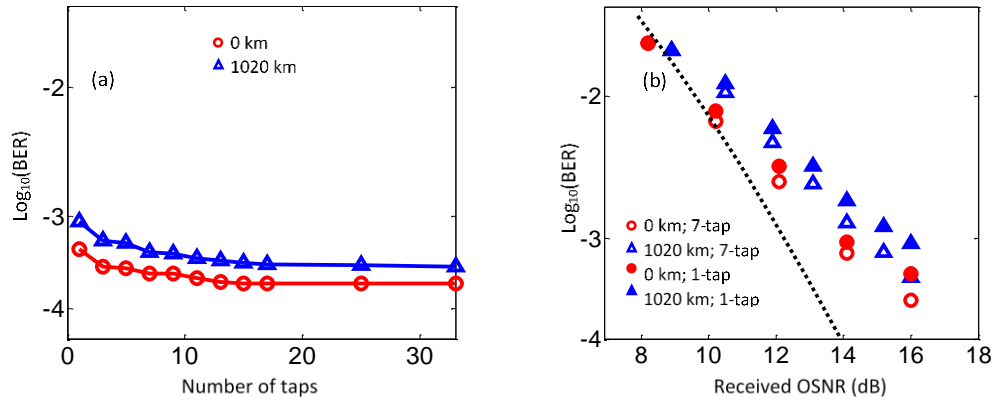


Figure 2.17: (a) BER versus the number of taps. The signal launch power is -8 dBm; (b) BER versus the received OSNR.

Figure 2.18(a)-(d) illustrate the benefits of multi-tap equalizers in the presence of CFO and phase noise. In Figure 2.18, 5-kHz lasers were applied, and the residual CFO and phase noise were added using Eq. (3). Figure 2.18 (a) shows the BER versus f_{CFO}/f_s at 1020 km for different number of taps, where f_s represents the subcarrier spacing. It can be seen that three-tap equalizers can compensate most of the ICI, resulting in significant improvement over one-tap equalizers. Increasing the tap number to five further enhances the tolerance, and the performance becomes stable for seven-tap equalizers. This result agrees with a previous prediction [10], where it was theoretically shown that the CFO-induced ICI in optical F-OFDM was mainly from adjacent subcarriers. Figure 2.18 (b) compares the performance of multi-tap equalizers in C-OFDM and F-OFDM at 1020 km. As predicted, multi-tap equalizers cannot result in significant performance improvement for C-OFDM signals because the ICI is more spread over subcarriers in the presence of the CFO. Instead, the ICI in the optical F-OFDM is more concentrated and seven-tap equalizers can realize a CFO tolerance range more than three times of that of the C-OFDM.

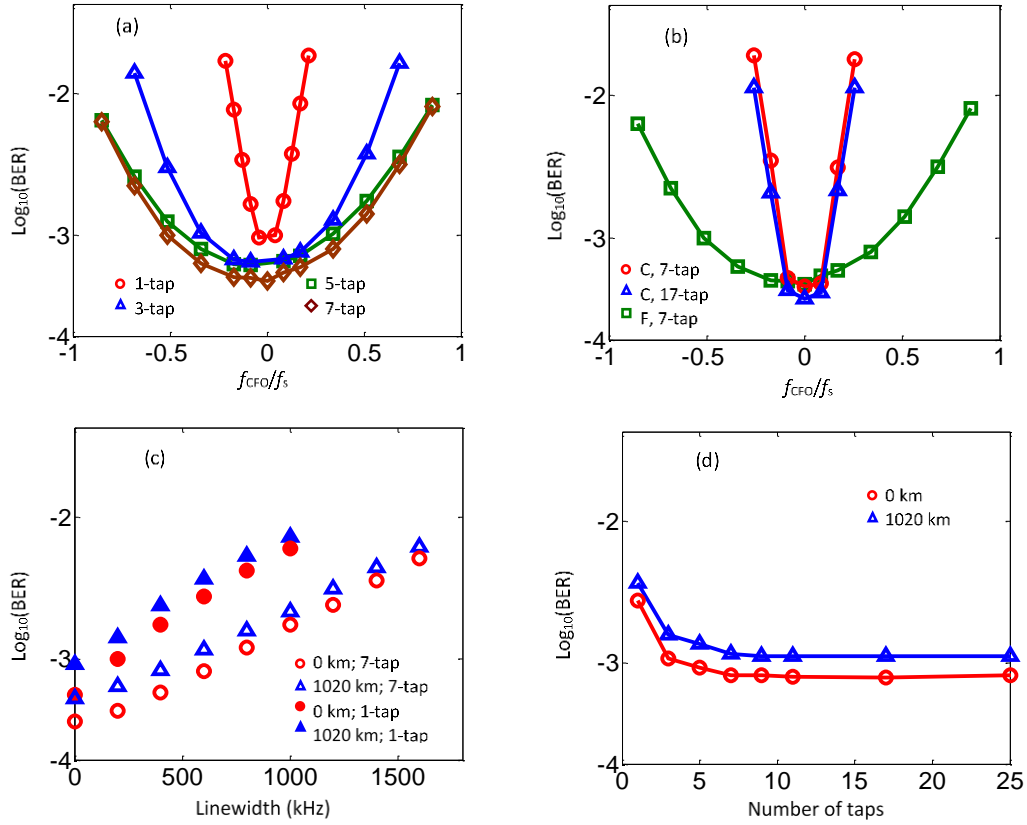


Figure 2.18: (a) BER versus f_{CFO}/f_s at 1020 km. (b) BER versus f_{CFO}/f_s for C-OFDM (C) and F-OFDM (F). (c) BER versus the linewidth of added phase noise at 0 and 1020 km. (d) BER versus the number of taps when the linewidth of added phase noise is 600 kHz. In (a)-(d), the OSNR is 16 dB.

Figure 2.187 (c) shows the performance versus the linewidth of artificially added phase noise for one- and seven-tap equalizers. It is clearly seen that the use of the multi-tap equalizer can also enhance the tolerance to the phase noise. At a BER of 2×10^{-3} , the tolerance ranges under seven-tap equalizers at 0 and 1020 km are around 1000 kHz, 2.5 times of that using one-tap equalizers. Figure 2.187 (d) depicts the performance versus the number of taps at 0 and 1020 km when the linewidth of artificially added phase noise is 600 kHz. Similar to the mitigation of the CFO, three-tap equalizers show the largest performance improvement. A larger number of taps results in better system performance, and seven-tap equalizers can balance the performance and implementation complexity.

Figure 2.18 is based on the use of near-ideal lasers with artificially added CFO and phase noise. In the following, we replaced the 5-kHz lasers with 100-kHz lasers. Figure 2.19(a)-(b) shows the performance versus the received OSNR at 0 and 1020 km when the CFO is estimated every 11.1 μs and 1.8 μs . For each point in the figures, five sets of signals were captured independently from the oscilloscope for BER averaging. In the case of 1.8- μs time interval, the CFO estimation symbol was inserted more frequently in each set of signal, resulting in better tracking of laser frequency drift. From the figure, it can be seen that when the conventional one-tap equalizer is applied, the performance is significantly degraded. For 11.1 μs CFO estimation interval, the BER versus OSNR curve is irregular for high OSNR values. It is because the performance is mainly limited by residual CFO in this region, which is induced by random frequency drift of lasers. Consequently, the BER also fluctuates randomly in the high-OSNR region. When the CFO is estimated more frequently, the effect of frequency drift is mitigated and the performance can be improved. However, there is still a penalty when compared to the case using seven-tap equalizers. Comparison between Figure 2.17(b) and Figure 2.19(a)-(b) shows that this penalty is more prominent for lasers with a wider laser linewidth. It implies that in a continuous-mode optical communication system, multi-tap equalization can obtain significant performance benefits when lower-cost lasers are employed.

The last conclusion we may draw from Figure 2.19 (a)-(b) is that the performance of multi-tap equalization is not sensitive to the estimation interval, and the cases with 11.1- μ s and 1.8- μ s estimation intervals exhibit almost the same performance.

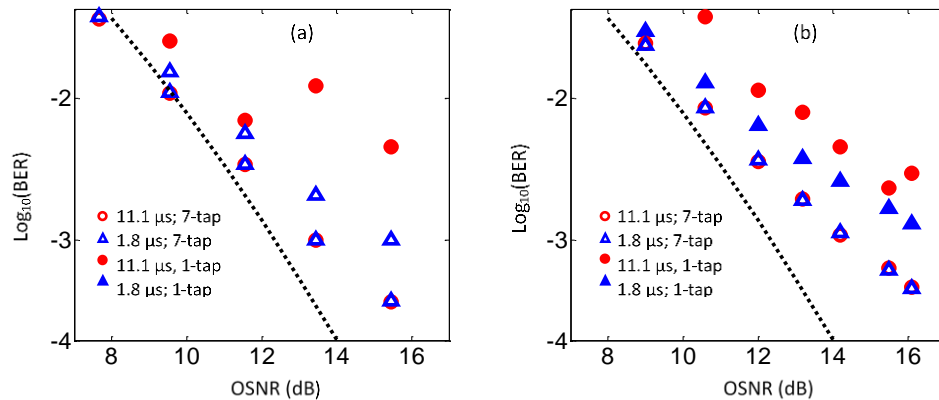


Figure 2.19: BER versus received OSNR at (a) 0 km and (b) 1020 km when the CFO is estimated every 11.1 μ s and 1.8 μ s.

2.1.4.1 Discussion

In this report, we have investigated multi-tap equalization to enhance the performance of the F-OFDM systems. It is shown in a 16-QAM F-OFDM system with 1020-km SMF transmission that this technique can exhibit significant benefits in a continuous-mode optical system using low-cost lasers, including improved receiver sensitivity and reduced overhead for the CFO estimation. It is also shown that multi-tap equalization is more effective in F-OFDM than in C-OFDM for the CFO mitigation, implying that F-OFDM may be a more potential multicarrier solution for wavelength-selective optical packet networks.

2.1.5 Multi-Band OFDM

Equipment suppliers presently propose 200 Gbit/s coherent WDM interfaces to operators in order to improve by a factor of two the spectral efficiency of WDM links in existing optical transport networks. The upgrade from 100 Gbit/s to 200 Gbit/s is obtained by means of coherent dual-polarization 16QAM (DP-16QAM) single-carrier modulation operating at 32 Gbaud [11]. Unfortunately, the transmission performance of these 200 Gbit/s WDM interfaces is severely impaired not only by the high sensitivity of 16QAM to accumulation of amplified spontaneous emission (ASE) noise and fiber nonlinearities, but also by the physical limitations of hardware (HW) components [12]. In particular, the low 3dB-bandwidth (~ 15 GHz), the limited vertical resolution ($\text{ENOB} \sim 4$ bits at 15 GHz) of digital-to-analog converters (DAC) [13], as well as the linearity defaults of the RF driver response significantly impact the performance of the commercially available 200 Gbit/s WDM interfaces, resulting in a maximum reach of 400-500 km only [14-16] when erbium-doped fiber amplifiers (EDFA) are used. These limitations prevent the adoption of 200 Gbit/s WDM interfaces by operators whose primary concern is to reuse at 200 Gbit/s the existing G.652 (standard single mode) / G.655 (non-zero dispersion shifted) fiber-based meshed optical transport networks, over which WDM links frequently reach distances of 1000 km and beyond.

In this deliverable, we experimentally investigate the capability of coherent Multi-Band OFDM (MB-OFDM) [17] to carry 200 Gbit/s DP-16QAM over legacy long-haul G.652/G.655 fiber-based transport networks. After back-to-back characterization of our transmitter/receiver, we show that properly-designed 200 Gbit/s 16QAM-MB-OFDM can reach typical transmission distances of ~ 1000 km over uncompensated G.652 or G.655 fiber lines equipped with EDFA only.

The experimental transmission test-bed is depicted in Figure 2.20. The WDM transmitter consists of one 100 Gbit/s or 200 Gbit/s dual-polarization MB-OFDM (DP-MB-OFDM) channel at 1552.52 nm carrying QPSK or 16QAM, and 59 other channels ranging from 1533.86 nm to 1557.36 nm on the 50 GHz ITU grid and modulated at 100 Gbit/s by dual-polarization QPSK (DP-QPSK). Note that 100 Gbit/s QPSK-OFDM is

taken here as a reference for our experiments. As shown in Figure 2.20.a), the MB-OFDM signal is constituted of four sub-bands spaced by 10 GHz with a guard-band of 2 GHz between them. Each sub-band has 256 subcarriers, covers a bandwidth of 8 GHz, and carries a net bit-rate of 25 Gbit/s (resp. 50 Gbit/s) when modulated with QPSK (resp. 16QAM). Overheads for soft-decision FEC (20 %), cyclic prefix (7%), training symbols and pilot tones (3%) increase the data rate to 32.5 Gbit/s (for QPSK) or 65 Gbit/s (for 16QAM) in each sub-band. The DP-MB-OFDM signal has a total bandwidth of 38 GHz, and transports a net bit-rate of 100 Gbit/s (for QPSK) or 200 Gbit/s (for 16QAM). As depicted in Figure 2.20, two arbitrary waveform generators (AWG), each embedding four DACs, are used to generate the four de-correlated OFDM sub-bands. Four 100-kHz linewidth external cavity lasers (ECL) spaced by 10 GHz feed four complex Mach-Zehnder modulators (CMZM), combined together by a polarization-maintaining (PM) coupler. Linear RF amplifiers (SHF 807) are used to drive the CMZMs in the linear regime of their transfer function. A polarization-maintaining EDFA (PM-EDFA) is inserted to compensate for transmitter losses. A polarization-multiplexing unit with one symbol delay between the X and Y polarizations generates the dual-polarization MB-OFDM signal. The 60 channels are then combined together by a wavelength selective switch (WSS) with 50 GHz resolution. The resulting WDM signal spectrum recorded at the transmitter side is shown in Figure 2.20d).

The uncompensated 1000-km transmission line is constituted of ten 100-km spans of G.652 [18] or G.655 fiber [19], whose losses are compensated by single-stage EDFA with 20-dB gain and 4.5-dB noise figure. A dynamic gain equalizer (DGE) is inserted in the middle of the transmission line in order to flatten the multiplex power. The WDM signal spectrum recovered after 1000-km is shown in Figure 2.20.e).

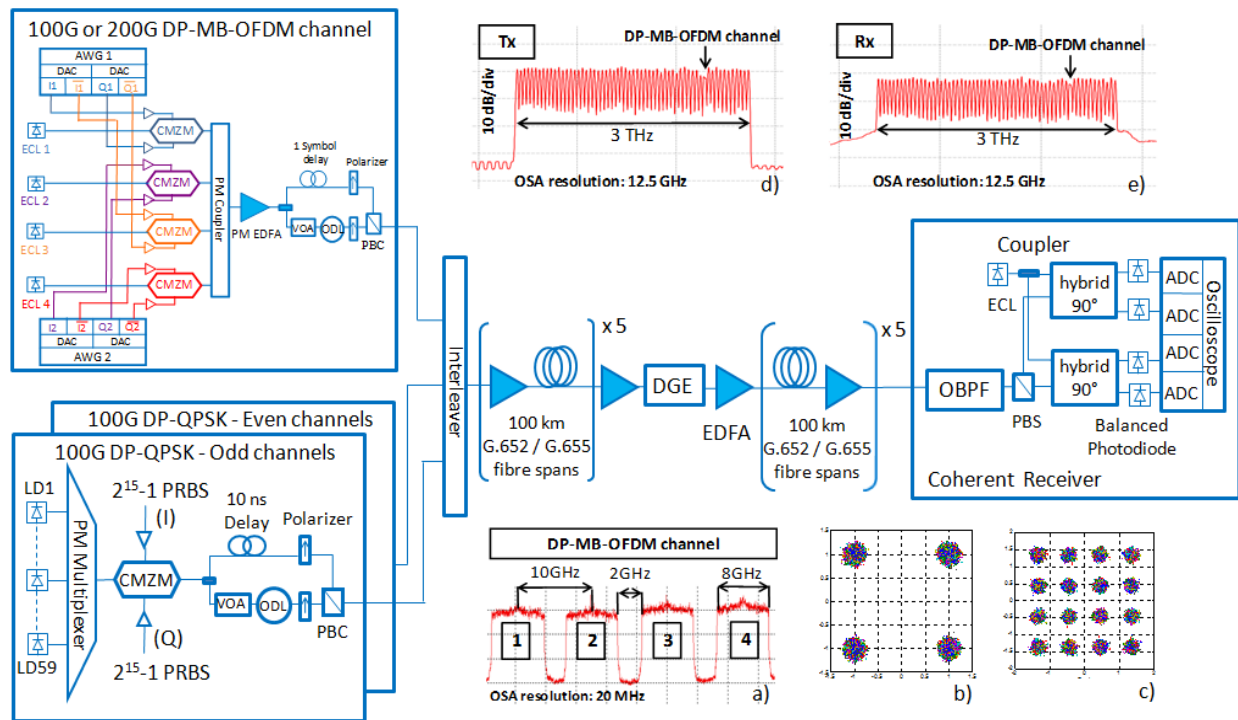


Figure 2.20: Set-up of the 10x100-km transmission test-bed, with the DP-MB-OFDM channel at 1552.52 nm, the 59 odd and even 100 Gbit/s DP-QPSK channels ranged from 1533.86 nm to 1557.36 nm, the 10x100-km uncompensated G.652/G.655 transmission line, and the coherent receiver. In insets, the spectrum and constellations of the QPSK and 16QAM DP-MB-OFDM signal in BtB (a-c), the spectra of the 60 channels at the transmitter side (d) and receiver side after the 1000-km transmission (e).

At the receiver side, the DP-MB-OFDM channel at 1552.52 nm is extracted by a square flat-top optical band-pass filter (OBPF) and detected by a polarization-diversity coherent receiver using a ~100 kHz linewidth ECL as local oscillator. The signal is converted back to the digital domain thanks to a real-time oscilloscope with four 50 GS/s analog-to-digital converters (ADC). "Off-line" digital signal processing (DSP)

at the transmitter/receiver side is performed using Matlab®. Complete description of the algorithms used can be found in [20]. The QPSK-OFDM and 16QAM-OFDM constellations in back-to-back (BtB) without any noise loading are shown in Figure 2.20b) and Figure 2.20c).

To verify that a proper implementation of OFDM can overcome practical HW impairments, bit-error rates (BER) versus optical signal-to-noise ratios (OSNR) are plotted in BtB for 100 Gbit/s QPSK-OFDM and 200 Gbit/s 16QAM-OFDM in Figure 2.21. Noise loading is used to vary the OSNR at the receiver side. An OSNR penalty of 7.8 dB only is measured between 100 Gbit/s QPSK-OFDM (OSNR ~ 14.5 dB @ BER=10⁻³) and 200 Gbit/s 16QAM-OFDM (OSNR ~ 22.3 dB @ BER=10⁻³). This is only 0.8 dB away from theory which predicts a difference of 7 dB. In contrast, 200 Gbit/s single-carrier DP-16QAM show error floor around BER~10⁻⁴ with more than 10 dB OSNR penalty at BER=10⁻³ with respect to coherent 100 Gbit/s single-carrier DP-QPSK modulation [12, 21, 22]. This is a key advantage of the MB-OFDM technique which considerably relaxes the pressure put on the performance of DAC/ADC and analog components when compared to 32 Gbaud single-carrier DP-16QAM. For instance, the required analog bandwidth for MB-16QAM-OFDM in our setting is ~5 GHz only, whereas 32 Gbaud DP-16QAM would need at least 70% of the baud rate, i.e. ~ 22.5 GHz. Identically, the required ENOB of DAC/ADC for 16-QAM is ~6 bits: it is easily achieved when DAC/ADC have ~5 GHz bandwidth but absolutely not when they have bandwidths higher than 15 GHz [13, 23]. This remarkable result proves that HW impairments are fully manageable in practice with 200 Gbit/s 16QAM-OFDM, even if real-time implementation of DSP and use of industrial HW will surely increase the implementation penalty beyond 0.8 dB.

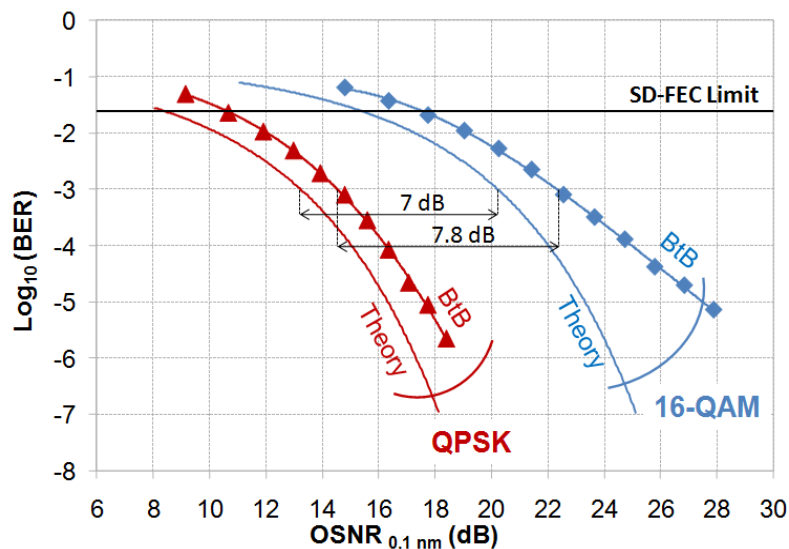


Figure 2.21: BER versus OSNR (in 0.1 nm) given by theory and measured in BtB for 100 Gbit/s QPSK-OFDM and 200 Gbit/s 16QAM-OFDM.

The performance of 200 Gbit/s 16QAM-OFDM is now evaluated over the previously described G.652 or G.655 fiber transmission test-bed. The results are shown in Figure 2.22 for both 100 Gbit/s QPSK-OFDM (used here as a reference) and 200 Gbit/s 16QAM-OFDM. Error-free transmissions with BERs well below the soft-decision FEC (SD-FEC) threshold (fixed here at BER=2x10⁻²) are achieved with 100 Gbit/s QPSK-OFDM over both G.652 and G.655 fibers. Interestingly, the best performance is obtained over the G.652 fiber, with a measured BER at the optimum span input power two decades below the BER obtained with the G.655 fiber (BER~1x10⁻⁷ vs. BER~1x10⁻⁵). Similarly, the optimum input power is larger for the G.652 fiber spans (PIN SPAN ~ 0 dBm) than for the G.655 fiber (PIN SPAN ~ -1.5 dBm). With 200 Gbit/s 16QAM-OFDM, error free transmission is achieved over the G.652 fiber (BER~8x10⁻³) whereas it falls short of the SD-FEC limit over the G.655 fiber (BER ~ 2.3x10⁻²). As for QPSK, the optimum span input power is 1.5 dB higher for the G.652 fiber when compared to the G.655 fiber. Due to its larger chromatic dispersion which fully decorrelates the interacting signals and limits the impact of cross-phase modulation and four-wave mixing, G.652 fiber turns out to be superior to G.655 fiber. Finally, as expected, 100 Gbit/s QPSK-OFDM

largely outperforms 200 Gbit/s 16QAM-OFDM. Nonetheless, we have demonstrated the remarkable results that error-free transmission can be achieved over 1000 km of G.652 fiber with 200 Gbit/s 16QAM-OFDM, while industrial 200 Gbit/s DP-16QAM WDM interfaces usually do not reach more than 400-500 km (with no industrial margin) in field trials using EDFA only [14-16]. Finally, BERs versus OSNRs are plotted for 100 Gbit/s QPSK-OFDM in Figure 2.23 a) and 200 Gbit/s 16QAM-OFDM in Figure 2.23 b) at the optimum span input power. Figure 2.23 shows that transmission penalties after 1000 km do not exceed 1 dB (for a BER= 10^{-3}) with QPSK-OFDM, whereas several decibels are measured with 16QAM-OFDM, thereby confirming the higher sensitivity of 16QAM-OFDM to fiber nonlinearities.

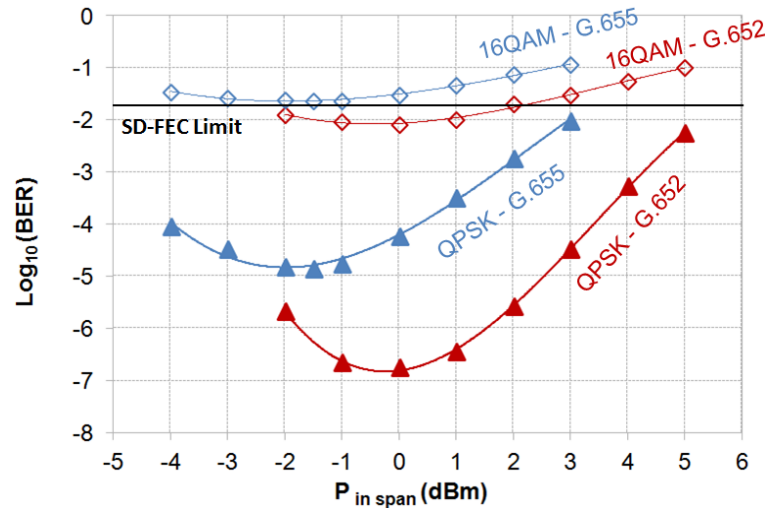


Figure 2.22: BER versus span input power (P IN SPAN) after 1000 km of transmission over G.652 and G.655 fibers (b) for 100 Gbit/s QPSK-OFDM and 200 Gbit/s 16QAM-OFDM.

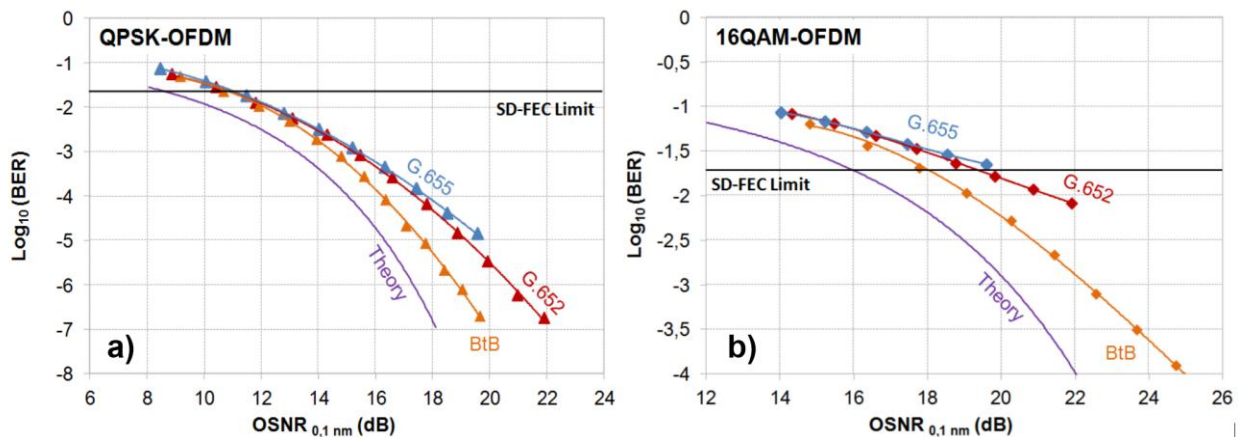


Figure 2.23: : BER versus OSNR (in 0.1 nm) given by theory, measured in BtB and after 1000 km of transmission over G.652 and G.655 fibers at the optimum span input power for 100 Gbit/s QPSK-OFDM (a) and 200 Gbit/s 16QAM-OFDM (b).

2.1.5.1 Discussion

We have evaluated the robustness of 200 Gbit/s coherent 16QAM MB-OFDM to practical implementation impairments, and proved that these impairments are fully manageable in practice by measuring an extra-OSNR implementation penalty of 0.8 dB only in BtB with respect to theory between 100 Gbit/s QPSK-OFDM and 200 Gbit/s 16QAM-OFDM. We have also demonstrated the ability of legacy fiber infrastructures to carry 200 Gbit/s 16QAM-OFDM over ~1000 km of uncompensated transmission links equipped with EDFA only. This work has also inspired a contribution given recently in the carriers group of Optical InternetWorking Forum (OIF) promoting the advantages of MB-OFDM for 400 Gbit/s WDM transmission [24].

2.1.6 Offset-QAM OFDM

N-FDM, F-OFDM and C-OFDM have been discussed in previous sections. N-FDM employs filters at transmitters/receivers to create a rectangular spectral profile (see Figure 2.24). On the other hand, F/C-OFDM utilizes a sinc-function spectrum to achieve sub-channel orthogonality. However, with either technique, there is a long oscillating tail in the frequency or time domain, resulting in disadvantages such as vulnerability to intercarrier interference (ICI) in F/C-OFDM and a long memory length for pulse shaping in N-FDM.

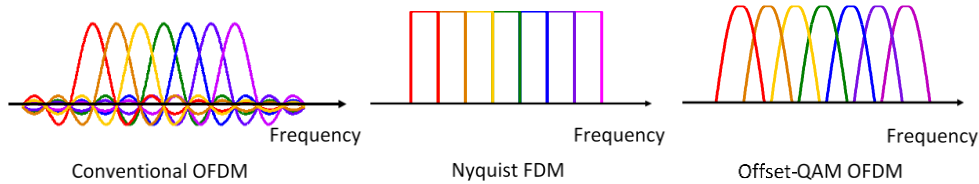


Figure 2.24: Spectra of C-OFDM, N-FDM, and offset-QAM OFDM

In this section, we will investigate a new multicarrier scheme, offset quadrature amplitude modulation (offset-QAM) OFDM [25-28]. In this technology, the required signal spectra for sub-channel orthogonality do not have to be a rectangular or sinc function and can be greatly relaxed. For example, the square-root-raised-cosine (SRRC) function, well known for inter-symbol interference (ISI) free operation in the single-channel case, cannot achieve sub-channel orthogonality in multicarrier systems unless offset-QAM formats are used. In the following, we will investigate discrete Fourier transform (DFT) based implementation of offset-QAM OFDM and discuss the multiplexing/demultiplexing design as well as phase estimation and channel estimation algorithms.

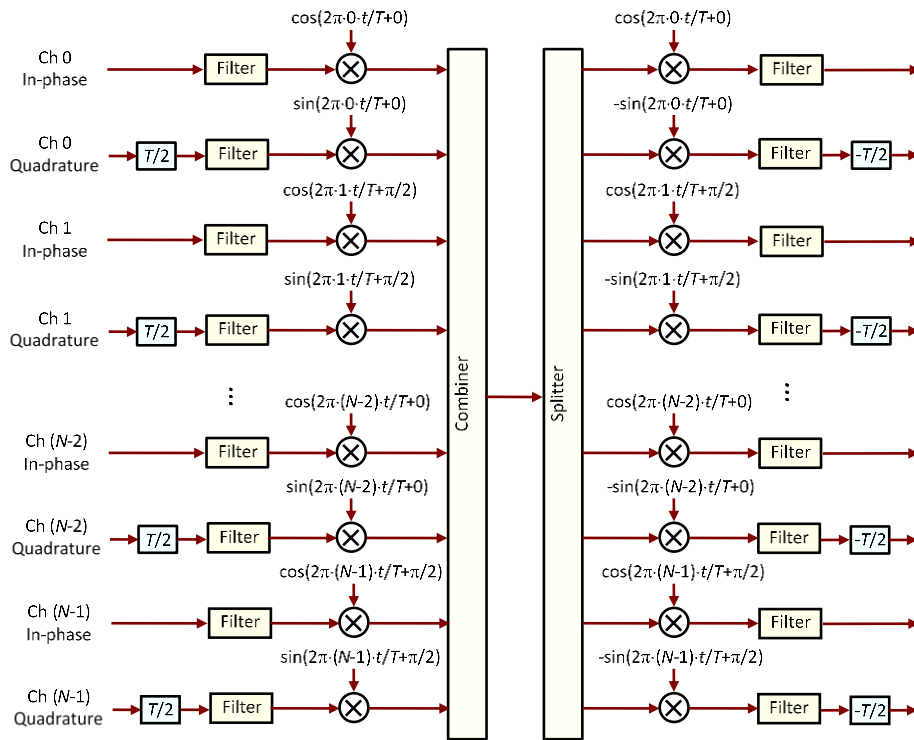


Figure 2.25: Principle of multiplexing and de-multiplexing of offset-QAM OFDM. N is assumed to be an even number.

Figure 2.25 depicts the principle of multiplexing and de-multiplexing of offset-QAM OFDM. In single-carrier offset-QAM, the quadrature signal is delayed by $T/2$ with respect to the in-phase signal, where T is the symbol period. Offset-QAM OFDM multiplexes multiple sub-channels carrying offset-QAM data, with $\pi/2$ phase difference between adjacent sub-channels.

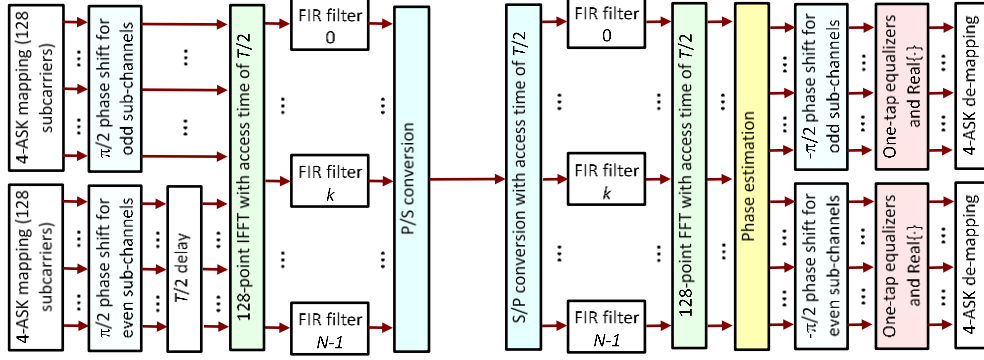


Figure 2.26: DFT-based implementation of offset 16QAM OFDM

Figure 2.26 shows DFT-based implementation for offset-QAM OFDM. Offset-16QAM format is adopted in the illustration. Two bi-polar four-amplitude-shift-keying (4-ASK) data are encoded with Gray coding. For the in-phase tributary, the phases of even subcarriers are set to be 0 (or π) while those of odd subcarriers are set to be $\pi/2$ (or $3\pi/2$). Conversely, for the quadrature tributary, the phases of odd subcarriers are set to be 0 (or π) while those of even subcarriers are set to be $\pi/2$ (or $3\pi/2$). The quadrature tributary is then delayed by half symbol period, $T/2$, with respect to the in-phase tributary. An inverse fast Fourier transform (IFFT) is applied to generate time-domain samples from the in-phase tributary at times $i \times N$, and from the quadrature tributary at times $(i + 1/2) \times N$, where i is an integer and N is the number of samples per OFDM symbol. The generated outputs pass through finite impulse response (FIR) filters for pulse shaping before parallel-to-serial (P/S) conversion. Assuming that $a_{i,n}$ and $s(i \cdot N + k)$ are the n^{th} subcarrier data in the frequency domain and the k^{th} sample in the time domain in the i^{th} OFDM symbol, $s(i \cdot N + k)$ is derived as:

$$\begin{aligned}
 s(i \cdot N + k) &= s^{real}(i \cdot N + k) + j \cdot s^{imag}(i \cdot N + k) \\
 &= \sum_{p=-\infty}^{+\infty} \sum_{n=-N/2+1}^{N/2} a_{p,n}^{real} \exp(j\pi n/2) \cdot \exp(2\pi j(p \cdot N + k) \cdot n/N) \cdot h(i \cdot N + k - p \cdot N) \\
 &\quad + \sum_{p=-\infty}^{+\infty} \sum_{n=-N/2+1}^{N/2} a_{p,n}^{imag} \exp(j\pi(n+1)/2) \cdot \exp(2\pi j(p \cdot N + k) \cdot n/N) \cdot h(i \cdot N + k - N/2 - p \cdot N)
 \end{aligned} \tag{1}$$

$$k = -N/2 + 1, -N/2 + 2, \dots, N/2 - 1, N/2$$

In Eq. (1), we employ the periodic property and set the ranges of n and k to be $[-N/2 + 1, N/2]$, rather than $[0, N - 1]$, to facilitate mathematical derivations. $h(i \cdot N + k)$, $-\infty < i < +\infty$, represents the impulse response of the k^{th} FIR filter, with one sample per OFDM symbol for each k . The required sampling rate of DACs for $s(i \cdot N + k)$ is N/T , the same as that in C-OFDM without additional requirement on the hardware speed.

At the receiver, the received signal is serial-to-parallel (S/P) converted with the access time of $T/2$, that is, the in-phase tributary accesses the sampled points from times $i \cdot N$ while the quadrature tributary accesses the sampled points from times $(i + \frac{1}{2}) \cdot N$. The outputs pass through FIR filters, and an FFT is applied to transform the signals to the frequency domain. Without loss of generality, we only derive the output of the FFT for the in-phase tributary of the m th subcarrier in the i th OFDM symbol, $b_{i,m}^{real}$:

$$b_{i,m}^{real} = \sum_{k=-N/2+1}^{N/2} \sum_{q=-\infty}^{+\infty} \exp(-2\pi j k \cdot m/N) \cdot r((i - q) \cdot N + k) \cdot h_{receiver,k}(q \cdot N) \tag{2}$$

where $r(i \cdot N + k)$ is the received time-domain signal. We firstly assume an ideal channel so that $r(i \cdot N + k) = s(i \cdot N + k)$. $h_{receiver,k}(q \cdot N)$ is the impulse response of the k th receiver FIR filter. For proper decoding, $h_{receiver,k}(q \cdot N)$ is set to be $h(q \cdot N - k)$. Therefore, the remaining problem is to design $h(i \cdot N - k)$ to ensure the subcarrier orthogonality. In C-OFDM and N-FDM, the pulse shape should be a rectangular and a sinc function, respectively. In offset-QAM OFDM, the requirement for the design of

pulse shape or signal spectral profile to achieve subcarrier orthogonality can be greatly relaxed: a) the signal pulse is an even function; b) the signal pulse satisfies the ISI free criterion; c) there is no spectral overlap between subcarriers with more than one subcarrier distance (e.g. the m^{th} and $(m \pm 2)^{th}$ subcarriers). We firstly apply condition c) to Eq. (2) and derive $b_{i,m}^{real}$ in Eq. (2) as:

$$\begin{aligned}
 b_{i,m}^{real} = & \sum_{k_1=-\infty}^{+\infty} \sum_{p=-\infty}^{+\infty} a_{p,m}^{real} \exp(j\pi m/2) \cdot h((i-p) \cdot N - k_1) \cdot h(k_1) \\
 & + \sum_{k_1=-\infty}^{+\infty} \sum_{p=-\infty}^{+\infty} a_{p,m+1}^{real} \exp(j\pi(m+1)/2) \cdot h((i-p) \cdot N - k_1) \cdot h(k_1) \cdot \exp(2\pi j k_1 / N) \\
 & + \sum_{k_1=-\infty}^{+\infty} \sum_{p=-\infty}^{+\infty} a_{p,m-1}^{real} \exp(j\pi(m-1)/2) \cdot h((i-p) \cdot N - k_1) \cdot h(k_1) \cdot \exp(-2\pi j k_1 / N) \\
 & + \sum_{k_1=-\infty}^{+\infty} \sum_{p=-\infty}^{+\infty} a_{p,m}^{imag} \exp(j\pi(m+1)/2) \cdot h((i-p) \cdot N - N/2 - k_1) \cdot h(k_1) \\
 & + \sum_{k_1=-\infty}^{+\infty} \sum_{p=-\infty}^{+\infty} a_{p,m+1}^{imag} \exp(j\pi(m+2)/2) \cdot h((i-p) \cdot N - N/2 - k_1) \cdot h(k_1) \cdot \exp(2\pi j k_1 / N) \\
 & + \sum_{k_1=-\infty}^{+\infty} \sum_{p=-\infty}^{+\infty} a_{p,m-1}^{imag} \exp(j\pi(m)/2) \cdot h((i-p) \cdot N - N/2 - k_1) \cdot h(k_1) \cdot \exp(-2\pi j k_1 / N)
 \end{aligned} \quad (3)$$

where $k_1 = q \cdot N - k$. The six terms on the right-hand side of Eq. (3) represent the influence of the in-phase tributary of the m^{th} , $(m+1)^{th}$, and $(m-1)^{th}$ subcarriers, and the quadrature tributary of the m^{th} , $(m+1)^{th}$, and $(m-1)^{th}$ subcarriers, respectively. Condition b) is then applied to further simplify Eq. (3). Because the pulse shape satisfies ISI free criteria, the first term on the right-hand side of Eq. (3) can be re-written as:

$$\sum_{k_1=-\infty}^{+\infty} \sum_{p=-\infty}^{+\infty} a_{p,m}^{real} \cdot \exp(j\pi m/2) \cdot h((i-p) \cdot N - k_1) \cdot h(k_1) = a_{i,m}^{real} \cdot \exp(j\pi m/2) \quad (4)$$

On the other hand, the second term on the right-hand side of Eq. (3) can be obtained as:

$$\begin{aligned}
 & \sum_{k_1=-\infty}^{+\infty} \sum_{p=-\infty}^{+\infty} a_{p,m+1}^{real} \exp(j\pi(m+1)/2) \cdot h((i-p) \cdot N - k_1) \cdot h(k_1) \cdot \exp(2\pi j k_1 / N) \\
 & = j \cdot \exp(j\pi m/2) \cdot (-1)^{i-p} \cdot \sum_{k_2=-\infty}^{+\infty} \sum_{p=-\infty}^{+\infty} a_{p,m+1}^{real} \cdot h((i-p) \cdot N/2 - k_2) \cdot h((i-p) \cdot N/2 + k_2) \cdot \exp(2\pi j k_2 / N) \\
 & = j \cdot c_{m+1}^{real} \cdot \exp(j\pi m/2)
 \end{aligned} \quad (5)$$

where c_{m+1}^{real} is real. In Eq. (5), we use condition a): if $h(\cdot)$ is an even function, it is readily derived that $h\left((i-p) \cdot \frac{N}{2} - k_2\right) \cdot h((i-p) \cdot N/2 + k_2)$ is also an even function. From Eqs. (4)-(5), we find that the decoded signal is real while the crosstalk value from the in-phase tributary of the $(m+1)^{th}$ subcarrier is imaginary. It is noted that the crosstalk can be from ... $(i-2)^{th}, (i-1)^{th}, i^{th}, (i+1)^{th}, (i+2)^{th}$... symbols of adjacent subcarriers $(m+1)$. Similar manipulation can be carried out to derive other terms on the right-hand side of Eq. (3), so that Eq. (3) can be written as:

$$b_{i,m}^{real} = (a_{i,m}^{real} + j \cdot c_{m+1}^{real} + j \cdot c_{m-1}^{real} + j \cdot c_m^{imag} + j \cdot c_{m+1}^{imag} + j \cdot c_{m-1}^{imag}) \cdot \exp(j\pi m/2) \quad (6)$$

where c_{m+1}^{real} , c_{m-1}^{real} , c_m^{imag} , c_{m+1}^{imag} , c_{m-1}^{imag} represent the crosstalk from the in-phase tributary of the $(m+1)^{th}$ and $(m-1)^{th}$ subcarriers, and the quadrature tributary of the m^{th} , $(m+1)^{th}$, and $(m-1)^{th}$ subcarriers, respectively.

From Eq. (6), it can be seen that in an ideal case, the desirable signal is real while crosstalk value is imaginary. Therefore, data can be correctly decoded if the phase shifts applied to different subcarriers at the transmitters, $\exp(j\pi m/2)$, are reversed and the real part is extracted:

$$a_{i,m,est}^{real} = \text{real}\{b_{i,m}^{real} \cdot \exp(-j\pi m/2)\} = a_{i,m}^{real} \quad (7)$$

However, Eq. (6) does not consider the channel response. In practice, the responses of electrical drivers, modulators, optical filters, and photodiodes, as well as dispersion and timing errors in the synchronization process, would influence the performance. When the number of subcarriers is large such that the system response on the signal spectrum of individual subcarriers is approximately a constant, we can generalize Eq. (6) as:

$$b_{i,m}^{real} = \exp(j\pi n/2) \cdot \exp(j\varphi_i) \cdot (a_{i,m}^{real} \cdot H(\omega_m) + j \cdot c_{m+1}^{real} \cdot H(\omega_{m+1}) + j \cdot c_{m-1}^{real} \cdot H(\omega_{m-1}) + j \cdot c_m^{imag} \cdot H(\omega_m) + j \cdot c_{m+1}^{imag} \cdot H(\omega_{m+1}) + j \cdot c_{m-1}^{imag} \cdot H(\omega_{m-1})) \quad (8)$$

where $H(\omega_m) = H_{btb}(\omega_m) \cdot \exp\left(\frac{j\beta_2\omega_m^2 L}{2}\right) \cdot \exp(-j\tau\omega_m)$. φ_i is the common phase error (CPE) in the i th symbol. $H(\omega_m)$ represents the overall system response at the frequency of the m th subcarrier ω_m , and includes the contributions from the back-to-back response, $H_{btb}(\omega_m)$, the dispersion, and the time delay. L and β_2 are the fiber length and the second-order dispersion value, respectively. τ represents the value of time delay. In practice, $H(\omega_m) \approx H(\omega_{m+1}) \approx H(\omega_{m-1})$ under commonly used number of subcarriers in OFDM systems, e.g. 128/256/512 subcarriers. Equation (8) assumes that the GI is sufficient so that there is no ISI between OFDM symbols. In contrast to C-OFDM, the GI to avoid ISI and ICI in the presence of dispersion is greatly reduced in offset-QAM OFDM. Dispersion in fiber links introduces two effects: 1) the pulse of each sub-channel is broadened; 2) the pulses of different sub-channels transmit at different speed, which results in time delays between sub-channels. The first effect is negligible especially for a large number of sub-channels, as it scales with the bandwidth of each sub-channel. The second effect scales with the bandwidth of the full OFDM spectrum and dominates the performance. In C-OFDM, when there is no GI, the demultiplexing filter for the target sub-channel is no longer orthogonal to other sub-channels. Due to the long spectral tails of the sinc function, all sub-channels would introduce ICI (or ISI) to the target sub-channel (or the target OFDM symbol). In order to avoid the ICI and ISI, the length of the GI should be larger than the time delay between the sub-channels that have the largest distance in frequency. In contrast, in offset-QAM OFDM, the spectral tail can be greatly suppressed. The ICI and ISI due to the absence of GI are only from adjacent sub-channels after the demultiplexing filter. The required GI length, T_{GI} , is obtained as:

$$T_{GI} = |L \cdot \beta_2 \cdot \Delta\omega| \quad (9)$$

$\Delta\omega$ is equal to the full OFDM bandwidth in C-OFDM and twice the subcarrier spacing in offset-QAM OFDM, respectively. In a system with 10-GHz signal bandwidth and 128 subcarriers, it can be readily calculated that the required GI lengths after 600-km SMF transmission ($\beta_2 = -21.7 \text{ ps}^2/\text{km}$) are 818 ps and 12.8 ps for C-OFDM and offset-QAM OFDM, respectively. These values, in the discrete domain, correspond to 8 and 0 samples, respectively. It is also expected from Eq. (9) that the larger the number of subcarriers, the shorter the required GI length. Therefore, the proposed scheme may reduce the length of GI for dispersion compensation, in particular for a large number of subcarriers.

In terms of phase estimation, pilot tones can be employed. In principle, pilot tones should be inserted as the DC to eliminate the influence of the dispersion. In the case that the driving amplifiers are AC-coupled, a pilot tone is inserted into a subcarrier close to the DC such that $\exp\left(\frac{j\beta_2 L \omega_m^2}{2}\right) \approx 1$. In addition, due to the suppressed spectral tail, only the $(m-1)^{\text{th}}$ and $(m+1)^{\text{th}}$ sub-channels would introduce ICI and ISI to the target m^{th} sub-channel. Therefore, adjacent sub-channels of the pilot tone are un-modulated to avoid the crosstalk term. The pilot tone for the i^{th} symbol is then written as:

$$P_{i,m} \propto \exp(j\pi n/2) \cdot \exp(j\varphi_i) \quad (10)$$

where m is set such that ω_m is in the zero-frequency region. The pilot tones can be extracted, conjugated, and used for phase correction.

The final issue in the design is the channel estimation. In C-OFDM, because there is no crosstalk between subcarriers, channel response can be estimated using the least squares (LS) method based on time-

domain averaging, pilot tones, or intra-symbol frequency-domain averaging. In offset-QAM OFDM, despite the orthogonality to the desirable signal, the crosstalk terms in Eq. (8) would influence the channel estimation performance when the conventional LS method is applied. From Eq. (8), it is deduced that if the phase of the channel response at ω_m is not correctly recovered, the nonlinear operation of $real\{\cdot\}$ would filter out part of signal power and pass through part of crosstalk power, resulting in performance degradation. Therefore, the phase terms in $b_{i,m}^{real}$ have to be firstly compensated, and then the amplitude of the channel response is estimated by:

$$H_{est}(\omega_m) = \frac{1}{M} \sum_{p=1}^M real\{b_{p,m}^{real} \cdot \exp(-j\pi m/2) \cdot \exp(-j\beta_2 L \omega_m^2/2) \cdot \exp(j\tau \omega_m) \cdot \exp(-j\varphi_p)\} / a_{p,m}^{real} \quad (11)$$

where M is the number of averaging symbols and should be sufficiently large to mitigate the noise impact. The CPE φ_i can be estimated before channel estimation using pilot tones. However, Eq. (11) requires accurate estimation of the dispersion $\beta_2 L$ and places stringent requirement on the symbol synchronization algorithm in the offset-QAM OFDM system. More importantly, it is found in the experiment that even when the parameters $\beta_2 L$ and τ are precisely determined (e.g. via manual optimization), there is still a penalty. This penalty may be from imperfect channel estimation using Eq. (11), which does not consider the residual phase shifts in the responses of optoelectronic devices, i.e. $H_{btb}(\omega_m)$. These residual phases are unknown in practice and have different values for different ω_m .

To solve this problem, we firstly propose to improve the channel estimation performance by appropriately designing the training symbols (TSs). From Eq. (8), it can be deduced that the crosstalk terms on the m th subcarrier are only from the $(m-1)$ th and the $(m+1)$ th subcarriers. Therefore, if the training data are inserted every two subcarriers in the TSs, the crosstalk terms may be avoided. However, further design consideration is required. To clearly see this, we study two kinds of TSs, named modified LS-1 (M-LS-1) and M-LS-2, respectively: 1) Odd subcarriers are set to be real-valued while even subcarriers are set to be zero in the 1st, 3rd, 5th... TSs. Conversely, in the 2nd, 4th, 6th... TSs, even subcarriers are set to be real-valued while odd subcarriers are set to be zero. 2) Odd subcarriers are set to be real-valued while even subcarriers are set to be zero in the 1st, 2nd, ..., $(M/2)^{th}$ TSs. Conversely, even subcarriers are set to be real-valued while odd subcarriers are set to be zero in the $(M/2+1)^{th}$, $(M/2+2)^{th}$, ..., M^{th} TSs, where M is the number of TSs. Channel estimation is realized by using:

$$H_{est}(\omega_{2m-1}) = \frac{2}{M} \sum_{p \in P_{2m-1}} b_{p,2m-1}^{real} \cdot \exp(-j\pi(2m-1)/2) \cdot \exp(-j\varphi_p) / a_{p,2m-1}^{real} \quad (12.1)$$

$$H_{est}(\omega_{2m}) = \frac{2}{M} \sum_{p \in P_{2m}} b_{p,2m}^{real} \cdot \exp(-j\pi(2m)/2) \cdot \exp(-j\varphi_p) / a_{p,2m}^{real} \quad (12.2)$$

where the channel response for odd and even subcarriers are estimated individually using corresponding TSs, P_{2m-1} and P_{2m} . M-LS-1 and M-LS-2 can have significantly different performance although only the position of TSs for estimating the response of odd and even subcarriers varies. It is attributed to the fact that the signal pulses between OFDM symbols overlap, and by using M-LS-1, channel estimation performance is still degraded by the crosstalk from adjacent subcarriers in adjacent offset-QAM OFDM symbols. In contrast, M-LS-2 may mitigate the crosstalk and approach the optimal performance.

In addition to the design of TSs, we also propose a method to track the unknown phase shift at each frequency, ω_m , before the nonlinear operator $real\{\cdot\}$. Assuming the estimated channel response is $H_{est}(\omega_m)$, we have:

$$a_{i,m,est}^{real} = real\{b_{i,m}^{real} \cdot \exp(-j\pi m/2) \cdot H_{est,i}(\omega_m)\} \quad (13.1)$$

$$H_{est,i}(\omega_m) = H_{est,i-1}(\omega_m) + e \cdot \delta_i(\omega_m) \quad (13.2)$$

$$\delta_i(\omega_m) = 0.5 \times \delta_{i-1}(\omega_m) + 0.5 \times (a_{i-1,m}^{real} - a_{i-1,m,est}^{real}) \cdot \left(\frac{\partial a_{i,m,est}^{real}}{\partial real\{H_{est,i}(\omega_m)\}} + j \frac{\partial a_{i,m,est}^{real}}{\partial imag\{H_{est,i}(\omega_m)\}} \right) \quad (13.3)$$

where e is a parameter to control the estimation speed. The channels in practical optical communication systems are commonly static, and so the estimation process is only required at the initial stage. However, this method is also applicable to a slow-varying optic-fiber channel to track the channel. We will show that when applied in offset-QAM OFDM systems, this method can greatly relax the requirements for symbol synchronization and prior estimation of dispersion parameters compared to the conventional LS method. In addition, it precisely estimates unknown residual phases in the responses of optoelectronic devices $H_{btb}(\omega_m)$ and overcomes the performance limit of Eq. (11). Because Eq. (13) uses modified least-mean-square (LMS) algorithm after the nonlinear operation $real\{\cdot\}$ to track the correct phase shifts at each ω_m , we call this method M-LMS-1.

Equation (13) may mitigate the impact of crosstalk in Eq. (8) even when these crosstalk terms exit without special design of the TSs. In all proposed methods above (M-LS-1, M-LS-2, and M-LMS-1), the receiver FIR filter is designed to be $h_{receiver,k}(q \cdot N) = h(q \cdot N - k)$ and channel estimation does not produce update to the coefficients of the pulse-shaping FIR filters. However, it is unknown if the presence of channel response in the hardware as well as dispersion, delay, etc. may possibly break this orthogonality. In order to clarify this issue, we further study a more completed algorithm (named M-LMS-2) which includes the response of the FIR filters in the channel estimation:

$$\vec{h}_{receiver,k,i} = \vec{h}_{receiver,k,i-1} + \varepsilon \cdot \vec{\kappa}_{k,i} \quad (14.1)$$

$$\vec{\kappa}_{k,i} = 0.5 \times \vec{\kappa}_{k,i-1} + 0.5 \times (a_{i-1,m}^{real} - a_{i-1,m,est}^{real}) \cdot conj(H_{est,i-1}(\omega_m) \cdot \vec{r}_{k,i-1} \cdot F_{m,k}) \quad (14.2)$$

where $\vec{h}_{receiver,k,i} = [h_{receiver,k}(-l \cdot \frac{N}{2}) \cdot \dots \cdot h_{receiver,k}(l \cdot \frac{N}{2})]$ with l being the memory length of the FIR filter. $r_{k,i} = [r((i - \frac{l}{2}) \cdot N + k) \cdot \dots \cdot r((i + \frac{l}{2}) \cdot N + k)]$, representing the received time-domain signal vector. $F_{m,k}$ is the element in the m th row and the k th column of the Fourier matrix. $conj(\cdot)$ presents the conjugate. Equation (14) ensures that the FIR filters at the receiver are also optimized in the presence of channel response, and so avoids possible performance degradation due to the loss of the orthogonality. Note that for N subcarriers and M TSs, the complexities of M-LS-1, M-LS-2, and M-LMS-1 scale with $N \cdot M$, while that of M-LMS-2, when N subcarriers and M TSs are fully used, scales with $(l + 1) \cdot N^2 \cdot M$, resulting in higher implementation complexity.

Experiments were carried out to investigate the performance of different channel estimation methods. Figure 2.27 shows the experimental setup. The IFFT and FFT used 128 points, of which 102 subcarriers were used for 16QAM data modulation. The six subcarriers in the zero-frequency region were not modulated, allowing for AC-coupled amplifiers and insertion of pilot tones for phase estimation. The positions of pilot tones were close to DC in order to reduce the influence of dispersion. The twenty subcarriers in the high-frequency region were zero-padded to avoid aliasing. The FIR filter created a set of SRRC functions with different roll-off values, or a 3rd-order super-Gaussian function. In all cases, the 3-dB bandwidth of the shaped spectrum was the same as the subcarrier spacing. The offset-QAM OFDM symbol sequence began with a start-of-frame (SOF) symbol designed to enable symbol synchronization. In M-LS-1 and M-LS-2, the TSs for channel estimation were designed as discussed above. In conventional LS, M-LMS-1, and M-LMS-2 methods, special design was not required. The number of TSs was fixed to be 80 in all methods to ensure that optimal performance could be obtained for fair comparison. Inset of Figure 2.27 shows the spectrum of an offset-QAM OFDM signal when the SRRC function with a roll-off coefficient of 0.5 was used. It can be seen that offset-QAM OFDM avoided the long spectral tails, and so exhibited greatly suppressed side lobes. The generated signal was clipped with a peak-to-average power ratio of 11 dB before being downloaded to an arbitrary waveform generator with 12-GS/s DACs. The signal line rate including FEC was 38 Gb/s.

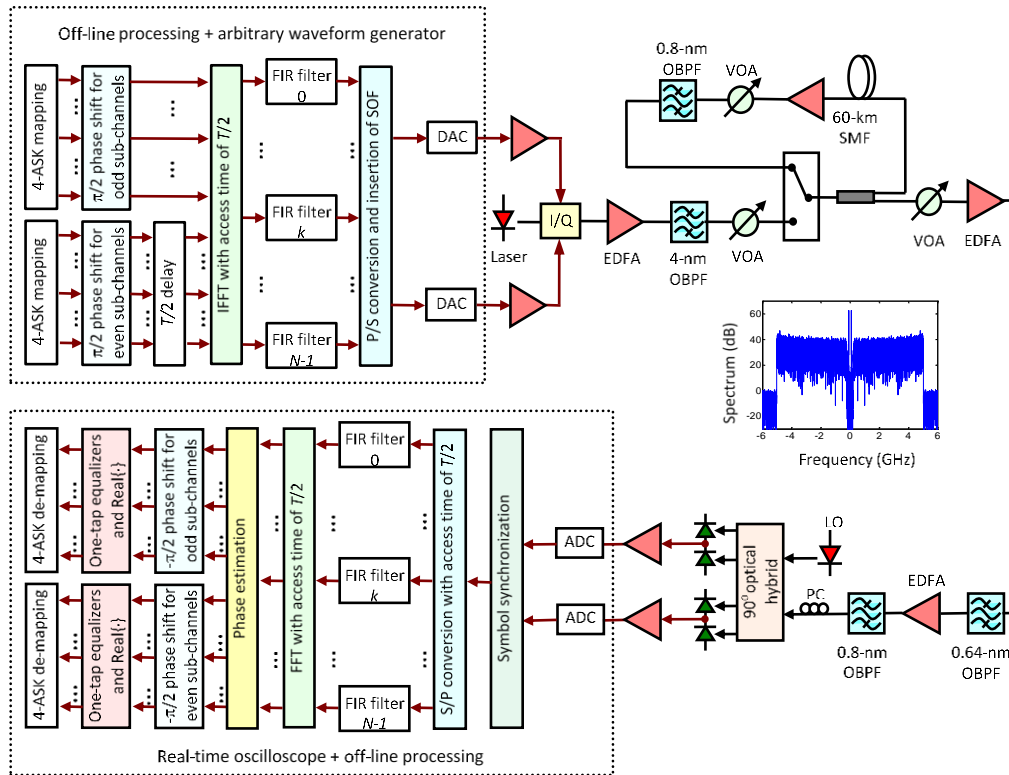


Figure 2.27: Experimental setup of coherent optical offset-16QAM OFDM. Inset shows its spectrum.

A laser was used to generate the optical carrier. The electrical OFDM signal was fed into an optical I/Q modulator with a peak-to-peak driving swing of $0.5V_{\pi}$ to avoid nonlinear distortion. The generated optical signal was amplified by an erbium doped fiber amplifier (EDFA), filtered by a 4-nm optical band-pass filter (OBPF), and transmitted over a recirculating loop comprising 60-km single-mode fiber (SMF) with 14-dB fiber loss. The noise figure of the EDFA was 6 dB and another 0.8-nm OBPF was used in the loop to suppress the amplified spontaneous emission noise. The launch power per span was around -9 dBm to avoid the nonlinear effects. At the receiver, the optical signal was detected with a pre-amplified coherent receiver. A variable optical attenuator (VOA) was used to vary the optical signal-to-noise ratio (OSNR) for the bit error rate (BER) measurements. The pre-amplifier was followed by an OBPF with a 3-dB bandwidth of 0.64 nm, a second EDFA, and another OBPF with a 3-dB bandwidth of 1 nm. The second EDFA at the receiver ensured fixed input powers into photodiodes, and eliminated potential influence of thermal noise. A polarization controller (PC) was used to align the polarization of the filtered OFDM signal before entering the signal path of a 90° optical hybrid. The optical outputs of the hybrid were connected to two balanced photodiodes with 40-GHz 3-dB bandwidths, amplified by 40-GHz electrical amplifiers, and captured using a 50-GS/s real-time oscilloscope. The total number of measured 16QAM symbols was 240,000. The received signal was up-sampled, synchronized, and then serial-to-parallel (S/P) converted before being passed through the receiver FIR filters. An FFT was applied to transform the signals to the frequency domain. Pilot tones were extracted for phase estimation. Different channel estimation methods were employed and the signals were then equalized using one-tap equalizers based on the estimated channel response.

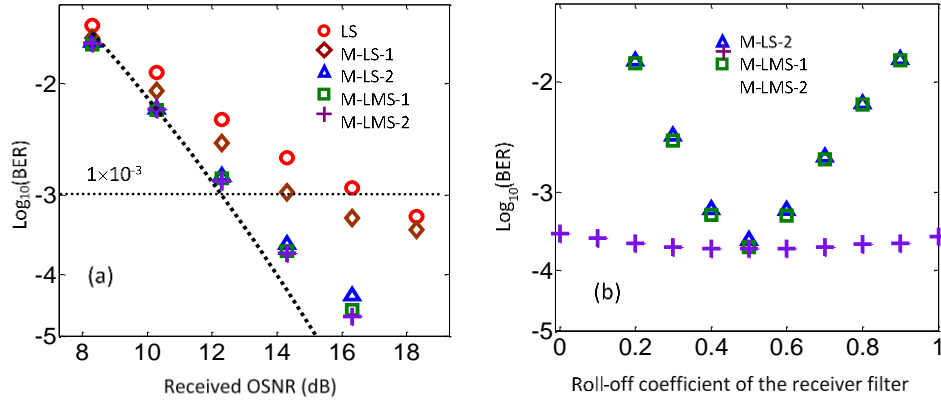


Figure 2.28: (a) BER versus the received OSNR using different channel estimation methods when a SRRC function with the roll-off coefficient of 0.5 is used as the signal spectrum. (b) BER versus roll-off coefficient of the receiver filter for different channel estimation method when the roll-off coefficient of the transmitter filter is 0.5.

Figure 2.28 (a) shows the BER versus the received OSNR for offset-16QAM OFDM with different channel estimation methods when the signal spectral profile is a SRRC function with the roll-off coefficient of 0.5. The figure shows that the conventional LS method exhibits significant performance degradation even when the phase noise, synchronization, and dispersion (0 km in this case) in Eq. (11) are compensated or manually optimized. This penalty might be attributed to the unknown phase shifts in the hardware, including optical filters, amplifiers, etc. The use of the M-LS-1 method improves the performance somewhat. However, although the even subcarriers in the 1st, 3rd, 5th... TSs are set to be zero, the estimated responses at odd subcarriers using the 1st, 3rd, 5th... TSs are still degraded by crosstalk from even subcarriers in the 2nd, 4th, 6th... TSs, due to overlapped signal pulses. M-LS-2 can mitigate this effect, and so shows significantly improved performance. The required OSNR to achieve a BER of 10⁻³ is 12.8 dB, which is close to the theoretical limit of 12.3 dB for a 38-Gbit/s 16QAM signal (dotted line). On the other hand, M-LMS-1 and M-LMS-2 exhibit slightly better performance than the M-LS-2 method. This slight improvement might be due to their adaptive capability to track the optimal operation condition. It is also shown that M-LMS-2 does not result in significant performance improvement compared to M-LS-2 and M-LMS-1 while introducing additional implementation complexity. It implies that in the experiment, once the transmitter and receiver FIR filters are decided and implemented in the digital signal processing, the orthogonality can be maintained regardless of the response of the hardware and the channel. Consequently, M-LS-2 and M-LMS-1 are sufficient to approach the optimal performance at lower implementation complexity. Figure 2.27 (b) shows BER versus the roll-off coefficient of the receiver filter when that of the transmitter filter is 0.5. In order to ensure the orthogonality, the FIR filters at the transmitter and the receiver should satisfy $h_{receiver,k}(q \cdot N) = h(q \cdot N - k)$. M-LS-2 and M-LMS-1 do not have the capability to recover the orthogonality if this assumption is broken. On the other hand, M-LMS-2 is more tolerant to the loss of channel orthogonality. It is noted that in a relatively static metro or long-distance optical communication system, the FIR filters can be known beforehand, and so the benefit of M-LMS-2 over M-LS-2 and M-LMS-1 is limited while additional complexity is induced. However, M-MLS-2 may have advantages in secure optical networks.

Next, we simulate 112-Gb/s PDM offset-4QAM OFDM and 224-Gb/s PDM offset-16QAM OFDM systems, and compare these systems with C-OFDM to find out the advantage of the proposed scheme. The simulation setup was similar to Figure 2.16. The sampling rate of the DACs was 40 GS/s. The subcarrier number varied from 32 to 1024. For each case, the number of zero-padded subcarriers in the high-frequency region was controlled such that the signal line rate (including the GI in C-OFDM) was fixed to be 112 Gb/s and 224 Gb/s for offset-4QAM (4QAM in C-OFDM) and offset-16QAM (16QAM in C-OFDM), respectively. Nonlinearity was not considered in order to isolate the effect of dispersion. In offset-QAM OFDM, the FIR filter created a set of SRRC functions with a roll-off coefficient of 0.5. The sampling rate of

the oscilloscope at the receiver was 40 GS/s. The total simulated 4QAM (or 16QAM) symbols were around 200,000.

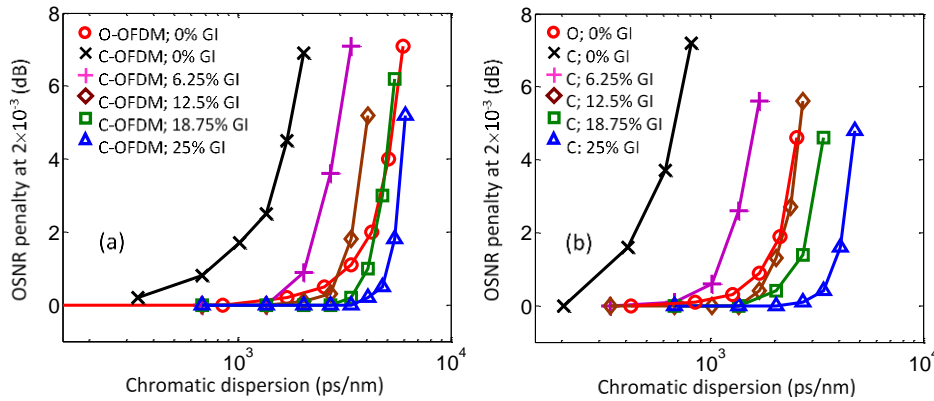


Figure 2.28: OSNR penalty versus CD for (a) PDM offset-4QAM OFDM without GI and conventional PDM 4QAM OFDM with different GI lengths; (b) PDM offset-16QAM OFDM without GI and conventional PDM 16QAM OFDM with different GI lengths. The subcarrier number is 128. O-OFDM stands for offset-QAM OFDM.

Figure 2.28 shows the OSNR penalty versus CD for (a) PDM (offset-) 4QAM OFDM and (b) PDM (offset-) 16QAM OFDM when the subcarrier number is 128. It can be seen that when GI was not used in C-OFDM, the performance was degraded rapidly as CD increased. The transmission reach was extended by using a longer GI, which however reduced the net data rate. 16QAM OFDM was more sensitive to ISI so exhibited poorer CD tolerance than 4QAM OFDM. On the other hand, offset-QAM OFDM without GI significantly outperformed C-OFDM with 0% GI. Offset-4QAM and offset-16QAM OFDM could realize transmission reaches similar to those obtained with the C-OFDM with 18.75% and 12.5% GI length, respectively.

The CD tolerance of offset-QAM OFDM scales with twice the subcarrier spacing, so inversely with the subcarrier number at a fixed OFDM bandwidth. Figure 2.29(a) shows the OSNR penalty versus CD for 112-Gb/s PDM offset-4QAM OFDM with different subcarrier numbers. As expected, the larger the subcarrier number, the better the CD tolerance. For 1024 subcarriers, 112-Gb/s PDM offset-4QAM OFDM could support $\sim 36,000$ ps/nm without any GI at the 3-dB penalty, which corresponded to the dispersion value of $\sim 2,100$ -km fiber. Figure 2.29(b) illustrates supported CD values at the 3-dB penalty versus the subcarrier number. It can be seen that the transmission reaches scaled linearly with the subcarrier number for both offset-QAM OFDM and C-OFDM. For subcarrier numbers larger than 64, $\sim 18.75\%$ GI was required in C-OFDM to achieve the same performance as offset-QAM OFDM without any GI. This verifies that the presented scheme is more suitable for long-distance transmissions, with $1/(1-0.1875)=23\%$ increase in net data rate.

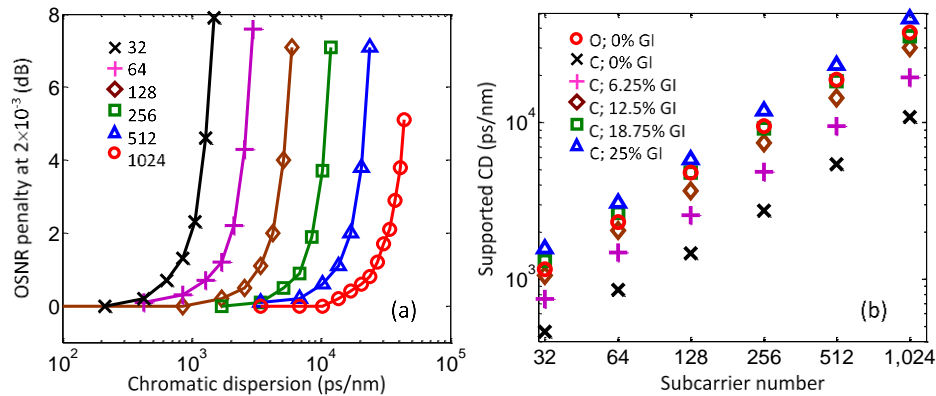


Figure 2.29: (a) OSNR penalty versus CD for PDM offset-4QAM OFDM without GI and with different subcarrier numbers; (b) Supported CD values at the 3-dB OSNR penalty versus the subcarrier number for offset-4QAM OFDM and conventional 4QAM OFDM.

2.1.6.1 Discussion

Offset quadrature amplitude modulation OFDM exhibits enhanced net data rates compared to C-OFDM, and reduced complexity compared to N-FDM. In this report, we experimentally demonstrated the implementation of 38-Gbit/s offset-16QAM OFDM. Further numerical simulations showed that by avoiding the GI, 112-Gbit/s polarization multiplexed offset-4QAM OFDM could achieve 23% increase in net data rate over C-OFDM under the same transmission reach.

Most algorithm designs in offset-QAM OFDM are similar to C-OFDM. However, channel estimation in offset-QAM OFDM requires particular study. Although the residual crosstalk is orthogonal to the decoded signal, its existence degrades the channel estimation performance when the conventional least-square method is applied. We investigate four channel estimation algorithms for offset-QAM OFDM that vary in terms of performance, complexity, and tolerance to system parameters. It is theoretically and experimentally shown that simple channel estimation can be realized in offset-QAM OFDM with the achieved performance close to the theoretical limit. This, together with the advantages over C-OFDM and N-FDM, makes this technology very promising for optical communication systems.

2.1.7 References

- [1] P. C. Schindler, R. Schmogrow, S. Wolf, B. Baeuerle, B. Nebendahl, C. Koos, *et al.*, "Full flex-grid asynchronous multiplexing demonstrated with Nyquist pulse-shaping," *Optics Express*, vol. 22, pp. 10923-10937, 2014/05/05 2014.
- [2] R. Essiambre, G. Kramer, P. J. Winzer, G. J. Foschini, and B. Goebel, "Capacity Limits of Optical Fiber Networks," *Lightwave Technology, Journal of*, vol. 28, pp. 662-701, 2010.
- [3] R. Schmogrow, B. Nebendahl, M. Winter, A. Josten, D. Hillerkuss, S. Koenig, *et al.*, "Error Vector Magnitude as a Performance Measure for Advanced Modulation Formats," *Photonics Technology Letters, IEEE*, vol. 24, pp. 61-63, 2012.
- [4] B. Baeuerle, A. Josten, F. C. Abrecht, E. Dornbierer, J. Boesser, M. Dreschmann, *et al.*, "Multiplier-Free, Carrier-Phase Recovery for Real-Time Receivers Using Processing in Polar Coordinates," in *Optical Fiber Communication Conference*, Los Angeles, California, 2015, p. W1E.2.
- [5] J. E. Volder, "The CORDIC Trigonometric Computing Technique," *Electronic Computers, IRE Transactions on*, vol. EC-8, pp. 330-334, 1959.
- [6] T. Pfau, S. Hoffmann, and R. Noe, "Hardware-Efficient Coherent Digital Receiver Concept With Feedforward Carrier Recovery for M-QAM Constellations," *Lightwave Technology, Journal of*, vol. 27, pp. 989-999, 2009.

- [7] J. Zhao, "Multi-Tap Equalization for Performance Improvement in Optical Fast OFDM Systems," *Photonics Technology Letters, IEEE*, vol. 27, pp. 42-45, 2015.
- [8] Z. Jian and A. Ellis, "Transmission of 4-ASK Optical Fast OFDM With Chromatic Dispersion Compensation," *Photonics Technology Letters, IEEE*, vol. 24, pp. 34-36, 2012.
- [9] Z. Jian, S. K. Ibrahim, D. Rafique, P. Gunning, and A. D. Ellis, "Symbol Synchronization Exploiting the Symmetric Property in Optical Fast OFDM," *Photonics Technology Letters, IEEE*, vol. 23, pp. 594-596, 2011.
- [10] J. Zhao and A. Ellis, "Advantage of Optical Fast OFDM Over OFDM in Residual Frequency Offset Compensation," *Photonics Technology Letters, IEEE*, vol. 24, pp. 2284-2287, 2012.
- [11] "Alcatel-Lucent 1830 PSS brochure, www.alcatel-lucent.com; Ciena 6500 Packet Optical Platform brochure, www.ciena.com; Huawei OSN 9800 brochure, www.huawei.com," ed.
- [12] O. Bertran-Pardo, J. Renaudier, H. Mardoyan, P. Tran, F. Vacondio, M. Salsi, *et al.*, "Experimental assessment of transmission reach for uncompensated 32-GBaud PDM-QPSK and PDM-16QAM," in *Optical Fiber Communication Conference*, Los Angeles, California, 2012, p. JW2A.53.
- [13] "LEIA 65 GSamples/s DAC brochure, www.emea.fujitsu.com," ed.
- [14] Y. R. Zhou, K. Smith, R. Payne, A. Lord, G. Whalley, T. Bennett, *et al.*, "Real-Time Gridless 800G Super-channel Transport Field Trial over 410km Using Coherent DP-16 QAM," in *Optical Fiber Communication Conference*, San Francisco, California, 2014, p. Tu2B.3.
- [15] A. Pagano, E. Riccardi, M. Bertolini, V. Farelli, and T. Van De Velde, "400Gb/s Real-time Trial Using Rate-adaptive Transponders for Next Generation Flexible-grid Networks," in *Optical Fiber Communication Conference*, San Francisco, California, 2014, p. Tu2B.4.
- [16] "France Telecom-Orange and Alcatel-Lucent deploy world's first live 400 Gbit/s per wavelength optical link," www.orange.com," ed.
- [17] S. L. Jansen, I. Morita, T. C. W. Schenk, and H. Tanaka, "121.9-Gb/s PDM-OFDM Transmission With 2-b/s/Hz Spectral Efficiency Over 1000 km of SSMF," *Lightwave Technology, Journal of*, vol. 27, pp. 177-188, 2009.
- [18] "Corning SMF-28e+® Optical Fiber brochure, www.corning.com," ed.
- [19] "Corning LEAF® Optical Fiber brochure, www.corning.com," ed.
- [20] E. Pincemin, M. Song, J. Karaki, O. Zia-Chahabi, T. Guillosoy, D. Grot, *et al.*, "Multi-Band OFDM Transmission at 100 Gbit/s With Sub-Band Optical Switching," *Lightwave Technology, Journal of*, vol. 32, pp. 2202-2219, 2014.
- [21] T. J. Xia, G. A. Wellbrock, M.-F. Huang, S. Zhang, Y.-K. Huang, D.-I. Chang, *et al.*, "Transmission of 400G PM-16QAM Channels over Long-Haul Distance with Commercial All-Distributed Raman Amplification System and Aged Standard SMF in Field," in *Optical Fiber Communication Conference*, San Francisco, California, 2014, p. Tu2B.1.
- [22] J. D. Downie, J. Hurley, and D. Pikula, "Transmission of 256 Gb/s PM-16QAM and 128 Gb/s PM-QPSK signals over long-haul and submarine systems with span lengths greater than 100 km," in *Optical Communication (ECOC 2013), 39th European Conference and Exhibition on*, 2013, pp. 1-3.
- [23] "Making Sense of Effective Bits in Oscilloscope Measurements", application note, www.tektronix.com," ed.
- [24] ""Long-haul and metro coherent 400G DWDM", OIF Carrier WG, July 2014," ed.
- [25] J. Zhao, "Channel estimation in DFT-based offset-QAM OFDM systems," *Optics Express*, vol. 22, pp. 25651-25662, 2014/10/20 2014.

- [26] J. Zhao, "DFT-based offset-QAM OFDM for optical communications," *Optics Express*, vol. 22, pp. 1114-1126, 2014/01/13 2014.
- [27] J. Zhao and A. D. Ellis, "Enhanced Dispersion Tolerance of Coherent Offset-QAM OFDM over Conventional OFDM," in *Optical Fiber Communication Conference*, San Francisco, California, 2014, p. Tu2G.2.
- [28] J. Zhao, "DFT-based offset-QAM OFDM with arbitrary orthogonal waveform generation," in *Optical Communication (ECOC 2013), 39th European Conference and Exhibition on*, 2013, pp. 1-3.
- [29] Z. Wang, Y. Qiao, Y. Xu, and Y. Ji, "Statistical characterization of the nonlinear noise in 2.8 Tbit/s PDM-16QAM CO-OFDM system," *Optics Express*, vol. 21, pp. 18034-18042, 2013/07/29 2013.
- [30] D. A. Cleland, A. D. Ellis, and C. H. F. Sturrock, "Precise modelling of four wave mixing products over 400 km of step-index fiber," *Electronics Letters*, vol. 28, pp. 1171-1173, 1992.

2.2 Advanced Transceiver Technologies for CO-OFDM Super-Channels

2.2.1 Non-Rectangular Perfect Reconstruction of Pulse Shaping Based ICI Reduction in CO-OFDM

In the past years, coherent optical-orthogonal frequency division multiplexing (CO-OFDM) has been an attractive technology in high speed communication, due to its inherent advantages of higher resilience towards chromatic dispersion and polarization mode dispersion, flexibility in accessing individual subcarriers in multi-user environment, and a simplified equalization scheme [1]. However, apart from the disadvantage of high peak-to-average ratio (PAPR), the CO-OFDM is very sensitive towards carrier frequency offset (CFO) [2], which will effectively introduce inter-carrier interference (ICI).

In CO-OFDM transmission demonstration, CFO estimation and compensation was carried out in [3-5]. However, in high speed CO-OFDM systems, residual uncompensated CFO always exists with Gaussian distribution [2]. It is crucial to minimize the residual CFO to not only avoid ICI, but also relax the complexity of the initial CFO estimator and enhance the receiver robustness against optical local oscillator instability [2, 6]. However, the algorithms for ICI mitigation are computationally demanding, and the implementation of such algorithms is highly not feasible due to the high speed nature of optical communications [6]. For an example, some real-time CO-OFDM transmission demonstrations were not able to include even the first stage CFO compensation due to the lack of resources in field programmable gate array (FPGA) [7, 8], unless a state-of-the-art FPGA with high capacity was utilized as the CO-OFDM receiver as demonstrated in [3]. An efficient approach in mitigating the impact of residual CFO is to use pulse shaping techniques with good time and frequency localization properties. Recently Li et al [9] introduced pulse shaping with root raised cosine (RRC) in optical OFDM, where RRC has demonstrated some improvements in comparison to rectangular pulse shape for receiver operating under the influence of residual CFO.

In this section, we are introducing short perfect reconstruction (orthogonal) pulse shapes in CO-OFDM, namely time-frequency localization maximization (TFL) and out-of-band energy minimization (OBE), and presenting an opportunity of taking a new approach in providing higher residual CFO tolerance with pure discrete pulse shapes. We will introduce RRC for comparison with TFL and OBE. The major advantages of the proposed short pulse shapes (TFL and OBE) are that: A) the method does not require additional overhead beyond adding cyclic prefix, and B) in the case of hardware implementation, the proposed method only requires additional multipliers at the transmitter and receiver, simply because TFL and OBE are short length filters essentially designed in discrete domain allowing short length block processing. However, RRC is an analogue pulse shape with infinite impulse response that matches the Nyquist criterion. In the case of implementation, truncation is required for RRC to achieve short pulse shape; consequently the discrete finite impulse response of the RRC pulse shape would not allow perfect reconstruction and will not meet the Nyquist criterion

2.2.1.1 Principle of proposed pulse shapes and impact of residual CFO

Pulse shaping allows the signal to spread in the time-frequency plane. Such technique is important in the case of time-frequency selective channels [10]. Since the pulse shapes are usually longer than each data block, the underlying transceiver requires polyphase decomposition and advanced equalization schemes. To maintain a minimum complexity, short perfect reconstruction pulse shapes will be used, which are shorter or equal than each data block [11].

- **Input-output relationship**

Information is carried by a sequence of complex symbols denoted $\{c_{m,n}\}_{(m,n)}$, where m is the subcarrier index, n is the block index. The symbols are assumed to be independent and identically distributed. Each $c_{m,n}$ is placed in the time-frequency plane at coordinates $(m/M, nN)$, where M is the number of subcarriers and N represents the number of sample per sub-channel symbol period. The transmitted signal can be written as a function of discrete time k :

$$s[k] = \sum_{(m,n)} c_{m,n} \gamma_{m,n}[k], \quad k \in \mathbf{Z}. \quad (1)$$

where \mathbf{Z} is the integer set, $\gamma_{m,n}[k]$ is a time-frequency shifted version of the prototype pulse shape $\gamma[k]$ defined as:

$$\gamma_{m,n}[k] = \frac{1}{\sqrt{M}} \gamma[k - nN] e^{j2\pi \frac{m}{M} k}, \quad \gamma[k] \in \ell_2 \mathbf{Z}. \quad (2)$$

where $\ell_2(\mathbf{Z})$ is the set of square summable sequences. A necessary condition for perfect reconstruction of the transmitted symbols is the linear independence of the vectors $\{\gamma_{m,n}\}$. This requires $N/M \geq 1$, but orthogonality and completeness are not mandatory [12].

Let x and y be two sequences of $\ell_2(\mathbf{Z})$, we define the inner product $\langle x, y \rangle = \sum_{k \in \mathbf{Z}} x^*[k] y[k]$ and the $\ell_2(\mathbf{Z})$ norm $\|x\| = \langle x, x \rangle^{1/2}$. At the receiver side, the dual family of $\{\gamma_{m,n}\}$ is written as $\{\tilde{\gamma}_{m,n}\}$ and we have:

$$\tilde{\gamma}_{m,n}[k] = \frac{1}{\sqrt{M}} \tilde{\gamma}[k - nN] e^{j2\pi \frac{m}{M} k}, \quad \tilde{\gamma}[k] \in \ell_2 \mathbf{Z}. \quad (3)$$

In the presence of an ideal channel, such that $r[k] = s[k]$, the received signal is projected on the dual family and if we let $(m,n) \neq (p,q)$, where the q^{th} received symbol on the p^{th} sub-channel can be written as:

$$\hat{c}_{p,q} = \langle \tilde{\gamma}_{p,q}, s \rangle = c_{p,q} \langle \tilde{\gamma}_{p,q}, \gamma_{p,q} \rangle + \sum_{(m,n) \neq (p,q)} c_{m,n} \langle \tilde{\gamma}_{p,q}, \gamma_{m,n} \rangle \quad (4)$$

We notice from this expression that perfect reconstruction of the transmitted symbols needs biorthogonality, namely $\langle \tilde{\gamma}_{p,q}, \gamma_{m,n} \rangle = \delta_{m,p} \delta_{n,q}$ for all (m,n) and (p,q) ; δ represents the Kronecker delta. If $\tilde{\gamma}[k]$ and $\gamma[k]$ are satisfying following equation $\tilde{\gamma}[k] = \gamma[k]$, a perfect reconstruction system is denoted as orthogonal.

In order to perform an N -size block processing, we restrict our analysis on short filters, that is to say $\tilde{\gamma}[k] = \gamma[k] = 0$, if $k > N - 1$ or $k < 0$. This particular condition allows an N -size block processing. The resulting transmission scheme can be efficiently realized thanks to the use of fast algorithms [13]. Thus, this generalizes the conventional OFDM transceiver by allowing non-rectangular pulse shapes while preserving a low complexity (detailed system description will be given in following section). If we denote $x[k]$, $0 \leq k \leq M - 1$, entering the cyclic prefix Insertion block, and its output as $y[k]$, $0 \leq k \leq N - 1$, then we have $y[k] = x[2M - N + k]$ for $0 \leq k \leq N - M - 1$ and $y[k] = x[N - M + k]$ for $N - M \leq k \leq N - 1$. The resulting N samples are weighted by $\gamma[k]$, $0 \leq k \leq N - 1$.

At the receiver side, the dual operation is performed in the filtering block to ensure perfect reconstruction of the transmitted symbols, that is to say $\hat{c}_{m,n} = c_{m,n}$ if $r[k] = s[k]$. In particular, cyclic prefix Folding block is

defined by the following: if we denote $x[k]$, $0 \leq k \leq N-1$ as entering cyclic prefix Folding block, and its output is $y[k]$, $0 \leq k \leq M-1$, then we have $y[k] = x[N-M+k]$ for $0 \leq k \leq 2M-N-1$ and $y[k] = x[k-(2M-N)] + x[k-(M-N)]$ for $2M-N \leq k \leq M-1$.

If the received signal $r[k]$ is equal to the transmitted signal $s[k]$, then the complex symbols $\{c_{m,n}\}$ can be exactly reconstructed provided that the following perfect reconstruction conditions are fulfilled:

$$\begin{aligned} \bullet \gamma[k]\tilde{\gamma}[k] + \gamma[k+M]\tilde{\gamma}[k+M] &= 1, \text{ for } 0 \leq k \leq N-M-1, \\ \bullet \gamma[k]\tilde{\gamma}[k] &= 1, \text{ for } N-M \leq k \leq M-1. \end{aligned} \quad (5)$$

Through this relation, one may recover the expression of rectangular pulse shape used for cyclic prefix based OFDM: if $\gamma[k] = 1$ for $0 \leq k \leq N-1$ and 0 otherwise and perfect reconstruction is satisfied when $\tilde{\gamma}[k] = 1$ for $N-M \leq k \leq N-1$ and 0 otherwise.

• CO-OFDM in the presence of residual CFO

As specified above, CO-OFDM is very sensitive towards residual CFO; assuming perfect frame synchronization and no sampling frequency offset, a simple relation can be established by the following expression:

$$r[k] = (\tilde{H}s)[k] + z[k] = s[k]e^{j2\pi\phi k} + z[k] \quad (6)$$

where \tilde{H} is the channel model, ϕ is the residual CFO, and $z[k]$ is a complex white Gaussian noise sequence. Taking into account (1), (4), and (6), we derive the expression of the q th estimated symbol on the p th subcarrier:

$$\begin{aligned} \hat{c}_{p,q} &= \langle \tilde{\gamma}_{p,q}, r \rangle = \sum_{k \in \mathbb{Z}} s[k] e^{j2\pi\phi k} \gamma_{p,q}^*[k] + \sum_{k \in \mathbb{Z}} z[k] \gamma_{p,q}^*[k] \\ &= \frac{1}{M} \sum_{k \in \mathbb{Z}} \sum_{(m,n)} c_{m,n} \gamma[k-nN] \tilde{\gamma}[k-qN] e^{j2\pi[(m-p)/M + \phi]k} + z_{p,q}. \end{aligned} \quad (7)$$

Using the hypothesis of short length filters, we notice that $\gamma[k-nN]\tilde{\gamma}[k-qN] = 0$ for $n \neq q$, so that there is no interference between OFDM symbols. Consequently, we can focus on a single OFDM symbols estimation and omit n and q indices:

$$\hat{c}_p = \frac{1}{M} \sum_{m=0}^{M-1} c_m \underbrace{\sum_{k \in \mathbb{Z}} \gamma[k] \tilde{\gamma}[k] e^{j2\pi[(m-p)/M + \phi]k}}_{A_{m,p}^\phi} + z_p = \frac{1}{M} \underbrace{c_p A_{p,p}^\phi}_{s_p} + \frac{1}{M} \underbrace{\sum_{m=1:m \neq p}^{M-1} c_m A_{m,p}^\phi}_{i_p} + z_p \quad (8)$$

where s_p is the useful part of the signal, i_p is ICI term, and z_p is the filtered noise. The useful part of the signal should be maximized and the rest should be minimized in terms of mean power. First of all, in presence of a small residual CFO such that $\phi < 1/M$, with overlapped frequency domain signals, ICI mitigation suggests using frequency localized pulse shapes. On the other hand, the presence of additive white Gaussian noise justifies the use of orthogonal signaling (*i.e.* matched filtering) [14].

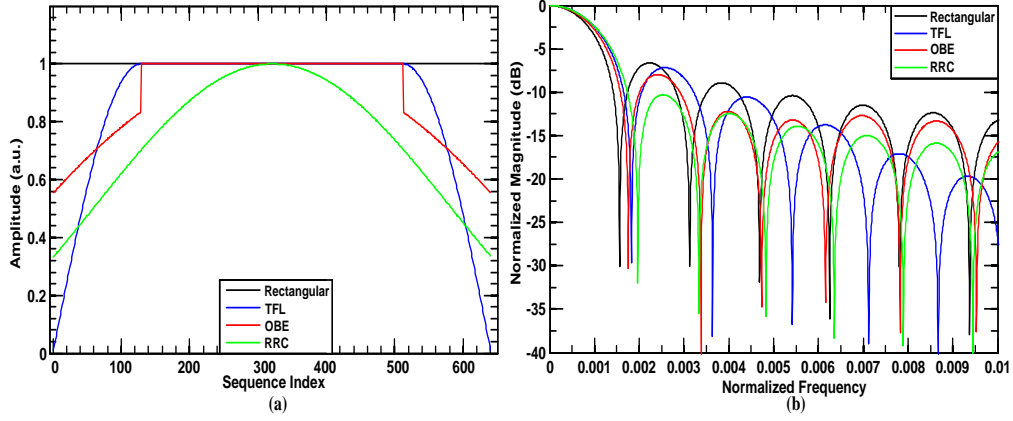


Figure 2.29 Rectangular (black), TFL (blue), OBE (red) and RRC (green, $\alpha = 1$) depiction of (a) impulse response and (b) frequency response. Rectangular has very high energy sidelobes. TFL pulse shape exhibits better localization in time and frequency than OBE. The difference between TFL and OBE is that TFL has higher sidelobe energy and quick energy decay; on the other hand OBE has lower sidelobe energy and slow energy decay. RRC shows good sidelobe energy, however it introduces high inter-symbol interference

- **Perfect reconstruction filters**

In this section, we will describe the two families of prototype filters [15] that are used herein over time-frequency dispersive channel, namely rectangular pulse shape and short perfect reconstruction filters.

The CO-OFDM biorthogonal rectangular pulse shapes can be defined as:

$$\begin{aligned} \gamma_{\text{RECT}}[k] &= \begin{cases} 1, & \text{if } 0 \leq k \leq N-1, \\ 0, & \text{otherwise,} \end{cases} \\ \tilde{\gamma}_{\text{RECT}}[k] &= \begin{cases} 1, & \text{if } N-M \leq k \leq N-1, \\ 0, & \text{otherwise.} \end{cases} \end{aligned} \quad (13)$$

The first $N - M$ coefficients of γ_{RECT} form the cyclic prefix in order to mitigate inter-symbol interference introduced by time-dispersive channels. At the receiver side, the cyclic prefix is removed by $\tilde{\gamma}_{\text{RECT}}$. The time and frequency response of the rectangular pulse shape is shown in Figure 2.29(a) and (b), respectively.

The prototype filters described in [15] are derived from two optimization criteria: TFL and OBE. Using $\Delta = N - M$, closed-form expressions are given for both filters:

$$\gamma_{\text{TFL}}[k] = \begin{cases} \sin\left(\frac{(2k+1)\pi}{4\Delta}\right) & \text{if } 0 \leq k \leq \Delta-1, \\ 1 & \text{if } \Delta \leq k \leq M-1, \\ \sin\left(\frac{(2(\Delta-k)+1)\pi}{4\Delta}\right) & \text{if } M \leq k \leq N-1, \\ 0 & \text{otherwise.} \end{cases} \quad (15)$$

$$\gamma_{\text{OBE}}[k] = \begin{cases} \cos\left(\tilde{a} + \tilde{b} \frac{(2k+1)}{2\Delta}\right) & \text{if } 0 \leq k \leq \Delta-1, \\ 1 & \text{if } \Delta \leq k \leq M-1, \\ \cos\left(\tilde{a} + \tilde{b} \frac{(2k+1)}{2\Delta}\right) & \text{if } M \leq k \leq N-1, \\ 0 & \text{otherwise.} \end{cases} \quad (16)$$

where \tilde{a} and \tilde{b} are two constants given in [15] and depend on the ratio of M / Δ . The time-frequency analysis of the prototype pulse shapes is shown in Figure 2.29, and plotted against rectangular pulse as a reference. From Figure 2.29, TFL pulse shape exhibits better localization in time and frequency than OBE.

In principle, both OBE and TFL are short length, perfect reconstruction (orthogonal) and have symmetric impulse response. The difference between these pulse shapes is that TFL has higher sidelobe power (lower than rectangular pulse shape) and quick power decay; on the other hand OBE has lower sidelobe power and slow power decay.

Since RRC pulse shape is investigated here, OBE filter may be directly compared with RRC because they share the same optimization criterion. But it is important to understand that the RRC pulse shape is a continuous time function, hence it has to be truncated in order to fit an N coefficients impulse response. Such a truncation prevents the perfect reconstruction and yield inter-symbol interference [16]. A comparison between TFL and RRC is not equitable because they are not optimized from the same criterion, where the former is optimized jointly in time and frequency resulting in minimization of second order moment with the constraint of N non-zero coefficients. The RRC pulse shape is shown in Figure 2.29

2.2.1.2 System Overview

In order to evaluate the proposed method of non-rectangular perfect reconstruction pulse shapes, an end-to-end extensive simulation is carried out with 40 Gbit/s quadrature phase shift keying (QPSK) CO-OFDM system. The simulation system is constructed in MATLABTM, as shown in Figure 2.30.

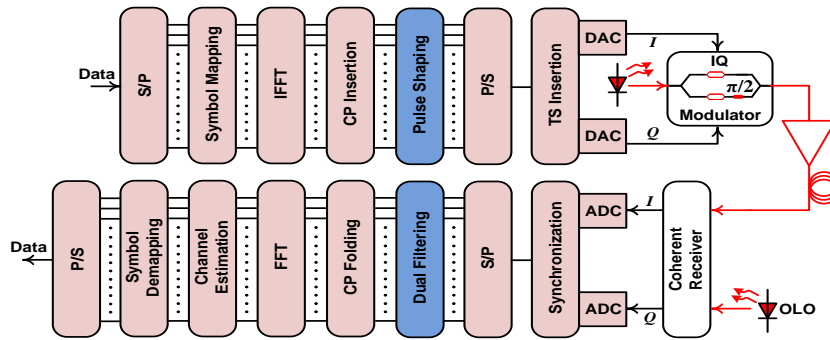


Figure 2.30 System diagram of CO-OFDM with proposed pulse shaping and receiver dual filtering. Acronyms- S/P: serial-to-parallel, IFFT: inverse fast Fourier transform, CP: cyclic prefix, P/S: parallel-to-serial, TS: training symbol, DAC: digital-to-analogue converter, I: in-phase, Q: quadrature, OLO: optical local oscillator, ADC: analogue-to-digital converter, and FFT: fast Fourier transform.

As illustrated in Figure 2.30, the serial data stream is converted to $M = 512$ parallel structured data prior to being mapped into gray coded QPSK modulation format. The QPSK data is then transformed into OFDM signal by performing IFFT of size 1024 operation, apart from the data subcarriers, the rest are padded with zeros for oversampling purpose. The duration of OFDM symbol is 40.1 ns. A cyclic prefix is then appended to the OFDM signal at the rate of 25% to combat inter-symbol interference in long haul transmission. The extended OFDM symbol then weighted with various pulse shapes, including rectangular, RRC with α of 0.1, 0.2, and 1, and the newly introduced TFL and OBE.

After the insertion of training symbol, the total transmitting symbols are 200. The electrical OFDM signal is optically modulated by IQ modulator, and transmitted over 400 km to 3600 km of single mode fiber (SMF), with loss coefficient: 0.2 dB/km, PMD coefficient: 0.1 ps/km^{1/2}, CD coefficient: 16 ps/nm.km, and optical fiber nonlinearity coefficient: 1.22 W⁻¹km⁻¹. The optical fiber loss is compensated for every 80 km span by utilizing erbium-doped fiber amplifier (EDFA) with 16 dB gain and noise figure of 6 dB. The laser phase noise is modeled using the Wiener-Levy process, expressed as the variance $\sigma^2 = 2\pi\nu t$, where ν is the combined laser linewidth and t is the time difference between two samples [17]. In this simulation, the amplified spontaneous emission (ASE) noise is added relative to each fiber span (80 km). At the receiver, the coherently detected signal is first frame synchronized and sampling frequency offset is not induced to purely study the mitigation of ICI due to residual CFO. To achieve optimum pulse shaping, a receiver dual filtering with the same shape as the transmitted is utilized for weighting. Rest of the receiver process is

exactly the reverse of the transmitter except for the channel estimation and equalization process with single-tap per subcarrier filter.

2.2.1.3 Results and Discussions

Figure 2.31 presents the optical launch power analysis and the signal quality is quantified through the usage of Q-factor based on direct error counting. The CO-OFDM transmission with rectangular pulse shape without any CFO is the benchmark, in other words it is the ideal received signal without ICI. Then, we deliberately introduce a residual CFO of 2 MHz and investigate the additional tolerance that can be provided by the proposed pulse shapes.

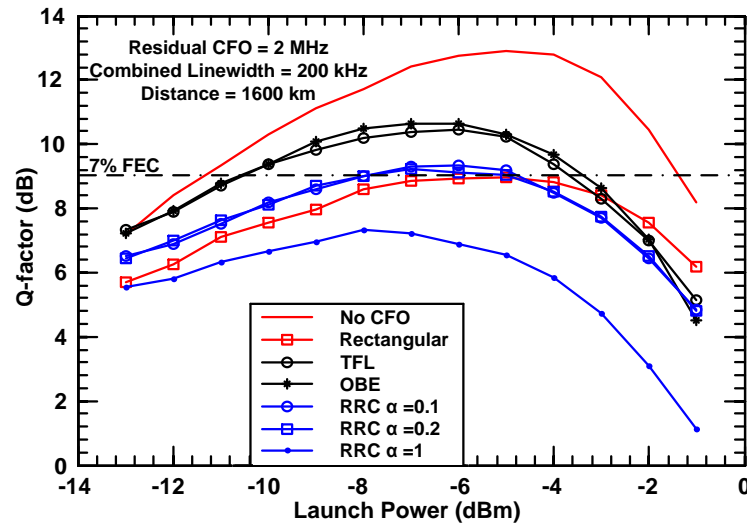


Figure 2.31 Optical launch power investigation with no CFO for rectangular pulse shape, and 2 MHz residual CFO across rectangular, TFL, OBE and RRC. α is 0.1, 0.2, and 1 for RRC pulse shape. The transmission distance is 1600 km.

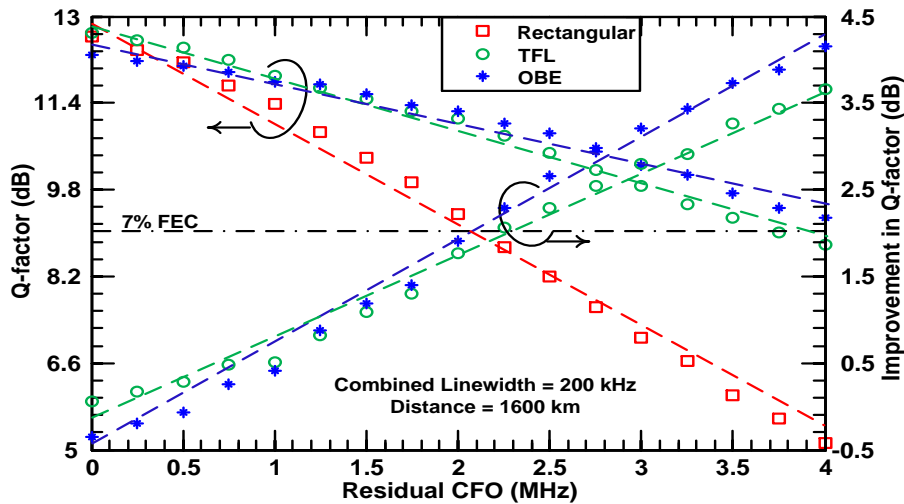


Figure 2.32 Impact of utilizing rectangular, TFL and OBE pulse shapes under varying residual CFOs at transmission distance of 1600 km.

By utilizing a rectangular pulse shape and 2 MHz residual CFO, the Q-factor at the optical launch power of -5 dBm deteriorated from 12.9 dB to 8.9 dB, which clearly showed the criticalness of ICI and resulted in dropping below the 7% forward error correction (FEC) limit of 9.1 dB [19]. In the case of RRC pulse shape, the Q-factor at -6 dBm optical launch power for α of 0.1 and 0.2 is 9.3 dB and 9.1 dB, respectively, unveiling the optimum α as 0.1 and consequently agreeing with [9]. However, increasing the α to 1 introduces excessive inter-symbol interference, resulting in very worsen Q-factor, where at -8 dBm optical launch

power, the Q-factor is 7.3 dB. One important aspect that needs to be addressed here is that the optimum optical launch power point decreases with respect to the increasing α . This is due to the proportional increase of PAPR relative to the increase in α . Now we have shown the impact of applying RRC and confirmed the optimum α , although applying RRC resulted in Q-factor above the FEC limit, but the improvement is rather insignificant. Henceforth, the investigation on RRC will be dropped from rest of the paper.

It is clear from Figure 2.31 that both TFL and OBE pulse shapes achieved the highest Q-factor under residual CFO of 2 MHz. At the optical launch power of -6 dBm, the Q-factor for TFL and OBE is 10.5 dB and 10.7 dB, respectively. The Q-factor improvement with respect to the rectangular pulse shape is 1.6 dB and 1.8 dB for TFL and OBE, respectively. It is clear that OBE provides better performance compared to TFL, although the difference is small. The superiority of OBE over TFL is due to the lower energy of sidelobes, as shown in Figure 2.29(b). Since 2 MHz residual CFO was purely chosen under arbitrary condition, it is important to understand the credibility of the proposed pulse shapes. Therefore, we have conducted a detailed investigation of the performances of rectangular, TFL, and OBE pulse shapes over residual CFO(x), $0 \leq x \leq 4$ MHz; for the transmission span of 1600 km, as shown in Figure 2.32. At CFO of 0, all three pulse shapes exhibit almost similar performance. For residual CFO > 0.5 MHz, rectangular pulse shape performs worse than both TFL and OBE with continuous degradation in Q-factor with a very sharp slope, effectively demonstrating the rectangular pulse shape's sensitivity towards ICI. Since TFL pulse shape's side lobe is lower than rectangular pulse shape and higher than OBE, it provides an optimum compensation for ICI up to 1 MHz. However, OBE closely follows the trend of TFL up to 1 MHz. Beyond 1 MHz, due to OBE's much lower power based sidelobes, it exhibits better resilience towards increasing ICI compared to TFL and rectangular.

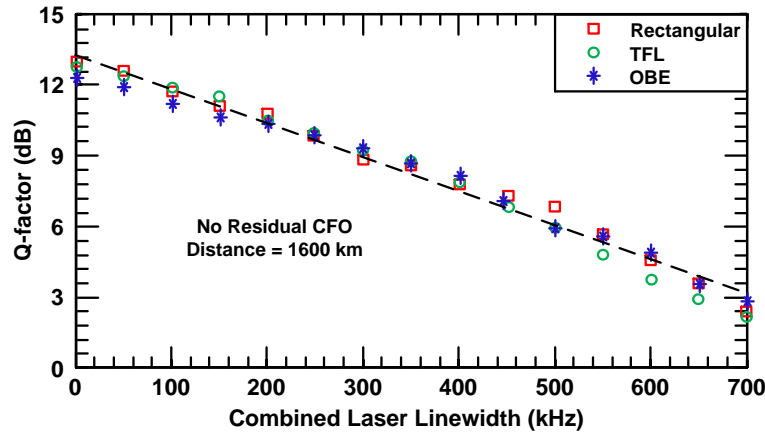


Figure 2.33 Rectangular, TFL and OBE pulse shapes behavior under continuous broadening of combined linewidth with no residual CFO, and at transmission distance of 1600 km

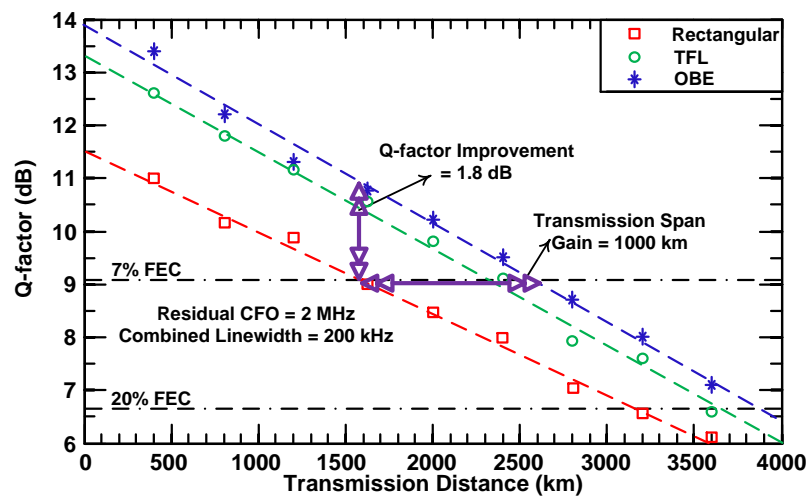


Figure 2.34 Transmission investigation of Rectangular, TFL and OBE pulse shapes with 2 MHz residual CFO and a combined linewidth of 200 kHz.

This investigation has revealed the possibilities of using TFL and OBE under selected conditions based on a CO-OFDM receiver performance. For an example, if the residual CFO is < 1 MHz and > 1 MHz, TFL and OBE can be employed, respectively. However, it is important to note that in a real field deployed system, over a span of time, the residual CFO will increase, although not indefinitely. Therefore, it is advisable to utilize OBE as it performs similar to rectangular and TFL pulse shapes for residual CFOs of < 0.5 MHz and < 1 MHz, respectively, and demonstrates exemplary performance for residual CFO beyond 1 MHz. The limit of CFO for OBE is approximately 4 MHz for 1600 km at the specified FEC limit. Beyond this limit, the transmission distance has to be proportionally shortened, or more robust equalization schemes have to be utilized, and such optimization is beyond the scope of this paper.

Linewidth is a major factor that contributes to phase noise and as well as the quality of a specific laser. In order to determine if the quality of an optical LO at the receiver of CO-OFDM can be flexible in terms of quality, next phase of the investigation will be covering the impact of linewidth broadening on the proposed pulse shapes under the condition of no CFO. The rationale for no CFO is to purely study the effect of phase noise. Figure 2.33 illustrates the performance of rectangular, TFL and OBE pulse shapes under no CFO, at 1600 km transmission and expanding combined laser linewidth that proportionally increases the phase noise. It is clear that additional phase noise induced by higher linewidth lasers have very similar impact on all three pulse shapes under no CFO. Hence, it is clear that the proposed pulse shapes behaves closely to the rectangular pulse shape and can be employed for ideal receivers, although ideal receivers are highly unlikely to occur in a practical system. Since it is well known that physical

hardware, both optical and electrical will always introduce offsets and distortions, Figure 2.32 has already shown the usefulness of the proposed pulse shapes

Finally, CO-OFDM mostly drawn great interest in the area of long-haul optical communication systems [20]. Therefore, in the first framework of these new pulse shapes, it is important to stress the proposed system and investigate its potential transmission ability. Figure 2.34 presents the transmission investigation for rectangular, TFL, and OBE pulse shapes from 400 km to 3600 km spans. The residual CFO is fixed at 2 MHz and a combined linewidth of 200 kHz. Taking 7% FEC as the first benchmark, rectangular pulse shape is capable of achieving this reference point for slightly less than 1600 km transmission. However, TFL and OBE pulse shapes achieved Q-factor improvements of 1.6 and 1.8 dB, respectively at the same transmission point. In the case of TFL and OBE pulse shapes at 7% FEC point, the achievable distances are 2400 km and 2600 km, respectively. It is clear that by employing OBE pulse shape, the improvement of transmission span is 1000 km with respect to rectangular pulse shaped system, which effectively translates into a ~62% gain. Long haul system can also be designed by taking 20% soft decision (SD)-FEC as the benchmark that results in Q-factor of 6.75 dB [21]. In the case of 20% SD-FEC, rectangular pulse shape is still able to reach a 3100 km transmission distance. For TFL pulse shape, the 20% SD-FEC meets at the span of 3500 km and OBE effectively has not reached the threshold of 20% SD-FEC even up to 3600 km transmission, thus showing the credibility of the proposed pulse shapes.

2.2.1.4 Discussion

A simple residual CFO compensation method was proposed herein, based on short non-rectangular perfect reconstruction pulse shapes for CO-OFDM. Employing both OBE and TFL pulse shapes will significantly reduce the receiver complexity compared to employing exhaustive algorithms. The investigation revealed, through simulations, that TFL performs better for residual CFO < 1 MHz and vice versa for OBE. However, employing OBE for CFO < 1 MHz does not introduce significant penalty, and since the optical LO for CO-OFDM will drift over time, OBE would be the ideal pulse shape in real-time condition. Finally, by employing OBE, a transmission span of 3600 km could be achieved without hitting the 20% SD-FEC limit.

2.2.2 Comparison of Bit Error Rate Estimation Methods for QPSK CO-OFDM Transmission

The bit error rate (BER) in CO-OFDM systems can be estimated in numerical investigations using Monte Carlo simulation and in experiments by directly counting the number of errors at the receiver. The corresponding Q-factor is calculated using the inverse complementary error function. However, this method relies on a large number of statistical samples and is time-consuming, especially if the signal quality is high or extensive optimization is required. Therefore, it is highly desirable and practically important to develop efficient indirect numerical and statistical methods for evaluating CO-OFDM system performance.

For coherent communication systems utilizing multi-level amplitude and phase signals, the error vector magnitude (EVM) is commonly used as a fast measure of the received digital signal's quality [22, 23]. The EVM describes the effective distance of the received complex symbol from its ideal position in the constellation diagram. In an additive white Gaussian noise channel the association between EVM and BER has been determined theoretically [23]. The EVM can also be estimated without knowing the transmitted data by performing hard decision on the received symbols. Based on the assumption that in-phase and quadrature components of the received QPSK signal have Gaussian distribution [24], a few other relevant methods of evaluating the signal quality in QPSK system have been proposed and investigated in [25]. Recently, a novel statistical BER estimation method for QPSK CO-OFDM transmission based on the probability density function of the received QPSK symbols' phase has also been proposed in [26].

In this section, we experimentally study the statistical properties of a QPSK modulated OFDM signal and compare for the first time different BER estimation methods for wavelength division multiplexing (WDM) CO-OFDM transmission. We show that the distribution of the received QPSK symbols' phase in each

quadrant of the constellation diagram is essentially Gaussian. Furthermore, the statistical approach [26] offers the most accurate estimate of the system performance in comparison with other well-known approaches.

2.2.2.1 Experimental setup and results

For studying the statistical properties of a QPSK modulated OFDM signal and comparison of different BER estimation methods, we set up a WDM CO-OFDM transmission system as shown in Figure 2.35. This comprised a laser grid of five standard DFB lasers on a 100 GHz grid which were substituted in turn by a 100 kHz linewidth external cavity laser. The DFBs were located between 193.5 to 193.9 THz. Twenty additional loading channels (10 GHz bandwidth) were generated using an ASE source which was spectrally shaped using a WaveShaper wavelength selective switch (WSS). These loading channels were spread symmetrically around the test wavelengths so that the total bandwidth of the transmission signal was 2.5 THz. A wideband filter was used to filter out-of-band ASE noise at the transmitter. The transmission path is an acousto-optic modulator based re-circulating loop consisting of 4 x 100 km spans of Sterlite OH-LITE (E) fiber, having 18.9 to 19.5 dB insertion loss (per 100 km span) and dual stage amplifiers (EDFA, 5dB-6 dB of noise figure). The loop switch was located in the mid-stage of the first EDFA and a gain flattening filter was placed in the mid stage of the third EDFA. After fiber propagation the signal was filtered using a 4.2 nm flat topped filter and coherently detected. The received electrical signals were then sampled by a real-time oscilloscope at 80 GS/s and processed offline in MATLAB.

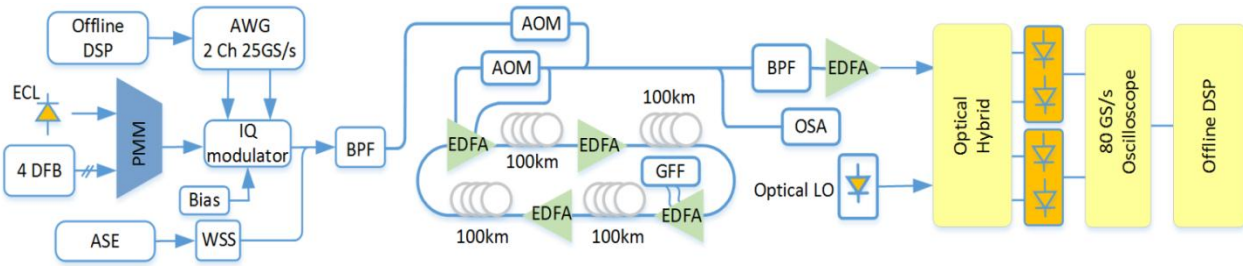


Figure 2.35 Schematic of experimental setup of WDM CO-OFDM transmission. ECL: external cavity laser, PMM: polarization maintaining multiplexer, WSS: wavelength selective switch, DFB: distributed feedback laser, BPF: band-pass filter (optical), AOM: acousto-optic modulator, GFF: gain flattening filter, OSA: optical spectrum analyzer, LO: local oscillator (optical), EDFA: Erbium-doped fiber amplifier

The OFDM signals (400 symbols each of 20.48 ns length, 2% cyclic prefix) encoded with QPSK modulation format were generated offline in MATLAB using an IFFT size of 512, where 210 subcarriers were filled with data and the remainder zeros giving a potential line rate of 20 Gb/s per channel. The DSP at the receiver included combining x- and y-polarizations using the maxima-ratio combining method [27], frequency offset compensation, chromatic dispersion compensation using a frequency domain equalizer (overlap-and-save method), channel estimation and equalization with the assistance of initial training sequence (2 training symbols every 100 symbols), common phase error (CPE) compensation by distributing 8 pilots uniformly across the OFDM band [28], giving a net data rate of 17.4 Gbit/s

Figure 2.36 shows the histograms of in-phase and quadrature components of the received QPSK signal for the center channel. The Gaussian fitting is obtained by calculating the mean and standard deviation (STD) of the received statistical samples ($\sim 8 \times 10^5$ in total). Herein, the well-known Kolmogorov-Smirnov test (K-S test) was applied to define if a statistical signal has a Gaussian-like distribution. The Kolmogorov-Smirnov statistic (KSSTAT) for a given cumulative distribution function $F(x)$ is defined as:

$$D = \sup |F_n(x) - F(x)| \quad (1)$$

where \sup is the supremum, $F_n(x)$ is the empirical distribution function for n observations of the statistical signal. A statistical signal can be assumed to have a Gaussian distribution if $D \leq 0.05$. The Gaussian fitting and KSSTAT values shown in Figure 2.36 indicate that at this power level the nonlinear interference noise

(NLIN) in CO-OFDM transmission deviates from Gaussian distribution. The obtained result herein agrees well with a recent study reported in [29], indicating that the Gaussian assumption of NLIN, which is the key in the derivation of closed-form expression for the nonlinear performance of CO-OFDM [30] is, in general, not satisfied exactly. On the other hand, as shown in Figure 2.37, the distribution of the received QPSK symbols' phase in each quadrant of the constellation diagram is essentially Gaussian. This result agrees well with numerical results presented in [26], indicating that the nonlinear interaction of the ASE noise and signal induces the distribution of QPSK phases in OFDM systems (rather than the in-phase/quadrature components) to be Gaussian.

Next, we investigate the performance of various BER estimation methods. Herein, we take into account the data-aided EVM (Q(EVM1), nondata-aided EVM (Q(EVM2)), two relevant methods proposed in [25] (Q-factor 1, Q-factor 2 or Q1, Q2) and the statistical method proposed in [26, 31] (Q-factor 3 or Q3).

The Q1, Q2 methods are based on the assumption that the four components of a QPSK signal are Gaussian distributed. Following the same well known approach for calculating the conventional Q-factor for on-off-keying signals, the Q1 method defines the Q-factors of the in-phase and quadrature components of the received QPSK signals by:

$$Q_{Re} = \frac{\langle c_{k,Re}(c_{k,Re} > 0) \rangle - \langle c_{k,Re}(c_{k,Re} < 0) \rangle}{\sigma(c_{k,Re} > 0) + \sigma(c_{k,Re} < 0)} \quad (2)$$

$$Q_{Im} = \frac{\langle c_{k,Im}(c_{k,Im} > 0) \rangle - \langle c_{k,Im}(c_{k,Im} < 0) \rangle}{\sigma(c_{k,Im} > 0) + \sigma(c_{k,Im} < 0)} \quad (3)$$

where $\sigma(\cdot)$ denotes the STD of the statistical samples, $\langle \cdot \rangle$ denotes the expectation operator, $C_{k,Re}$, $C_{k,Im}$ are the real and imaginary parts of the k^{th} received QPSK symbol (C_k). The BER then can be obtained by using the estimations from both in-phase and quadrature components:

$$BER = \left\langle \frac{1}{2} \operatorname{erfc} \left(\frac{Q_{Re}}{\sqrt{2}} \right), \frac{1}{2} \operatorname{erfc} \left(\frac{Q_{Im}}{\sqrt{2}} \right) \right\rangle \quad (4)$$

The Q2 method is based on the estimation of the ratio between the mean and the STD value of each constellation point. For the symbol in the first quadrant, the Q-factors are:

$$Q_{1,Re} = \frac{\langle c_{k,Re}(c_{k,Re} > 0, c_{k,Im} > 0) \rangle}{\sigma(c_{k,Re} > 0, c_{k,Im} > 0)} \quad (5)$$

$$Q_{1,Im} = \frac{\langle c_{k,Im}(c_{k,Re} > 0, c_{k,Im} > 0) \rangle}{\sigma(c_{k,Re} > 0, c_{k,Im} > 0)} \quad (6)$$

The overall BER can be obtained by using $Q_{i,Re}$ and $Q_{i,Im}$, $i = 1, 2, 3, 4$ of all the constellation symbols:

$$BER = \left\langle \frac{1}{2} \operatorname{erfc} \left(\frac{Q_{i,Re}}{\sqrt{2}} \right), \frac{1}{2} \operatorname{erfc} \left(\frac{Q_{i,Im}}{\sqrt{2}} \right) \right\rangle \quad (7)$$

In contrast to Q1 and Q2 the statistical method Q3 [26] is based on the assumption that the received QPSK symbols' phases in CO-OFDM system are Gaussian distributed. As a result, Q3 estimates the BER as:

$$BER = \frac{1}{8} \sum_{k=1}^4 \left[\operatorname{erfc} \left(\frac{\phi_k - \theta_k + \pi/4}{\sigma_k \sqrt{2}} \right) + \operatorname{erfc} \left(\frac{\theta_k + \pi/4 - \phi_k}{\sigma_k \sqrt{2}} \right) \right] \quad (8)$$

where ϕ_k and σ_k denote the means and standard deviations of the received phases in the k^{th} quadrant ($k=1, 2, 3, 4$), θ_k is the phase angle of the k^{th} ideal QPSK symbol, and erfc is the scaled complementary error function.

The aforementioned BER estimation methods for WDM CO-OFDM transmission are compared in Figure 2.38(a) for the center channel and in Figure 2.39 for the #2 channel. Similar results, which were obtained for other modulated channels, are not shown here. The blue line with circle markers (Q(BER)) is the

reference result derived directly from the BER from error counting following OFDM processing of 10 recorded traces (~106 bits in total) for each data point. The red line (Q3) shows the result obtained using the expression (8) [26]. In Figure 2.38 only a small mismatch (< 0.2 dB) between Q(BER) and Q3 is observed, indicating that this BER estimation method is highly accurate. In addition, as Q3 is based on the assumption that the received symbols' phases are Gaussian distributed, this method is tolerant to residual CPE as the residual CPE, which is common to all subcarriers, affects only the mean but not the variance of the symbols' phases. This phenomenon is confirmed by the simulated results for the back-to-back case (AWGN channel) shown in the Figure 2.40. Without the laser phase noise, Q3 offers slightly worse performance in comparison to other methods because in the AWGN channel the symbols' phases do not follow a Gaussian distribution [32]. However, in the presence of the laser phase noise Q3 offers the best performance (Figure 2.40(b)), because the random phase noise makes the distribution of the QPSK phases conform more closely to a Gaussian distribution as a result of the central limit theorem. As a result, Q3 still offers an excellent performance even in the ASE limited regime.

On the other hand, all the other BER estimation methods, namely EVM (data-aided, nondata-aided), Q-factor 1 and Q-factor 2, overestimate the system performance by approximately 0.7 to 1dB. Moreover, unlike Q3 method, Q(EVM), Q1, Q2 methods are sensitive to residual CPE because the residual CPE strongly affects the distributions of the in-phase and quadrature components of the QPSK signal.

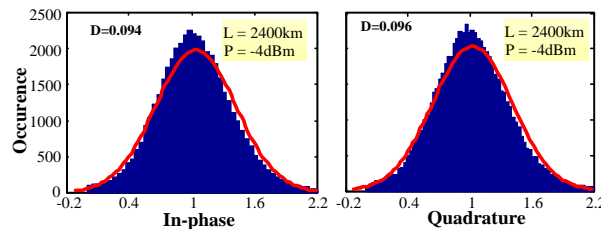


Figure 2.36 Histograms of in-phase and quadrature components of the received QPSK symbols in the first quadrant. Gaussian fitting is superimposed to each histogram; KSSTAT values are also included in each histogram

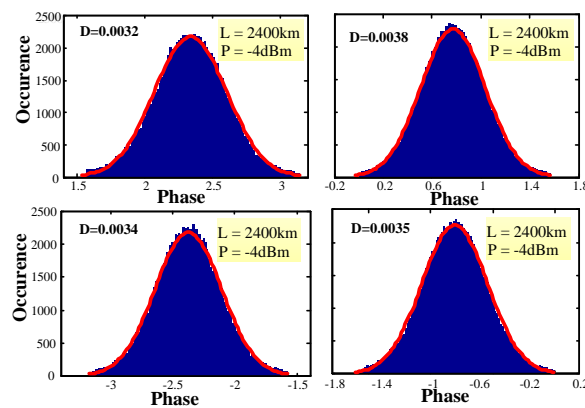


Figure 2.37 Histogram of the received QPSK symbols' phase of the center channel in four quadrants of the constellation diagram

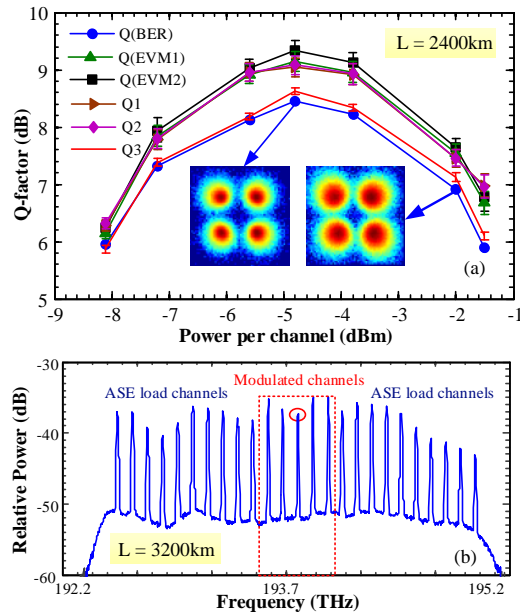


Figure 2.38 (a) - Q-factor values for the center channel as a function of the launch power at 2400km, (b) – received optical spectrum at 3200km.

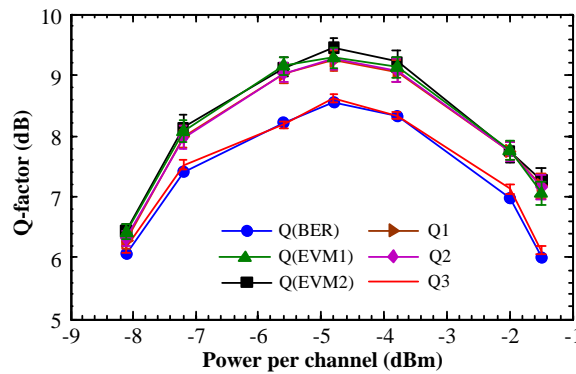


Figure 2.39 Q-factor values for the #2 channel as a function of the launch power at 2400km

Figure 2.41 shows the STDs obtained using considered here BER estimation methods as a function of the number of processed statistical symbols in each trace (N) when processing 20 recorded traces. When $N > 10^3$ the STD of Q3, which is only around 0.1 dB, is the smallest among those obtained with BER estimation methods studied here. This result indicates that the statistical BER estimation method proposed in [26] can be applied effectively with a relatively small number of received symbols ($\sim 10^3$) in comparison with other methods, offering a fast and accurate BER estimation method for QPSK CO-OFDM transmission.

2.2.2.2 Discussion

We have experimentally investigated the statistical properties of QPSK signal and compared various BER estimation methods for WDM CO-OFDM transmission. Experimental results reveal that the most accurate estimate of the system performance was achieved with the statistical method based on a Gaussian approximation of the received phase noise statistics.

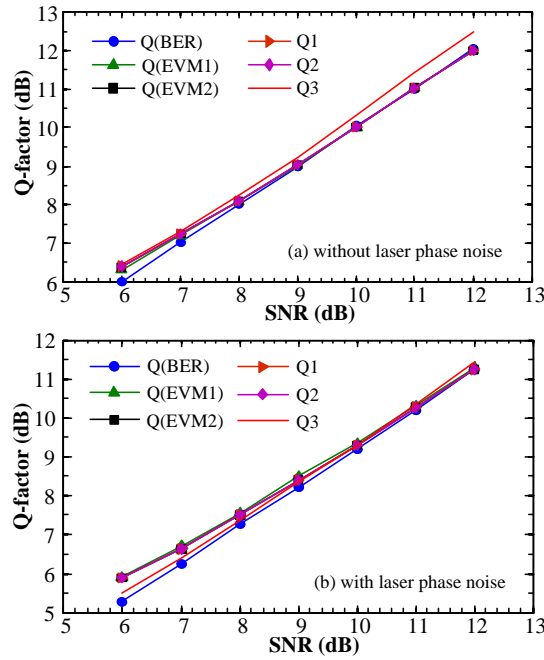


Figure 2.40 Performance comparison of BER estimation methods in the back-to-back case (simulation results), without (a) and with (b) the laser phase noise, the combined laser linewidth is 200 kHz

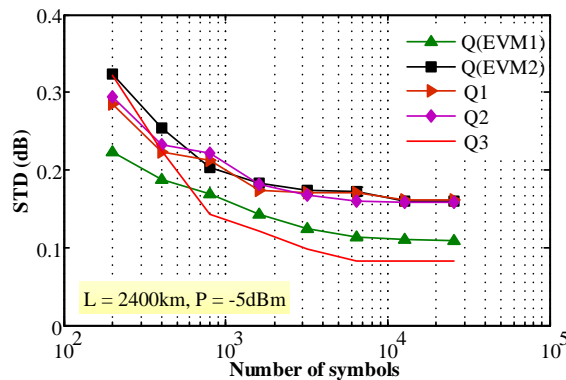


Figure 2.41 STD of the Q-factor obtained using different BER estimation methods as a function of the number of processed symbols.

2.2.3 Decision-Directed-Free Blind Phase Noise Estimation for CO-OFDM

Due to the long symbol duration CO-OFDM is sensitive to laser phase noise, which changes rapidly symbol-by-symbol. The impact of laser phase noise will introduce both common phase error (CPE) and inter-carrier interference (ICI) [33], which significantly degrades the system performance. Therefore, it is crucial that the laser phase noise is rigorously tracked, estimated and effectively compensated.

The laser phase noise impairment can be effectively mitigated by compensating the CPE using pilot subcarriers across the OFDM band [34]. However, this technique reduces the spectral (SE). To address this issue, several approaches have been proposed. In [35] a data-dependent pilot-aided technique was introduced to reduce the overhead due to pilot subcarriers by a factor of 2. In [36], a blind phase noise compensation (PNC) method has been proposed based on a decision-directed (DD) algorithm. However, this technique suffers significantly from error propagation, and thus, it cannot be applied in the presence of a large laser phase noise. In [37] the concept of blind phase search (BPS) was proposed, which can be applied effectively without suffering from error propagation. However, this technique also relies on DD

(to estimate the mean-square-error) and a large number test phases (16 to 32) are required to achieve good performance. To conclude, existing blind PNC techniques based on BPS or DD are either too complex or seriously affected by error propagation, and thus are not suitable for practical implementation.

In this section, we propose and experimentally demonstrate a hardware efficient decision-directed free (DDF) blind phase noise estimation method, which is also unaffected by error propagation. We introduce a novel cost function, which allows the CPE to be accurately estimated using just three test phases. The performance of the proposed technique is compared with pilot-aided (PA), DD and BPS compensation techniques

2.2.3.1 Proposed PNC technique for CO-OFDM and simulation result

By assuming perfect FFT window synchronization, channel estimation and frequency offset compensation, the received OFDM signal $R_{m,k}$ can be expressed as [34]:

$$R_{m,k} = S_{m,k} \exp(j\Phi_m) + \varepsilon_{m,k}, \quad (1)$$

where $S_{m,k}$ is the modulated data of the k^{th} subcarrier in the m^{th} symbol before transmission, Φ_m is the CPE for the m^{th} symbol due to laser phase noise or phase shifts acquired during optical fiber transmission, $\varepsilon_{m,k}$ represents residual inter-channel interference and random Gaussian noise.

In order to estimate the CPE we propose the following cost function, which is the mean value of the squared product of the projections of real and imaginary parts after rotation by a phase angle ϕ :

$$F_m(\phi) = \left\langle \text{Re}(R_{m,k} \cdot e^{-j\phi})^2 \cdot \text{Im}(R_{m,k} \cdot e^{-j\phi})^2 \right\rangle_k, \quad (2)$$

where $\langle \cdot \rangle$ stands for the averaging operation over all of the subcarriers in the m^{th} symbol.

For squared QAM modulation formats with identical probabilities of constellation points, the proposed cost function reaches its maximum value at $\phi = \Phi_m$. This phenomenon can be explained by the fact that ideal squared QAMs provide a “balance” between the real and imaginary parts of constellation points, thus, maximizing the mean value of the squared product of the projections of real and imaginary parts. For simplicity we consider in the following analysis the 4-QAM (QPSK) modulation format with constellation points $(\pm 1 \pm j)$. In this case, the expression (2) can be written as:

$$F_m(\phi) = 4 \cdot \left\langle (\cos(\Phi_m - \phi + \pi/4) + \eta_{1,k})^2 (\sin(\Phi_m - \phi + \pi/4) + \eta_{2,k})^2 \right\rangle_k, \quad (3)$$

where $\eta_{1,k}, \eta_{2,k}$ are two random Gaussian variables with zero means and variances $\langle \eta_{1,k}^2 \rangle = \langle \eta_{2,k}^2 \rangle = 1/(2 \cdot \text{SNR})$.

Straightforward calculations show that:

$$F_m(\phi) = 0.5 \cos(4\phi - 4\Phi_m) + (0.5 + 2/\text{SNR}) \quad (4)$$

Extending this result for higher order QAM modulation formats, the cost function (2) can be approximated as:

$$F_m(\phi) = A \cos(4\phi - 4\Phi_m) + B, \quad (5)$$

where A, B, Φ_m are three variables to be determined. Knowing the form of the cost function, the CPE (Φ_m) can be easily defined using just three test phases, for example, $0, \pi/4$ and $\pi/8$ as follows:

$$B = (F_m(0) + F_m(\pi/4))/2, \quad A = \sqrt{(F_m(0) - B)^2 + (F_m(\pi/8) - B)^2} \quad (7)$$

$$\Phi_m = 0.25 \cdot \text{sgn}(B - F_m(\pi/8)) \cdot \arccos((F_m(0) - B)/A), \quad (8)$$

where $\text{sgn}()$ is the sign function.

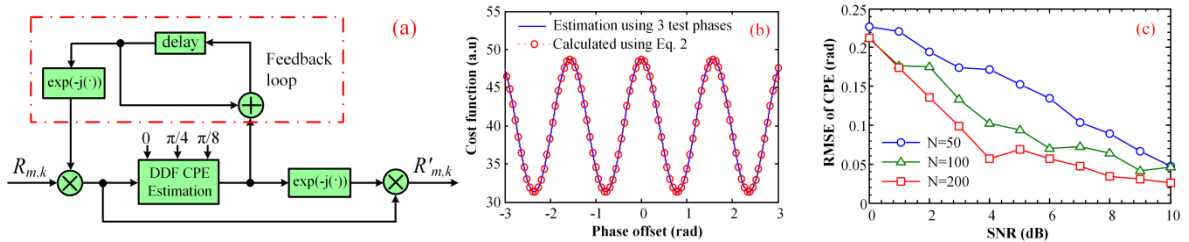


Figure 2.42 (a) Schematic diagram of DDF blind PNC technique for CO-OFDM, (b) The cost function of 16QAM at a SNR of 4dB, (c) CPE error as a function of SNR for 16QAM for different values of the number of calculated samples (N)

To increase the phase noise tolerance, we consider here a two-stage PNC scheme, as shown in Figure 2.42(a). In the first stage, the received samples of one symbol are compensated using the estimated CPE of the previous symbol. After that the residual CPE ($\Delta\Phi_m = \Phi_m - \Phi_{m-1}$) is estimated using the proposed DDF blind estimation technique. If a sufficient number of samples (N) are taken into calculation, the impact of random Gaussian noise can be effectively removed, allowing us to achieve an accurate estimation of the CPE. The calculated (using (2)) and estimated (using 3 test phases) cost functions for 16-QAM with a SNR of 4 dB and $N = 200$ are compared in Figure 2.42(b). The root-mean-square error (RMSE) of the CPE calculated by (8) is plotted in Figure 2.42(c) as a function of the SNR for 16QAM, showing that a small RMSE of 0.1 rad can be achieved for $N = 50$ at SNRs > 7 dB. This result clearly indicates the high tolerance of the proposed CPE estimation method to Gaussian noise.

To verify the effectiveness of the proposed DDF blind PNC scheme, we set up both single channel and WDM CO-OFDM transmissions using both the 16-QAM and QPSK modulation formats, as shown in Figure 2.43.

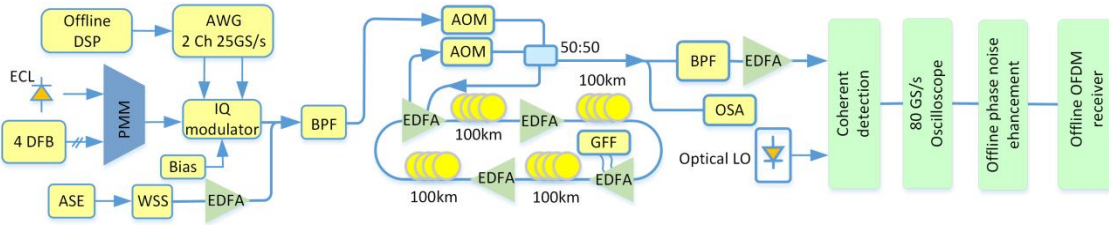


Figure 2.43 Schematic of experimental setup of WDM CO-OFDM transmission with PCPs for fiber nonlinearity compensation. ECL: external cavity laser, PMM: polarization maintaining multiplexer, WSS: Wavelength Selective Switch, DFB: distributed feedback laser, BPF: band-pass filter (optical), AOM: acousto-optic modulator, GFF: gain flatten filter, OSA: optical spectrum analyzer, LO: local oscillator.

The WDM transmission setup comprised a laser grid of five standard DFBs on 100 GHz grid which are substituted in turn by a 100 kHz linewidth ECL. For single channel transmission, only the ECL was used at the transmitter laser. For realizing a more realistic WDM transmission condition, 20 additional loading channels (10 GHz of bandwidth) were generated using an amplified spontaneous emission (ASE) source which is spectrally shaped using a WaveShaper wavelength selective switch (WSS) [38]. A wideband filter was used to filter out-of-band ASE noise at the transmitter. The transmission path is an acousto-optic modulator (AOM) based re-circulating loop consisting of 4×100 km spans of Sterlite OH-LITE (E) fiber, which have insertion loss of 18.9 to 19.5 dB/100 km. The loop switch was located in the mid-stage of the first EDFA and a gain flattening filter (GFF) was placed in the mid stage of the third EDFA. After propagation, the signal was filtered using a 4.2 nm flat topped filter before coherent detection with a 100 kHz linewidth local oscillator (LO). The received electrical signals were then sampled by a real-time oscilloscope at 80 GS/s and processed offline.

The OFDM signals (400 symbols each of 20.48 ns length, 2% cyclic prefix) encoded with QPSK or 16QAM were generated offline in MATLAB using an IFFT size of 512, where 210 subcarriers were filled with data and the remainder with zeros, thus giving line rates of 20 Gb/s (18.2 Gb/s net data rate, after 7% FEC overhead removal) and 40 Gb/s (36.4 Gb/s net data rate), for QPSK and 16QAM respectively. For investigating the impact of laser linewidth, the effective laser linewidth was artificially enhanced by passing the received samples ($r(t)$) through a digital filter defined as: $w(t) = r(t)\exp(\vartheta(t))$, where $\vartheta(t)$ was the phase noise enhancement and followed a Wiener-Levy process with a variance $\sigma^2 = 2\pi\nu \cdot \delta t$ where ν is the enhanced combined laser linewidth and δt is the sampling time. The offline OFDM receiver included: resampling to 25GS/s, timing synchronization, frequency offset compensation, IQ imbalance compensation, CD compensation using an overlapped frequency domain equalizer with the overlap-and-save method, channel estimation with the assistance of an initial training sequence (2 training symbols

every 100 symbols) and phase noise estimation and error counting. The BER was obtained by processing 10 recorded traces ($\sim 10^6$ bits).

The proposed DDF blind PNC scheme is compared with two-stage blind DD, BPS and PA methods for single channel 16QAM transmission in Figure 2.44(a) for a combined laser linewidth of 200 kHz. The proposed method is only matched in performance by highly complex BPS with 16 test phases. Due to error propagation, DD was unable to recover the symbol phases in the system under test, indicating that blind DD is not suitable for high order modulation formats such as 16QAM, even in systems with a typical combined laser linewidth of 200 kHz. A similar comparison result is observed in Figure 2.44(b), which shows the BER as a function of the launch power for the center channel in the WDM QPSK CO-OFDM transmission after 2400 km. The obtained result clearly indicates that the DDF blind PNC is also effective in compensating the CPE due to cross-phase modulation in WDM transmissions. In comparison with PA methods, DDF blind PNC offers better performance while avoiding the SE reduction, due to the pilot subcarriers, which is about 7.6% in this case. This result highlights the great benefit of the proposed PNC technique. The phase noise tolerances of the considered PNC methods are compared in Figure 2.44(c). Without differential coding, all blind PNC methods suffer from a phase ambiguity problem if the residual unwrapped phase lies outside the range $(-\pi/4, \pi/4)$, and thus, are reliable only within a certain phase noise range. Figure 2.44(c) shows that the proposed DDF blind PNC technique can be applied effectively (without differential coding) with a combined laser linewidth up to 700 kHz.

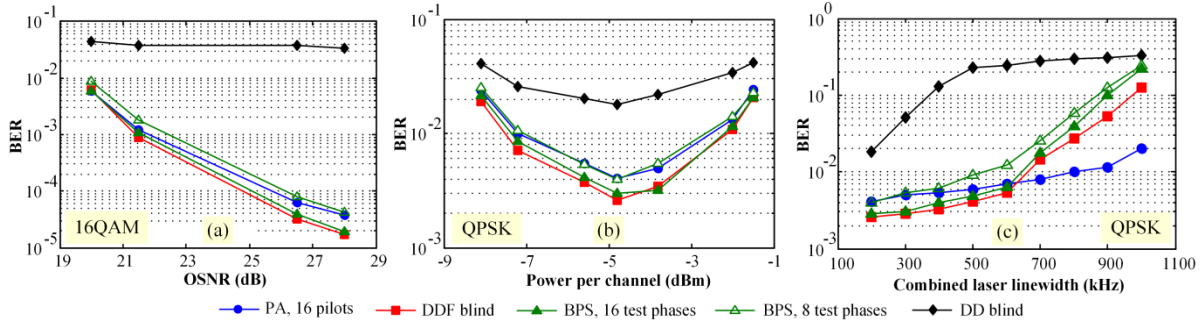


Figure 2.44 Experimental results for (a) BER versus OSNR in the back-to-back case, single channel with 16QAM, the combined laser linewidth is 200 kHz; (b) BER versus the power for the center channel in QPSK WDM transmission, the distance is 2400km, the combined laser linewidth is 200 kHz; (c) BER versus the combined laser linewidth for the center channel in QPSK WDM transmission, the distance is 2400 km, the power is -4.8 dBm.

2.2.3.2 Discussion

We have proposed and experimentally demonstrated a novel DDF blind PNC method for CO-OFDM transmission. Using just three test phases, the proposed technique offers the same performance in comparison with BPS with 16 test phases while avoiding the use of a DD algorithm.

2.2.4 Quasi-Pilot Aided Phase Noise Estimation for CO-OFDM Systems

Existing CO-OFDM phase noise compensation (PNC) may be divided into three groups, data aided (DA) [39, 40], pilot subcarrier aided (PA) [41], and RF-pilot [41]. RF-pilot phase noise estimation is realized by inserting a RF-pilot tone in the middle of the OFDM band that can be used at the receiver to revert any phase noise related impairments. The typical power overhead of RF-pilot PNC is in the range of 7% to 10% due to the tradeoff between pilot and signal to noise ratios. In addition, RF-pilot phase noise estimation also requires overhead due to the frequency guard band surrounding the RF-pilot tone [41]. An overhead is also unavoidable in PA method, in which the CPE is estimated with the assistance of pilot subcarriers (PSs). On the other hand, DA is a blind PNC scheme that enables CPE estimation without any overhead by applying Mth-power-law to remove the data modulation or using a two-stage iterative algorithm with decision-directed technique as shown in [40]. Maximum-likelihood (ML) PNC can also be applied with or without any overhead [42]. Even though ML exhibits better performance and tolerance towards laser

phase noise in comparison to DA but it requires highly exhausting computational load. Performances of these PNC techniques can be further improved by applying decision feedback (DF) (iterative algorithm), which re-estimates and re-compensates for the CPE after initial decision [43].

Among these aforementioned methods PA PNC is the most widely used method due to its inherently low complexity and high precision. However, the ultimate shortcoming of PA PNC is the required additional overhead. In this work we propose a novel PNC scheme termed quasi-pilot aided (QPA) phase noise compensation. The QPA method retains the use of PSs at known frequencies to estimate the carrier phase; however, unlike the conventional PA scheme where pilot phases are predetermined, the pilot phases in QPA are data dependent. The major advantage of QPA estimation is that the number of PSs required for a similar performance to PA estimation can be reduced by a factor of 2, without significant additional complexity and differential encoding. It should be noticed that QPA is also a CPE-based scheme and thus, it is intended for application to non ICI-dominated channels. The effectiveness of the proposed method is demonstrated by comparing with common PNC methods, including PA, DA with M-th power law, RF-pilot and ML estimation for both back-to-back transmission regime and a 2000 km optical link with standard single mode fiber (SSMF).

2.2.4.1 Theoretical principle

By assuming a perfect FFT window synchronization and frequency offset compensation, the received OFDM signal $R_{m,k}$ can be expressed as:

$$R_{m,k} = S_{m,k} h_k \exp(j\Phi_m) + \varepsilon_{m,k} + n_{m,k} \quad (1)$$

where $S_{m,k}$ is the modulated data of the k^{th} subcarrier in the m^{th} symbol before transmission, h_k is the transmission channel response (including not only the optical channel, but also the transceiver front ends) for the k^{th} subcarrier, Φ_m is the CPE for the m^{th} symbol due to laser phase noise or phase shifts acquired during optical fiber transmission. $\varepsilon_{m,k}$ represents residual ICI and is generally treated as white Gaussian noise provided that a large number of OFDM subcarriers are used and the random Gaussian noise is represented by $n_{m,k}$.

In CO-OFDM system, the transmission channel response can be estimated by periodically transmitting training symbols for channel estimation, after which the phase drift is “reset” to 0. By transmitting a few PSs, the CPE can be estimated in PA method as [41, 44]:

$$\bar{\Phi}_m = \arg \left(\frac{1}{N_p} \sum_{\text{pilots}} \frac{R_{m,k} \cdot S_{m,k}^*}{|R_{m,k}| \cdot |S_{m,k}|} \right) \quad (2)$$

where $\arg(\cdot)$ is the phase angle of the information symbol, $S_{m,k}$ is the known transmitted information symbol and N_p is the number of PSs.

It can be seen clearly in (2) that the accuracy of PA phase estimation technique is improved by increasing the number of PSs at the cost of proportionally increasing the overhead and so reducing the net data rate. To address this issue we propose that the effectiveness of PA phase estimation may be enhanced by modulating each pilot subcarrier with a data signal directly related to the signal on a data carrying subcarrier, rather than setting each pilot to a fixed predetermined state. As the pilots are no longer constant, we term this scheme quasi-pilot aided estimation. We consider two specific examples of QPA based estimation. In the first QPA scheme (QPA-1), all N_p pilot subcarriers are distributed equally in the first part of the OFDM band, taking the DC subcarrier as the symmetrical reference ($k=0$). N_p pilot subcarriers ($S_{m,k}$, $k=k_1, k_2, \dots, k_{N_p}$) are chosen by the condition:

$$S_{m,k} = S_{m,-k}^* \quad (3)$$

where $*$ stands for the complex conjugate operation. That is, each pilot subcarrier is the complex conjugate of the data carrying subcarrier equally spaced from the central reference. This proposal can be regarded as a novel method for realizing a transmission scheme with semi-pilot (strongly encoded) symbols [45, 46]. Note that in general the positions of PSs and the correlated data carrying subcarriers can be chosen arbitrarily. Equation (3) provides an option of setting the pilots in QPA-1 scheme such that

PSs and the correlated data carrying subcarriers are distributed equally among the OFDM band for achieving the best performance.

At the receiver, after performing channel estimation, each pilot subcarrier is coherently combined with its data carrying counterpart, eliminating the data modulation and enhancing the signal to noise ratio (SNR). The overall CPE is then estimated by summing the resultant modulation free vectors and taking the argument, as shown in the following expression:

$$\bar{\Phi}_m = \arg\left(\sum_{pilot} R_{m,k} \cdot R_{m,-k}\right) / 2, \quad (4)$$

This simple approach allows the CPE to be estimated without any prior information on the phases of PSs. In addition to this, the CPE is calculated by taking into account $2N_p$ subcarriers, which includes the complex conjugate data pilots in the first half and the actual data on the second half of the OFDM band. Thus, the accuracy of this estimation is similar to the PA phase estimation scheme whilst averaging the noise $n_{m,k}$ over $2N_p$ pilot subcarriers. In order to show the SNR advantage of QPA-1 scheme, let us consider the case when only one pilot is used for simplicity, and the extension to many pilots is straightforward. By assuming that $S_{m,k}h_k = S_{m,-k}h_{-k} = 1$ and there is no ICI, from (1) we have:

$$R_{m,k} \cdot R_{m,-k} = \exp(2j\Phi_m) + n'_{m,k} + n'_{m,-k} + n_{m,k} \cdot n_{m,k}$$

At intermediate-to-high SNR the product of the two noise terms can be neglected, leading to:

$$R_{m,k} \cdot R_{m,-k} = \exp(2j\Phi_m) + n'_{m,k} + n'_{m,-k} = \rho \exp(j(2\Phi_m + 2\theta))$$

where ρ is the modulus, 2θ is the part of the complex noise that can be approximated to white Gaussian noise with power $NSR = SNR^{-1}$. By applying QPA-1 we get:

$$\bar{\Phi}_m = \Phi_m + \theta, \text{ for } -\pi/2 < \Phi_m + \theta < \pi/2$$

It is clear that the power of θ is $NSR/4$, while the power of the noise component tangential to complex exponential in the conventional method (equation (2)) is $NSR/2$. As a result, QPA-1 scheme gives 3dB SNR gain over the conventional PA method.

In the second QPA scheme (QPA-2) instead of coding the pilots as direct conjugates of a single data subcarrier, the phases of N_p PSs are chosen such that their mean phase angle is opposite that of all the remaining data subcarriers, as specified by the condition:

$$\langle \arg(S_{m,k}) \rangle_{pilots} + \langle \arg(S_{m,l}) \rangle_{data} = 0, \quad (5)$$

where $\langle \cdot \rangle$ stands for the averaging operation. So the phases of the pilot subcarriers can be chosen equal to meet the requirement of (5):

$$\arg(S_{m,k})_{pilot} = -\langle \arg(S_{m,l}) \rangle_{data}$$

At the receiver, the CPE is estimated by summing the phases of all pilots and associated data subcarriers as follow:

$$\bar{\Phi}_m = \left(\langle \arg(R_{m,k}) \rangle_{pilots} + \langle \arg(R_{m,l}) \rangle_{data} \right) / 2 \quad (6)$$

Expression (6) also indicates that in QPA-2 the CPE is calculated without any prior knowledge of the phases of PSs. It is obvious that the accuracy of CPE estimation is improved significantly by taking all the subcarriers into consideration. The positions of PSs in QPA-2 scheme can be also chosen arbitrarily. However, for achieving the best performance, in QPA-2 scheme PSs should be equally distributed among the OFDM band. As the total phase of all symbols is constant, QPA-2 may be considered as a form of "phase parity". Note that in QPA schemes PSs are not inserted into training symbols, thus there is no impact during the synchronization process.

The phase noise tolerance of PNC methods can be increased by using the information about the CPE of the previous symbol(s) with an iterative algorithm [40, 43]. This approach is also applied here to QPA PNC.

In the first stage of compensation; the laser phase noise of the current symbol is compensated using the estimated CPE of the previous symbol. After that the difference between CPE estimations of the current and the previous symbols ($\Delta\Phi_m = \Phi_m - \Phi_{m-1}$) is estimated using expression (4) or (6). This scheme is known as two-stage-iterative (TSI) QPA PNC and can be regarded as an iterative algorithm, which increases the laser phase noise tolerance (in term of cycle slip and click probability) of QPA schemes significantly. The cycle slip probability (probability that the unwrapped phase lies outside the range $(-\pi/2, \pi/2]$) can be estimated as:

$$P \leq 2 \cdot Q(\pi^2 / 4\sigma^2), \quad (7)$$

where Q is the Q-function, $\sigma^2 = 4\pi\nu T_u$, ν is the combined laser linewidth, T_u is the OFDM symbol duration.

2.2.4.2 Simulation Setup - Results

In this section, we numerically investigate the effectiveness of TSI QPA-1 and TSI QPA-2 PNC methods in a 40Gb/s single polarization CO-OFDM system. The simulation framework is carried out in MATLAB and the setup is shown in the Figure 2.45.

As depicted in Figure 2.45, 40 Gb/s data stream is first mapped on 1000 subcarriers (1st to 1000th) using QPSK modulation format with Gray coding and subsequently transferred to the time domain by an IFFT of size 2048. A 12.5% cyclic prefix is appended to OFDM symbol to accommodate chromatic dispersion. The total OFDM symbol duration is 50ns. The fiber link is assumed to consist of 25 × 80-km spans of SSMF with the loss coefficient of 0.2 dB/km, PMD coefficient of 0.1ps/km^{0.5}, the nonlinearity coefficient of 1.22W⁻¹km⁻¹ and dispersion of 16 ps/nm/km. The fiber span loss is compensated by utilizing erbium-doped fiber amplifier (EDFA) with 16dB of gain and a noise figure of 6dB. The laser phase noise is modeled as a Wiener-Levy process with a variance $\sigma^2 = 2\pi\nu t$ where t is the time difference between two samples [41]. In simulation ASE noise is added inline after each fiber span. The simulated time window contains of 1000 OFDM symbols. The channel estimation and equalization is performed using zero forcing estimation method with the aid of training sequence (1 symbol), which is inserted after every 25 OFDM symbols.

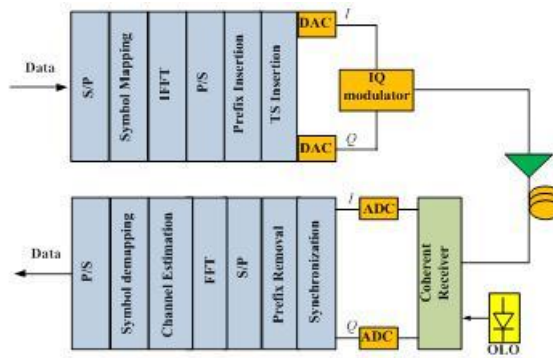


Figure 2.45 Block diagrama of 40 Gb/s CO-OFDM transmissions. S/P: serial/parallel conversion, P/S: parallel/serial conversion, TS: training symbol, DAC: digital-to-analog converter, OLO: optical local oscillator

Figure 2.46 illustrates the BER sensitivity in the back-to-back transmission regime with different PNC techniques at the combined laser linewidth of 100 kHz. One can notice that ML performs slightly better than PA, which agrees with previous reports [42]. However, with 2 PSs both TSI QPA methods outperform PA and ML methods. With 4 PSs, PA and ML show approximately the same performance as the TSI QPA schemes using 2 PSs confirming that the overhead can be effectively reduced by a factor of 2. Closer inspection reveals that TSI QPA-1 slightly outperforms TSI QPA-2 owing to the slightly improved noise mitigation when using conjugated PSs. In the case of DA PNC applying the Mth-power law, no PSs are required but the performance suffers strongly by the phase ambiguity associated with the Mth-power-law, indicating that the technique is unsuitable for practical implementation.

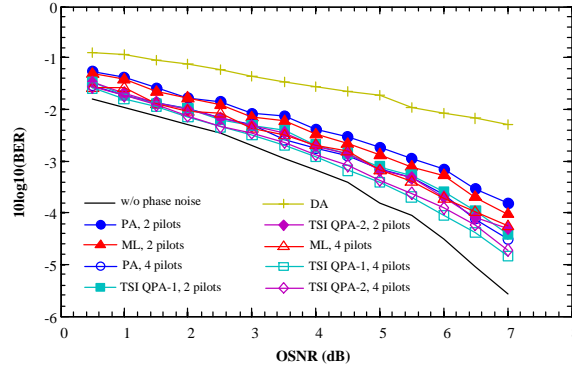


Figure 2.46 Back to back BER sensitivity for DA (crosses), PA (circles), ML (triangles) TSI QPA-1 (squares) and TSI QPA-2 (diamonds) estimation methods when 2 (closed) or 4 (open) subcarriers do not carry independent information (pilots)

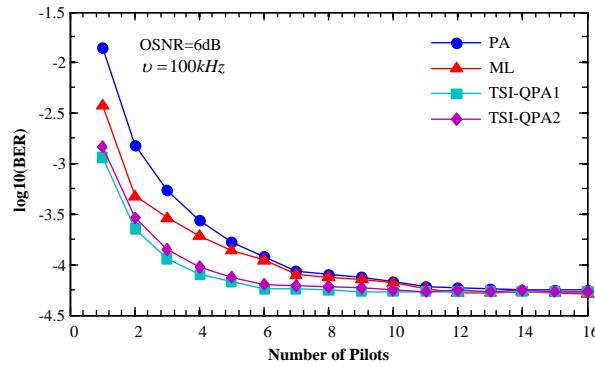


Figure 2.47 BER as a function of the number of pilot subcarriers with different phase noise estimation methods, PA (circle), ML (triangle) TSI QPA-1 (square) and TSI QPA-2 (diamond)

The overhead benefits of TSI QPA are more clearly illustrated in Figure 2.47 for a combined laser linewidth of 100 kHz, and a fixed OSNR of 6dB. It can be seen that with the conventional PA method, 8 PSs are required for negligible penalty (less than 5% degradation in BER). Similar overhead requirement can be observed for ML assisted PNC method. On the other hand, when TSI QPA-1 and TSI QPA-2 methods are applied the required number of PSs is 4, verifying that by applying QPA PNC methods, the required number of PSs can be reduced effectively by a factor of 2.

Figure 2.48 presents the tolerance of the PNC methods studied here towards laser phase noise. Among these PNC methods, ML is the most tolerant technique to laser phase noise. For combined laser linewidth $\leq 600\text{kHz}$, TSI QPA-1 and TSI QPA-2 methods with 2PSs require almost the same OSNR in comparison to PA technique with 4 PSs. For the investigated system, the cycle slip probability at $\nu = 600\text{kHz}$ is $P \leq 2Q(\pi^2/16\pi\nu T_u) \approx 10^{-38}$, which is less than the value required to avoid differential coding (10^{-18}) [47]. In addition, taking into account the fact that commercial external-cavity lasers have a linewidth of around 100 kHz, the advantage and reliability of TSI QPA PNC methods with reduced overhead have very high credibility.

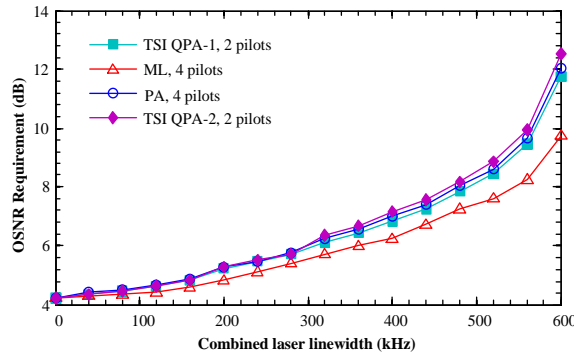


Figure 2.48 OSNR requirement (for a BER level of 10^{-3}) as a function of the combined laser linewidth (ν) for different phase noise estimation

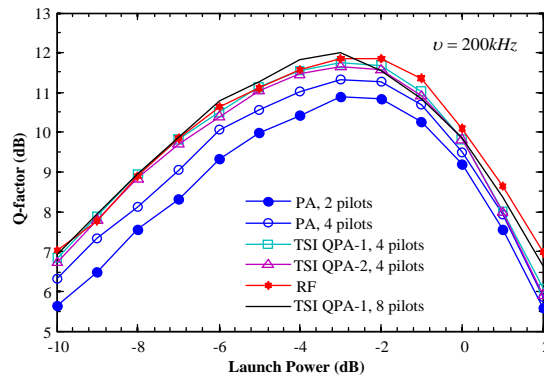


Figure 2.49 Q-factor as a function of the launch power when different phase noise estimation methods are applied, after 2000km of transmission

Performances of different phase noise estimation methods at 2000km long-haul optical transmission link are compared in the Figure 2.49. In this experiment the linewidth of the transmitter laser and the local oscillator are assumed to be 100 kHz. The system's Q-factor is delivered by the BER obtained through direct error counting [48]. In this figure we also show the performance of RF-pilot enabled PNC method. In order to apply this method, a RF-pilot tone (with 6.3% of power overhead) is inserted into the middle of the OFDM band. A frequency guard band of 100MHz is added surrounding the RF-pilot tone, resulting in around 0.4% of frequency overhead. At the receiver, a low pass filter (LPF) with a bandwidth of 10 MHz is applied to filter out the RF-pilot tone and subsequently applied for phase noise estimation and compensation. Due to the LPF, the complexity of RF-pilot PNC method is significantly higher in comparison to PA and QPA methods.

At the optimum optical launch power, TSI QPA-1 and TSI QPA-2 methods with 4 PSs, and PA with 8 PSs exhibit almost the same performance as RF-pilot tone PNC. Even though theoretically RF-pilot tone PNC can compensate for both CPE and ICI [41] but the effectiveness of RF-pilot tone method reduces under ASE and fiber nonlinearity impairments. In addition, the RF-pilot tone method is strongly affected by the size of the frequency guard band surrounding the DC subcarrier; consequently with a small overhead (0.4% in this paper) RF-pilot tone PNC does not show advantage in comparison to QPA PNC methods. In particular, 4 pilot TSI QPA also requires a 0.4% overhead, which is almost equivalent to that of the RF-pilot tone. As a result, TSI QPA methods are also more effective than RF-pilot tone in term of the balance among performance, overhead and the complexity.

2.2.4.3 Experimental implementation

The experimental set up is illustrated in Figure 2.50. The transmitter consisted of a 1553.47 nm fiber laser (100Hz linewidth); an IQ modulator biased at null point and 90° phase offset; a 2 channel 25GS/s arbitrary waveform generator (AWG) programmed with the OFDM signal. The OFDM signal (400 symbols each of 20.48 ns length, 2% cyclic prefix) encoded with 16QAM modulation format was generated offline in MATLAB using an IFFT size of 512, where 210 subcarriers were filled with data and the remainder zeros giving a line rate of 40Gb/s (36.4Gb/s after cyclic prefix and FEC overhead removed). The output of the IQ modulator was amplified by an erbium doped fiber amplifier (EDFA) and subsequently coupled into a transmission span of 20 km of single mode fiber (SMF). A short span was used to allow focus on the laser phase noise rather than other transmission impairments. After propagating through SMF, another EDFA was used for noise loading, where a 1% tap was taken for OSNR measurement. The rest of the signal was detected using a polarization diverse coherent receiver. The electrical received signals were then sampled by a real-time oscilloscope at 80 GS/s and 25 GHz bandwidth.

As the fiber lasers used in the experiment had a small linewidth, for investigation the impact of laser phase noise the effective linewidth was artificially enhanced by passing the received samples ($r(t)$) through a digital filter defined as: $s(t)=r(t) \cdot \exp(\vartheta(t))$, where $\vartheta(t)$ was the phase noise enhancement and followed a Wiener-Levy process with a variance $\sigma^2=2\pi \cdot \nu \cdot dt$ where ν is the enhanced combined laser linewidth and dt is the sampling time. The offline OFDM receiver included; resampling to 25GS/s, timing synchronization, frequency offset compensation, IQ imbalance compensation, channel estimation, phase noise estimation and error counting.

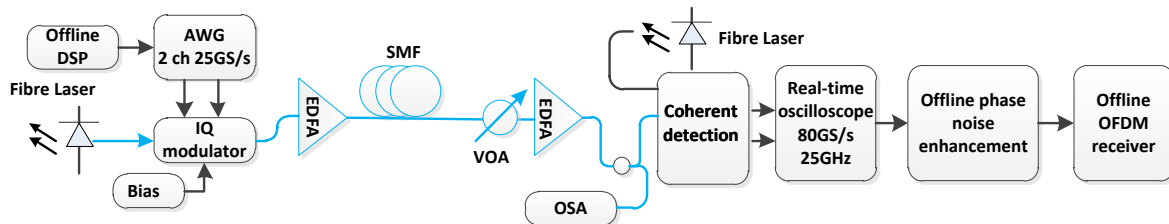


Figure 2.50 Experimental Set-up (AWG: Arbitrary Waveform Generator; EDFA: Erbium Doped Fiber Amplifier; VOA: Variable Optical Attenuator; OSA: Optical Spectrum Analyzer)

The two QPA PNC schemes are compared with RF and PA methods as a function of the OSNR, as shown in Figure 2.51(a) for a combined laser linewidth of 200 kHz. The RF-pilot tone was added by detuning the IQ modulator to give a DC subcarrier (7% power) separated from the 210 data subcarriers by a frequency guard band of 100 MHz. At the receiver, the DC subcarrier was filtered out for PNC using a low pass filter with an optimized bandwidth of 20 MHz. It can be seen in Figure 2.51(a) that both QPA schemes outperform the PA PNC scheme and in particular 2 pilot QPA schemes offer similar performance to 4 pilot PA schemes confirming that the overhead can be effectively reduced by a factor of 2. Similarly, 2 pilot QPA outperforms the use of an RF-pilot tone. The RF-pilot tone method is strongly affected by the size of the frequency guard band surrounding the DC subcarrier; consequently with a small overhead (1% in this paper) the QPA method outperforms the RF method. In particular, 2 pilot QPA requires a .95% overhead, which is almost equivalent to that of the RF-pilot tone.

The impact of overhead on CPE estimation performance is illustrated in Figure 2.51(b), showing BER at an experimentally measured OSNR of ~26 dB. It can be seen that with the conventional PA method, 10 PSs are required for negligible penalty (less than 5% degradation in BER). On the other hand, for both QPA schemes the required number of PSs is less than 6, a reduction of almost a factor of 2.

Figure 2.51(c) confirms that this advantage is maintained over a range of laser phase noises, with both 2 pilot QPA methods showing similar or enhanced performance compared to the PA method with 4 pilots for combined laser linewidths (artificially broadened) up to 800 kHz.

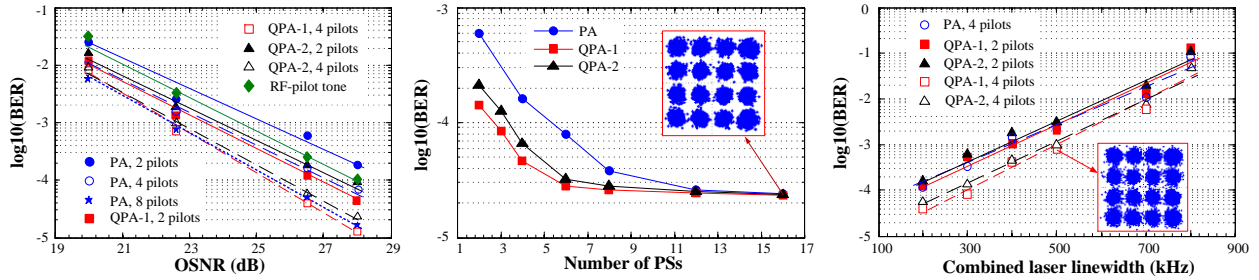


Figure 2.51 Experimental results for (a) BER versus OSNR with 200kHz combined linewidth, (b) BER versus number of PSs at 26dB OSNR and (c) BER versus combined laser linewidth also at 26dB OSNR for; Green – RF pilot tone assisted estimation (RF) with 100 MHz guard band, Blue – conventional pilot aided (PA) estimation, Red - quasi pilot aided estimation using conjugate pilots (QPA-1), Black - quasi pilot aided estimation using phase parity (QPA-2) where (except in Fig. 2(b),) closed symbols represent 2 pilots, and open symbols 4

2.2.4.4 Discussion

We have proposed a novel common phase error estimation technique based on correlating the phase of pilot tones with data subcarriers. Numerical simulation results have confirmed that by setting PSs in correlation with data subcarriers the overhead of pilot aided carrier phase estimation may be reduced by a factor of 2 for two different correlation techniques, conjugated pilots and phase parity pilots. In addition, in comparison with RF-pilot tone, the proposed methods can offer a similar performance at the same overhead while significantly reducing the complexity in implementation. Finally, experimental results have confirmed that by setting PSs in correlation with data subcarriers the overhead of pilot aided carrier phase estimation may be reduced by a factor of 2 for two different correlation techniques, conjugated pilots and phase parity pilots

2.2.5 Phase-Conjugated Pilots for Fiber Nonlinearity Compensation

There have been extensive efforts in attempting to surpass the Kerr nonlinearity limit through several nonlinearity compensation techniques. Digital-back-propagation (DBP) is an effective nonlinearity compensation method, which removes the nonlinear distortion by inverting the distorted signal at the receiver digitally [49]. However, accurate DBP requires a substantial increase in digital signal processing (DSP) complexity, proportional to the number of spans. Furthermore, in wavelength-division multiplexed (WDM) systems the effectiveness of DBP is significantly reduced as the neighboring WDM channels are unknown to the compensator.

Digital [50] and optical [51-53] phase conjugations (OPCs) at the mid link or installed at the transmitter [54] are other well-known nonlinear compensation techniques that conjugate the signal phase after transmission in one segment of the link in order to achieve a net cancellation of the nonlinear phase shift using the nonlinearity generated in the second segment of the link. However, OPC modifies the transmission link by inserting a phase conjugator at the middle point of the link, and imposes significant symmetry conditions with respect to the phase conjugator, and thus, significantly reducing the flexibility in an optically routed network.

Recently, novel nonlinear compensation technique called phase-conjugated twin waves (PC-TW) has been proposed in [55]. PC-TW is a transponder-based technique that can be implemented with minimal additional optical hardware or DSP. In this scheme, the signal complex waveform and its phase-conjugate copy are simultaneously transmitted in x- and y-polarization states. If the dispersion map of the link is symmetrical, the nonlinear distortions on x-and y-polarizations are essentially anti-correlated, and thus, it can be subsequently mitigated at the receiver through coherent superposition of the two copies. The PC-TW provides a simple and effective solution in compensating optical fiber nonlinearity as it requires only an additional per symbol conjugate-and-add operation prior to symbol detection. However, the one serious shortcoming of PC-TW is that it sacrifices half the transmission capacity. To address this drawback of PCTW, a dual PCTW scheme has been also proposed for single carrier systems, yielding an improvement

of ~ 1.2 dB [56]. Unfortunately, quadrature pulse shaping is required for dual PCTW, which cannot be applied effectively for multicarrier modulation formats such as orthogonal frequency division multiplexing (OFDM). To address this problem, a phase-conjugated coding scheme has been proposed in [57], offering around 1.5 dB performance gain in BPSK CO-OFDM transmission.

The general idea of communication through phase-conjugated optical variants is described in [58], claiming that a meaningful performance gain can be achieved through coherent superposition of the signal and its phase conjugated copy, which can be transmitted in a different polarization state, time slot, spatial localization, optical carrier wavelength and subcarrier frequency. In [59], coherent superposition of the useful signal and its phase conjugated copy transmitted in a different optical wavelength was adopted to increase significantly the transmission distance. In addition, in [60] it was also applied to OFDM subcarrier pairs with Hermitian symmetry. However, in a similar manner to the PCTW scheme, both approaches proposed in [59, 60] also sacrifice half the transmission capacity.

In this section, we demonstrate a novel nonlinearity compensation technique for CO-OFDM systems based on the transmission of phase-conjugated pilots (PCPs), without sacrificing 50% of the transmission capacity. The general idea was first presented in [61]. In this scheme, a portion of the OFDM subcarriers (up to 50%) are transmitted as phase-conjugates of other subcarriers. The PCPs are used at the receiver to estimate the nonlinear distortion of their respective original subcarriers. The estimated distortion can also be used to compensate the nonlinear impairments in other subcarriers close to the PCP, thanks to the narrow OFDM subcarrier spacing (tens of MHz), which enhances the correlation between nonlinear phase shifts of neighboring subcarriers. With this technique, the fiber nonlinearity impairments due to the Kerr effect in OFDM systems can be effectively compensated without the complexity of DBP or 50% loss in capacity of PC-TW. The technique proposed here can be effectively implemented in both single polarization and PMD systems, in both single channel and WDM systems. In other words, nonlinearity compensation using PCPs offers a simple, easy implementation applicable to any optical links where the level of nonlinear compensation may be readily tuned by selecting an appropriate number of PCPs.

2.2.5.1 Phase conjugated pilots for fiber nonlinearity compensation

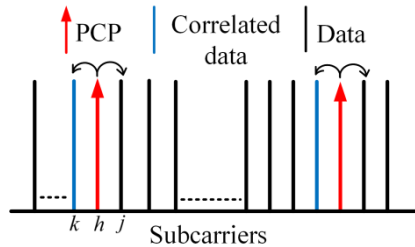


Figure 2.52 Inserting phase-conjugated pilots for fiber nonlinearity compensation

Since the frequency spacing in an OFDM system is often small [62, 63] (tens of MHz) compared to the phase matching bandwidth of the link (few GHz [64][30]), at the end of the optical link, the nonlinear phase shifts on adjacent subcarriers will be strongly correlated. This implies that nonlinear distortion experienced in one spectral region may be used to estimate the distortion in other closely space regions, as observed in pilot tone compensation schemes [65]. Thus nonlinear compensation can be achieved by sparsely inserting PCPs across the OFDM band.

The concept of inserting PCP is illustrated in the Figure 2.52. Suppose the information symbol carried by the k^{th} subcarrier is $S_k = A_k \cdot \exp(j \cdot \varphi_k)$ where A_k and φ_k are the amplitude and the phase of this information symbol, then the phase conjugated symbol can be transmitted in the h^{th} subcarrier, $S_h = S_k^* = A_k \cdot \exp(-j \cdot \varphi_k)$, where $(.)^*$ represents complex conjugation. To simplify the exposition, we assume that during propagation nonlinear phase shifts, represented by θ_k and θ_h , are added to these subcarriers. The received information symbols on the k^{th} and h^{th} subcarriers are $R_k = A_{r,k} \cdot \exp(j \cdot \varphi_k + j \cdot \theta_k)$ and $R_h = A_{r,h} \cdot \exp(-j \cdot \varphi_k + j \cdot \theta_h)$, respectively. If the frequency spacing between k^{th} and h^{th} subcarriers is small enough, the nonlinear phase shifts will be highly correlated, $\theta_k \approx \theta_h$ providing the opportunity of cancelling the nonlinear phase shift on the k^{th}

subcarrier by averaging the received information symbol of a subcarrier and the subcarrier which carries its phase conjugate (after a second conjugation):

$$\bar{R}_k = (R_k + R_h^*) / 2 \approx A_{r,k} \cdot \cos(\theta_k) \cdot \exp(j\phi_k) \quad (1)$$

This compensation technique is often referred in the literature as coherent superposition [55, 66]. Note that the nonlinear phase shift on the original subcarrier k can be estimated as [67, 68]:

$$\theta_k = \arg(R_k \cdot R_h) / 2 \quad (2)$$

Ideally, a data carrying subcarrier and its PCP should be closely spaced in frequency (adjacent) to maximize the level of correlation of the nonlinear phase shifts between these subcarriers. For those data carrying subcarriers which do not have PCPs, the nonlinear phase shift of the j^{th} subcarrier can be estimated and compensated as:

$$\theta_j = \arg\left(\sum_{k,h} \eta_{jkh} \cdot R_k \cdot R_h\right) / 2$$

$$\bar{R}_j = R_j \cdot e^{-j\theta_j} \quad (3)$$

where η_{jkh} is the FWM efficiency coefficient. In this paper η_{jkh} is approximated either as 1 if j is the closest subcarrier to k or h and 0 otherwise.

By applying this fiber compensation technique, the fiber nonlinearity phase shifts on data subcarriers in an OFDM system can be compensated without conjugating all pairs of subcarriers. In this system configuration, several data carrying subcarriers are placed between conjugate pairs. The nonlinear phase shifts for all of these subcarriers are similar as long as the frequency spacing is small. These nonlinear distortions can be compensated using the estimated nonlinear distortion on the closest pair of subcarrier data and phase conjugated pilot. As a result, one phase conjugated pilot can be used to compensate the nonlinear distortions on several subcarriers and the overhead due to phase conjugated pilots is relaxed and can be designed according to the requirement of a specific application.

Whilst the most accurate nonlinear compensation will be achieved by weighting and summing the nonlinear distortion estimated from all of the phase conjugate pairs, the nonlinear distortion on subcarriers which are not part of phase conjugate pairs can be estimated in various ways. The first approximation is to simply use the estimated nonlinear distortion from the nearest phase conjugate pair. The second approximation is to use a linear interpolation of the estimated nonlinear distortions from the two closest phase conjugate pairs (two points).

In common with PC-TW, the performance of a system based on PCP can be further improved with 50% electrical dispersion pre-compensation (pre-EDC), which is applied to create a dispersion-symmetry along the transmission link. This dispersion map enhances the similarity between nonlinear distortions on subcarrier data and its phase conjugate, thus further improving the effectiveness of the proposed nonlinearity compensation scheme.

2.2.5.2 Simulation

As a proof of concept, we conducted simulation of the proposed PCP scheme for a single channel 112 Gb/s PDM QPSK CO-OFDM transmission. The simulation setup is shown in the Figure 2.53. The data stream was first divided into x- and y-polarizations, each of which was then mapped onto 1400 subcarriers using QPSK modulation format and subsequently transferred to the time domain by an IFFT of size 2048 while zeros occupying the remainder. Our standard simulation was as follows, although some parameters were varied to illustrate the salient features of this nonlinearity compensation scheme. The OFDM useful duration was 50ns (20 MHz subcarrier spacing), no cyclic prefix was added and we ignored here the effect of polarization mode dispersion. The fiber link comprised 80-km spans of standard single mode fiber (SSMF) with a loss parameter of 0.2dB/km, nonlinearity coefficient of $1.22W^{-1}km^{-1}$ and dispersion of 16ps/nm/km. The span loss was compensated by Erbium-doped fiber amplifiers (EDFA) with 16dB of gain and 6dB noise

figure. The amplified spontaneous emission (ASE) noise is added inline to ensure that the interaction between signal and noise [69] is correctly captured. The transmitter and receiver lasers had the same linewidth of 100 kHz. The simulated time window contained 100 OFDM symbols (560,000 bits).

The received signal after coherent reception was first resampled and converted from serial to parallel for further processing, including chromatic dispersion compensation using a frequency domain equalizer (OFDE) employing the overlap-and-save method, channel estimation and equalization with the assistance of initial training sequence (2 training symbols every 100 symbols) using zero forcing estimation with MIMO processing [70], and nonlinear phase noise (NLPN) estimation and compensation. In order to compensate for NLPN using PCPs, it is necessary to compensate for the common phase error (CPE) introduced by the lasers' phase noise and common phase shift due to the fiber nonlinearity first. To reduce the net overhead, this compensation is also achieved using all the PCPs as shown in [68], using a two-stage compensation scheme. After CPE compensation, the nonlinear distortion of subcarriers data accompanied by PC pilots was compensated using Eq. 1 whilst the nonlinear distortions of other subcarriers were compensated using Eq. 3.

In order to demonstrate effectiveness of the nonlinear noise cancellation scheme based on the coherent superposition of the PCP pairs, we first turn off the ASE noise. The simulation results are shown in the Figure 2.54 for a 1200 km optical link with 5 dBm of the launch power. After coherent superposition, a dramatic reduction (~ 7 dB) of the nonlinear signal distortion variance (σ^2) was observed, indicating that the nonlinear distortion on a data carrying subcarrier and those of its PC are highly anti-correlated, especially if the frequency spacing is small.

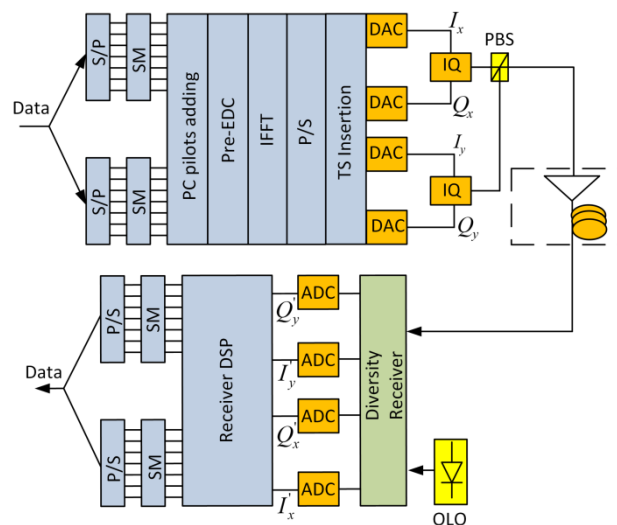


Figure 2.53 Block diagram of 112 Gb/s PDM CO-OFDM transmissions. S/P: serial/parallel conversion, P/S: parallel/serial conversion, SM: symbol mappings, TS: training symbol, DAC: digital-to-analog converter, ADC: analog-to-digital converter, I/Q: I/Q modulator, PBS: polarization beam splitter, OLO: optical local oscillator

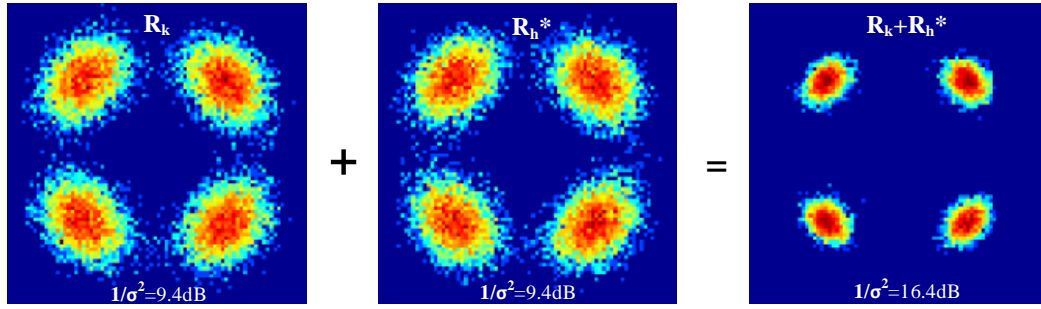


Figure 2.54 Nonlinear noise cancellation based on the coherent superposition of PCP pairs. The transmission distance is 1200km, launch power is 5dBm, ASE noise is not considered and 50% pre-EDC is adopted.

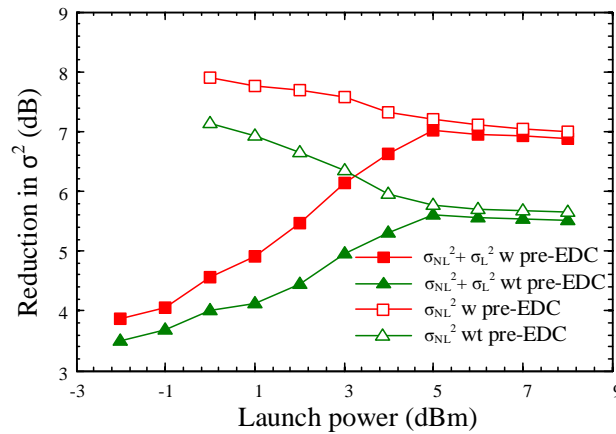


Figure 2.55 Measured reduction of signal variance from both nonlinear distortion (σ_{NL}^2) and linear noise (σ_L^2) as a function of the launch power, in systems with and without 50% pre-EDC. The transmission distance is 1200km, ASE noise is included

Figure 2.55 plots the reduction in the signal variance (σ^2), which is equivalent to the signal-to-noise ratio (SNR) improvement, when coherent superposition is applied for PCP pairs in systems with and without 50% pre-EDC (red and green respectively). The difference between the open and solid symbols illustrates the impact of ASE noise. When the launch power is small, the dominant limiting factor in the system is the ASE noise. As a result, the coherent superposition of the PCP pairs using 50% pilots offers around ~ 3 dB reduction of the signal variance, as expected from the linear effects of coherent superposition of two copies of the same signal. However, with increasing launch powers a larger reduction in σ^2 eventually occurs, indicating the maximum effectiveness of the proposed nonlinear noise cancellation scheme. Note that in this regime, there is little impact from the addition of ASE noise suggesting that the system is limited by compensation accuracy rather than the fundamental parametric noise amplification process [69]. When 50% pre-EDC is performed, the reduction of σ^2 is further enhanced, reaching around 7 dB at a high level of the launch power. When considering only the nonlinear noise distortion, an even higher reduction of ~ 8 dB can be observed.

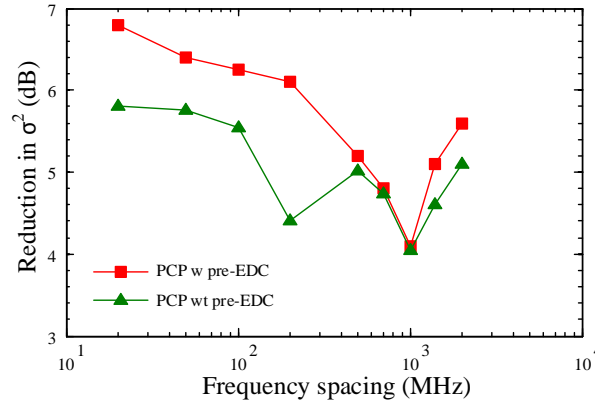


Figure 2.56 Measured reduction of signal variance as a function of the frequency spacing. The transmission distance is 1200 km, the launch power is 5dB, ASE noise is included and the number of subcarriers is varied, keeping the same data rate (112 Gb/s).

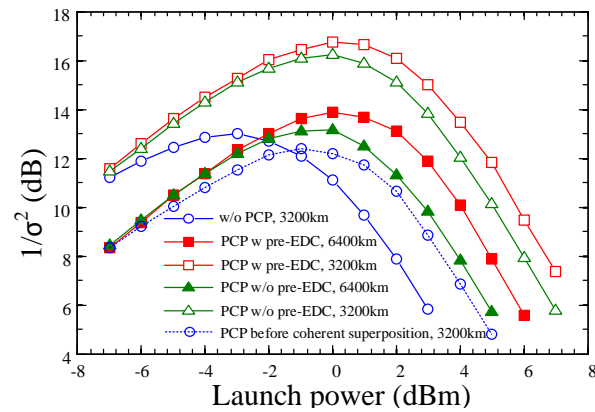


Figure 2.57 Nonlinear cancellation using coherent superposition of PCP pairs in long-haul 56 Gb/s (net data rate) CO-OFDM transmission. The transmission distances are 3200 km (open symbols) and 6400 km (closed symbols)

As mentioned before, the proposed PCP compensation scheme relies on the correlation of nonlinear phase shifts of the data carrying subcarriers and PCPs; the effectiveness of this scheme depends strongly on the subcarrier frequency spacing. Figure 2.56 shows the reduction of signal variance σ^2 as a function of the subcarrier frequency spacing (by varying the number of the subcarriers). As expected, when the subcarrier frequency spacing increases, the benefit of coherent superposition scheme tends to decrease, from around 7dB at a frequency spacing of 20MHz to around 4 dB at a frequency spacing of 1 GHz (for the case of 50% pre-EDC). The 3dB nonlinear interaction bandwidth of the simulated system was around 1.1 GHz. However, we attribute the rapid dip in performance around 1GHz (and 200MHz without pre-dispersion) to a quasi-phase matching process [64, 69, 71] rather than a specific resonance with this bandwidth.

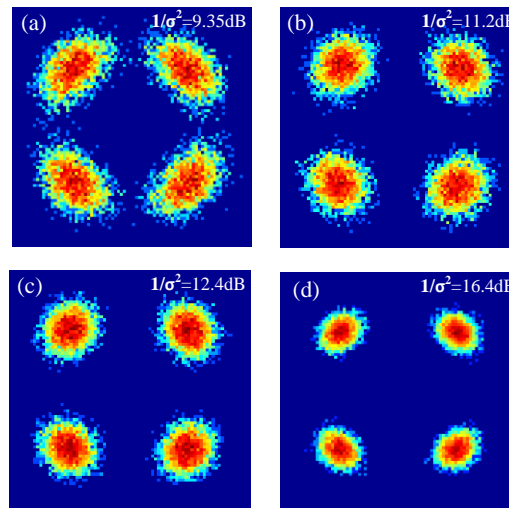


Figure 2.58 Received constellation diagrams in 112 Gb/s PDM CO-OFDM systems without (with the same bandwidth, before CS) (a) and with PCPs for fiber nonlinearity compensation (b - 12.5%, c - 25%, d - 50% overhead). The Transmission distance is 1200 km, the launch power is 5dBm.

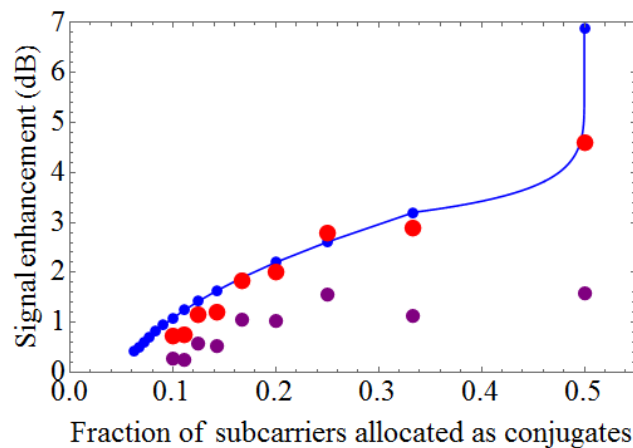


Figure 2.59 Signal enhancement of a 3,200km PDM NGI CO-OFDM system at the optimum launch power as a function of the fraction of subcarriers allocated as phase conjugate pilots, showing measured reduction in signal variance (red symbols), net gain after subtraction of overhead (purple) and predicted signal to noise ratio gain (blue symbols)

The effective SNR of 112 Gbit/s OFDM systems with 50% PCPs and without any PCPs are compared in Figure 2.57. Note that, the spectral efficiency is reduced by a factor of 2 when 50% of the subcarriers are transmitted as PCPs. In Figure 2.57, by combining pre-EDC and PCP techniques, a reduction of around 4.5dB in the signal variance can be achieved at a transmission distance of 3200km at the cost of 50% overhead. The nonlinear threshold is also increased by 9dB with PCP compensation. This result clearly indicates that a substantial fraction of the nonlinear distortion can be mitigated by coherently adding the phase conjugated pilot and its correlated data subcarrier. As a result of this improvement, a longer transmission distance can be achieved. In Figure 2.57 the effective SNR of system with 50% PCP after 6400km of transmission distance is also plotted for comparison purpose. As can be seen, this system still offers around 1.5dB advantage in performance in comparison with OFDM system without PCP after 3200km of transmission distance. This comparison indicates that the product of spectral efficiency and transmission distance can be significantly increased with PCP techniques, and is consistent with results obtained for PC-TW.

This implementation offers excellent performance but it requires 50% overhead. The required overhead can be reduced by using the estimated nonlinear distortion on one pair of subcarrier data and its PCP to compensate the nonlinear distortions on other subcarriers. Specifically, one PCP can be used to compensate the nonlinear distortion of 2, 3, 4 or more data subcarriers at the cost of 33%, 25%, 20% or smaller overhead respectively. In Figure 2.58 the received constellation diagrams of systems with and without PCPs for fiber nonlinearity compensation are shown for different values of PCP overhead with the launch power deliberately set in the highly nonlinear region (+5dBm). The trade-off between overhead due to PCPs and performance can be clearly observed. A better performance comes with the cost of larger overhead due to the transmission of additional PCPs.

The reduction in the signal variance (in dB) at the optimum launch power (difference of the minimum achievable σ^2 in systems without and with PCPs) and the net benefit in dB (after extracting the spectral efficiency reduction due to the PCPs) as a function of the overhead due to PCPs are shown in the Figure 2.59. With 50%, 33%, and 20% overhead the achievable reduction in σ^2 are 4.6 dB, 3.2 dB and 2.1 dB respectively, or approximately 0.1dB per 1% of overhead. We believe that the reduction in σ^2 enhancement as the overhead is reduced is initially due to lower coherent gain (a smaller number of subcarriers have the >3dB benefit of coherent superposition), but eventually the subcarriers become spaced by more than the FWM efficiency bandwidth after which the nonlinear compensation starts to reduce. This is confirmed by a theoretical estimation (shown in blue). To obtain this estimation the normalized difference in nonlinear distortion from FWM [64] was computed for all possible subcarrier triplets whose nonlinear distortions fall on either the carrier or its conjugate. The sum of these nonlinearity compensation errors was used to estimate the level to which inter subcarrier nonlinearity is suppressed in the calculation of nonlinear noise. To give an upper bound on the compensation performance we assume that parametric noise amplification [69] is not compensated by the conjugates. The optimum signal to noise ratio was used to calculate the BER for subcarriers with and without a phase conjugate assuming that coherent superposition enabled a 3dB enhancement in signal to noise ratio [55]. Finally the mean BER was used to calculate the required SNR to give the same performance without conjugate pilots. The curve fit between 33% and 50% conjugates assumes a linear interpolation of the nonlinear compensation error, but is dominated by the increasing effectiveness of the coherent superposition. An excellent fit is observed over a wide range of configurations with the exception of the case where 50% of the subcarriers are phase conjugate pilots. We believe that this error is due to a reduced benefit of coherent superposition when the noise fields are no longer statistically independent, due to their parametric amplification by the signal. In a practical system, a minimum overhead for CPE (4-10%) would be required, and this overhead may be used to provide a certain level of nonlinear compensation without additional overhead.

2.2.5.3 Experimental demonstration

The experimental set-up is shown in Figure 2.60. It comprised a laser grid of five standard DFBs on 100 GHz grid which were substituted in turn by a 100 kHz linewidth laser. The DFBs are located between 193.5 to 193.9 THz. Additional loading channels (10 GHz of bandwidth) were generated using an ASE source which were spectrally shaped using a wavelength selective switch (WSS) [72]. The twenty loading channels were spread symmetrically around the test wavelengths so that the total bandwidth of the transmitted signal was 2.5 THz. A wideband filter was used to filter out of band ASE noise at the transmitter. The transmission path was an acousto-optic modulator (AOM) based re-circulating loop consisting of 4 x 100 km spans of Sterlite OH-LITE (E) fiber, having 18.9 to 19.5 dB insertion loss. The loop switch was located in the mid-stage of the first EDFA and a gain flattening filter (GFF) was placed in the mid stage of the third EDFA. After propagation the signal was filtered using a 4.2 nm flat topped filter and coherently detected. The received electrical signals were then sampled by a real-time oscilloscope at 80 GS/s and processed offline in MATLAB.

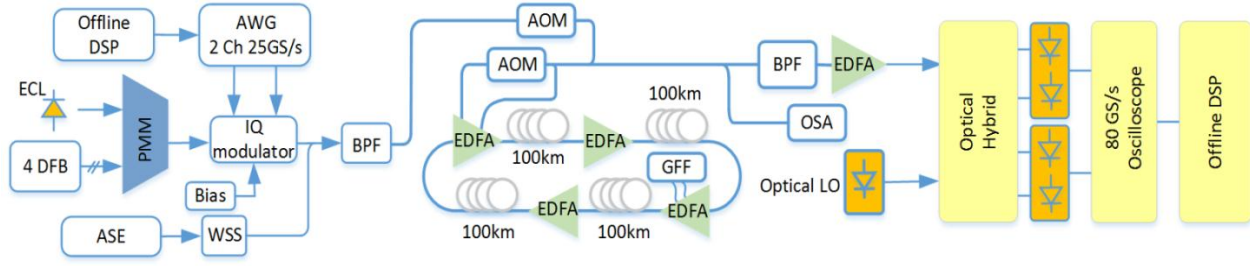


Figure 2.60 Schematic of experimental setup of WDM CO-OFDM transmission with PCPs for fiber nonlinearity compensation. ECL: external cavity laser, PMM: polarization maintaining multiplexer, WSS: Wavelength Selective Switch, DFB: distributed feedback laser, BPF: band-pass filter (optical), AOM: acousto-optic modulator, GFF: gain flatten filter, OSA: optical spectrum analyzer, LO: local oscillator

The OFDM signal (400 symbols each of 20.48 ns length, 2% cyclic prefix) encoded with QPSK modulation format was generated offline in MATLAB using an IFFT size of 512, where 210 subcarriers were filled with data and the remainder zeros giving a line rate of 20 Gb/s (18.2 Gb/s after cyclic prefix and FEC overhead are removed). When 25 %, 33.3 % and 50 % of OFDM subcarriers are transmitted with its PCPs the net data rates were 13.65 Gb/s, 12.12 Gb/s and 9.1 Gb/s respectively. In this work, in order to maximize the similarity between nonlinear phase noises on data subcarrier and PCP, data subcarrier and its PCP were placed next to each other. The DSP at the receiver included chromatic dispersion compensation using an overlapped frequency domain equalizer with overlap-and-save method, channel estimation and equalization with the assistance of initial training sequence (2 training symbols every 100 symbols), CPE compensation with the help of the PCPs [67] or 16 pilot subcarriers if PCPs were not transmitted, fiber nonlinearity compensation as described above, and symbol detection. The system performance was evaluated directly from the BER by processing 10 recorded traces ($\sim 10^6$ bits). The measured BER is then converted to an equivalent “Gaussian noise” Q-factor in dB using the expression [73, 74]:

$$Q_{BER} = 20 \log[\sqrt{2} \cdot \text{erfc}^{-1}(2BER)] \quad (4)$$

Where erfc^{-1} is the inverse complementary error function.

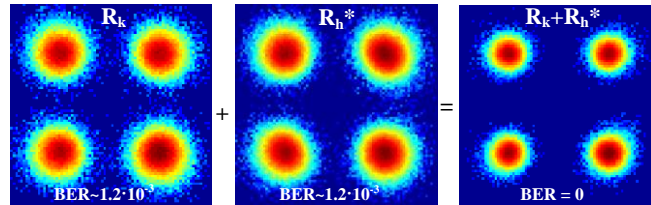


Figure 2.61 Cancellation of the nonlinear distortions by CS of subcarriers with its counterpart PCPs in WDM CO-OFDM transmission, 800 km of distance, the launch power (per/ch) was 0 dBm.

The effectiveness of the proposed PCP compensation scheme for fiber nonlinearity compensation in CO-OFDM is shown in Figure 2.61, for the center channel. Before coherent superposition, the measured BER was $\sim 1.2 \cdot 10^{-3}$. However, after coherent superposition error free transmission was observed. This result clearly indicates that a substantial fraction of the nonlinear distortion, including both intra and inter-channel distortions, can be effectively compensated using coherent superposition of the data carrying subcarriers and the PCPs.

It can be seen in the Figure 2.62(a), that by transmitting 50% of OFDM subcarriers as PCPs a dramatic (~ 4 dB) improvement in the system’s Q-factor was achieved (after 3200 km of the transmission distance), which agrees well with the simulation result and is also comparable with results achieved with the conventional PC-TW technique [55]. The optimum launch power was increased by around 1 dB.

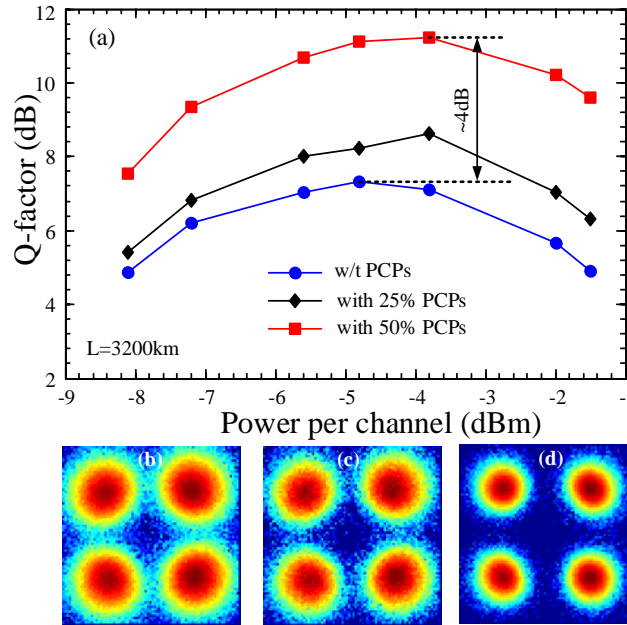


Figure 2.62 Q-factor of the center channel as a function of the launch power in system with and without PCPs for fiber nonlinearity compensation (a) and constellation diagrams at $P_{in} = -1.5$ dBm for the cases of without PCPs (b) and with 25%, 50% of PCPs (c and d) respectively

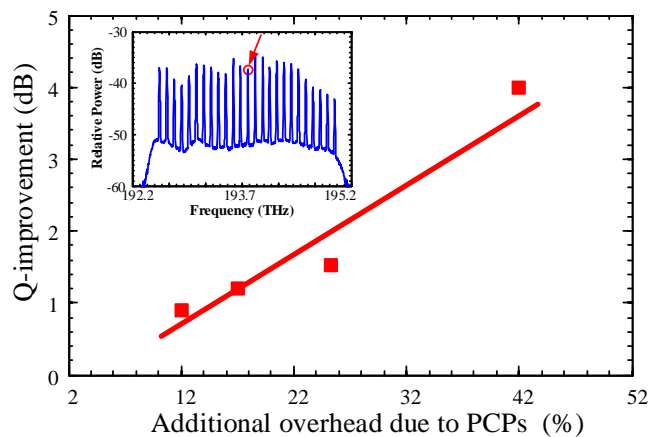


Figure 2.63 Performance gain as a function of the additional overhead due to PCPs for the center channel, after 3200 km of distance. Without PCPs, an overhead of ~8% was required for CPE compensation.

As mentioned before, the overhead can be reduced by using a smaller number of PCP. Specifically, one PCP can be used for 2, 3, 4 or more data subcarriers at the cost of 33 %, 25 %, 20 % or smaller overhead respectively. When the PCP overhead was reduced to 25%, a performance improvement of around 1.5 dB was still achieved (Figure 2.62(a)). This result confirms the possibility of using one PCP to compensate the nonlinear distortions of several data carrying subcarriers. Figure 2.63 plots the Q-factor improvement as a function of the additional overhead due to the PCP, showing the trade-off between PCP overhead and performance gain. Since when PCPs were not transmitted, 8% of OFDM subcarriers were allocated for phase noise estimation, the additional overhead for nonlinear compensations were 12 %, 17 %, 25 % and 42 % and the performance gains were 0.9, 1.2, 1.5 and 4dB respectively. This result clearly shows the flexibility of the proposed PCP fiber nonlinearity compensation technique, allowing the number of PCP to be chosen to meet the performance requirement.

2.2.5.4 Discussion

We have demonstrated a novel fiber nonlinearity compensation technique for CO-OFDM systems based on the transmission of phase-conjugated pilots, which can be effectively applied in both single polarization and PMD systems, in both single channel and WDM systems. The effectiveness of this technique was demonstrated by numerical simulation and laboratory experiment, showing that a direct improvement of up to 4 dB can be achieved. In addition, with this scheme, one phase conjugated pilot can be used to compensate the nonlinear distortions on several subcarriers and thus, the overhead due to phase conjugated pilots can be chosen according to the requirement of a specific application, offering the highest flexibility in implementations.

2.2.6 References

1. Z. Benyuan, D. Peckham, Y. Man, T. Taunay, and J. Fini, "Recent progress in transmission fibers for capacity beyond 100-Tbit/s," in Optical Fiber Communication Conference and Exposition (OFC/NFOEC), 2012 and the National Fiber Optic Engineers Conference(2012), pp. 1-3.
2. Z. Jian, and A. Ellis, "Advantage of Optical Fast OFDM Over OFDM in Residual Frequency Offset Compensation," Photonics Technology Letters, IEEE 24, 2284-2287 (2012).
3. C. Simin, Y. Ma, and W. Shieh, "Multiband Real-Time Coherent Optical OFDM Reception up to 110 Gb/s with 600-km Transmission," Photonics Journal, IEEE 2, 454-459 (2010).
4. X. Zhou, K. Long, R. Li, X. Yang, and Z. Zhang, "A simple and efficient frequency offset estimation algorithm for high-speed coherent optical OFDM systems," Opt. Express 20, 7350-7361 (2012).
5. Y. Chun Ju, L. Xiang, S. Chandrasekhar, K. Yong-Hwan, K. Jong-Hoi, J.-S. Choe, C. Kwang-Seong, and N. Eun-Soo, "An efficient and frequency-offset-tolerant channel estimation and synchronization method for PDM CO-OFDM transmission," in Optical Communication (ECOC), 2010 36th European Conference and Exhibition on(2010), pp. 1-3.
6. Barbieri, G. Colavolpe, T. Foggi, E. Forestieri, and G. Prati, "OFDM versus Single-Carrier Transmission for 100 Gbit/s Optical Communication," Lightwave Technology, Journal of 28, 2537-2551 (2010).
7. N. Kaneda, Y. Qi, L. Xiang, S. Chandrasekhar, W. Shieh, and Y.-k. Chen, "Real-Time 2.5 GS/s Coherent Optical Receiver for 53.3-Gb/s Sub-Banded OFDM," Lightwave Technology, Journal of 28, 494-501 (2010).
8. C. Simin, Y. Qi, and W. Shieh, "Demonstration of 12.1-Gb/s single-band real-time coherent optical OFDM reception," in Optoelectronics and Communications Conference (OECC), 2010 15th(2010), pp. 472-473.
9. T. Li, Y. Jianjun, Z. Junwen, S. Yufeng, and C. Nan, "Reduction of Intercarrier Interference Based on Window Shaping in OFDM RoF Systems," Photonics Technology Letters, IEEE 25, 851-854 (2013).
10. W. Kozek, and A. F. Molisch, "On the eigenstructure of underspread WSSUS channels," in Signal Processing Advances in Wireless Communications, First IEEE Signal Processing Workshop on(1997), pp. 325-328.
11. D. Roque, and C. Siclet, "Performances of Weighted Cyclic Prefix OFDM with Low-Complexity Equalization," Communications Letters, IEEE 17, 439-442 (2013).
12. W. Kozek, and A. F. Molisch, "Nonorthogonal pulses shapes for multicarrier communications in doubly dispersive channels," Selected Areas in Communications, IEEE Journal on 16, 1579-1589 (1998).
13. D. Roque, "Modulations multiporteuses WCP-OFDM: evaluation des performances en environnement radiomobile," in PhD Dissertation, (Universite de Grenoble, 2012).
14. J. Proakis, and M. Salehi, Digital Communications (McGraw-Hill, 2006).
15. D. Pinchon, and P. Siohan, "Closed-Form Expressions of Optimal Short PR FMT Prototype Filters," in Global Telecommunications Conference (GLOBECOM 2011), 2011 IEEE(2011), pp. 1-5.

16. P. Siohan, C. Siclet, and N. Lacaille, "Analysis and design of OFDM/OQAM systems based on filterbank theory," *Signal Processing, IEEE Transactions on* 50, 1170-1183 (2002).
17. S. Randel, S. Adhikari, and S. L. Jansen, "Analysis of RF-Pilot-Based Phase Noise Compensation for Coherent Optical OFDM Systems," *Photonics Technology Letters, IEEE* 22, 1288-1290 (2010).
18. C. Simin, Y. Qi, Y. Ma, and W. Shieh, "Real-Time Multi-Gigabit Receiver for Coherent Optical MIMO-OFDM Signals," *Lightwave Technology, Journal of* 27, 3699-3704 (2009).
19. A.Sano, H. Masuda, E. Yoshida, T. Kobayashi, E. Yamada, Y. Miyamoto, F. Inuzuka, Y. Hibino, Y. Takatori, K. Hagimoto, T. Yamada, and Y. Sakamaki, "30 x 100-Gb/s all-optical OFDM transmission over 1300 km SMF with 10 ROADM nodes," in *Optical Communication - Post-Deadline Papers (published 2008), 2007 33rd European Conference and Exhibition of (2007)*, pp. 1-2.
20. W. Shieh, Q. Yang, and Y. Ma, "107 Gb/s coherent optical OFDM transmission over 1000-km SSMF fiber using orthogonal band multiplexing," *Opt. Express* 16, 6378-6386 (2008).
21. Q. Dayou, H. Ming-Fang, Z. Shaoliang, P. Nan Ji, S. Yin, F. Yaman, E. Mateo, W. Ting, Y. Inada, T. Ogata, and Y. Aoki, "Transmission of 115G PDM-8QAM-OFDM channels with 4bits/s/Hz spectral efficiency over 10,181km," in *Optical Communication (ECOC), 2011 37th European Conference and Exhibition on (2011)*, pp. 1-3.
22. R. Schmogrow, B. Nebendahl, M. Winter, A. Josten, D. Hillerkuss, S. Koenig, et al., "Error Vector Magnitude as a Performance Measure for Advanced Modulation Formats," *Photonics Technology Letters, IEEE*, vol. 24, pp. 61-63, 2012.
23. R. A. Shafik, S. Rahman, and R. Islam, "On the Extended Relationships Among EVM, BER and SNR as Performance Metrics," in *Electrical and Computer Engineering, 2006. ICECE '06. International Conference on, 2006*, pp. 408-411.
24. A. Carena, G. Bosco, V. Curri, P. Poggiolini, M. T. Taiba, and F. Forghieri, "Statistical characterization of PM-QPSK signals after propagation in uncompensated fiber links," in *Optical Communication (ECOC), 2010 36th European Conference and Exhibition on, 2010*, pp. 1-3.
25. Z. Fan, L. Yazhi, W. Yandan, L. Li, Z. Lixin, C. Zhangyuan, et al., "Experimental Comparison of Different BER Estimation Methods for Coherent Optical QPSK Transmission Systems," *Photonics Technology Letters, IEEE*, vol. 23, pp. 1343-1345, 2011.
26. S. T. Le, K. J. Blow, V. K. Menzentsev, and S. K. Turitsyn, "Comparison of numerical bit error rate estimation methods in 112Gbs QPSK CO-OFDM transmission," in *Optical Communication (ECOC 2013), 39th European Conference and Exhibition on, 2013*, pp. 1-3.
27. K. Kikuchi and S. Tsukamoto, "Evaluation of Sensitivity of the Digital Coherent Receiver," *Lightwave Technology, Journal of*, vol. 26, pp. 1817-1822, 2008.
28. L. Son Thai, T. Kanesan, E. Giacomidis, N. J. Doran, and A. D. Ellis, "Quasi-Pilot Aided Phase Noise Estimation for Coherent Optical OFDM Systems," *Photonics Technology Letters, IEEE*, vol. 26, pp. 504-507, 2014.
29. Z. Wang, Y. Qiao, Y. Xu, and Y. Ji, "Statistical characterization of the nonlinear noise in 2.8 Tbit/s PDM-16QAM CO-OFDM system," *Optics Express*, vol. 21, pp. 18034-18042, 2013/07/29 2013.
30. X. Chen and W. Shieh, "Closed-form expressions for nonlinear transmission performance of densely spaced coherent optical OFDM systems," *Optics Express*, vol. 18, pp. 19039-19054, 2010/08/30 2010.
31. S. T. Le, K. J. Blow, V. K. Mezentsev, and S. K. Turitsyn, "Bit Error Rate Estimation Methods for QPSK CO-OFDM Transmission," *Lightwave Technology, Journal of*, vol. 32, pp. 2951-2959, 2014.
32. R. F. Pawula, S. O. Rice, and J. Roberts, "Distribution of the Phase Angle Between Two Vectors Perturbed by Gaussian Noise," *Communications, IEEE Transactions on*, vol. 30, pp. 1828-1841, 1982.

33. S. Wu and Y. Bar-Ness, "OFDM systems in the presence of phase noise: consequences and solutions," Communications, IEEE Transactions on, vol. 52, pp. 1988-1996, 2004.
34. W. Shieh, Q. Yang, and Y. Ma, "107 Gb/s coherent optical OFDM transmission over 1000-km SSMF fiber using orthogonal band multiplexing," Optics Express, vol. 16, pp. 6378-6386, 2008.
35. S. T. Le, T. Kanesan, M. McCarthy, E. Giacomidis, I. Phillips, M. F. Stephens, et al., "Experimental Demonstration of Data-dependent Pilot-aided Phase Noise Estimation for CO-OFDM," OFC2014, paper. Tu3G.4.
36. M. E. Mousa-Pasandi and D. V. Plant, "Zero-overhead phase noise compensation via decision-directed phase equalizer for coherent optical OFDM," Optics Express, vol. 18, pp. 20651-20660, 2010.
37. T. Pfau, S. Hoffmann, and R. Noe, "Hardware-Efficient Coherent Digital Receiver Concept With Feedforward Carrier Recovery for M-QAM Constellations," Lightwave Technology, Journal of, vol. 27, pp. 989-999, 2009.
38. M. E. McCarthy, N. M. Suibhne, S. T. Le, P. Harper, and A. D. Ellis, "High Spectral Efficiency Transmission Emulation for Non-Linear Transmission Performance Estimation for High Order Modulation Formats," ECOC2014, paper P5.7.
39. M. E. Mousa-Pasandi and D. V. Plant, "Data-aided adaptive weighted channel equalizer for coherent optical OFDM," Optics Express, vol. 18, pp. 3919-3927, 2010/02/15 2010.
40. M. E. Mousa-Pasandi and D. V. Plant, "Zero-overhead phase noise compensation via decision-directed phase equalizer for coherent optical OFDM," Optics Express, vol. 18, pp. 20651-20660, 2010/09/27 2010.
41. S. Randel, S. Adhikari, and S. L. Jansen, "Analysis of RF-Pilot-Based Phase Noise Compensation for Coherent Optical OFDM Systems," Photonics Technology Letters, IEEE, vol. 22, pp. 1288-1290, 2010.
42. W. Shieh, "Maximum-Likelihood Phase and Channel Estimation for Coherent Optical OFDM," Photonics Technology Letters, IEEE, vol. 20, pp. 605-607, 2008.
43. C. Shengjiao, K. Pooi Yuen, and Y. Changyuan, "Decision-Aided, Pilot-Aided, Decision-Feedback Phase Estimation for Coherent Optical OFDM Systems," Photonics Technology Letters, IEEE, vol. 24, pp. 2067-2069, 2012.
44. S. Wu and Y. Bar-Ness, "A phase noise suppression algorithm for OFDM-based WLANs," Communications Letters, IEEE, vol. 6, pp. 535-537, 2002.
45. L. Barletta, M. Magarini, and A. Spalvieri, "Staged demodulation and decoding," Optics Express, vol. 20, pp. 23728-23734, 2012/10/08 2012.
46. J. Eudes, "Modulation method with insertion of semi-pilot symbols," US Patent 7692485, 2010.
47. M. G. Taylor, "Phase Estimation Methods for Optical Coherent Detection Using Digital Signal Processing," Lightwave Technology, Journal of, vol. 27, pp. 901-914, 2009.
48. S. T. Le, K. J. Blow, V. K. Menzentsev, and S. K. Turitsyn, "Comparison of numerical bit error rate estimation methods in 112Gbs QPSK CO-OFDM transmission," in Optical Communication (ECOC 2013), 39th European Conference and Exhibition on, 2013, pp. 1-3
49. E. Ip and J. M. Kahn, "Compensation of Dispersion and Nonlinear Impairments Using Digital Backpropagation," Journal of Lightwave Technology, vol. 26, pp. 3416-3425, 2008/10/15 2008.
50. C. Xi, L. Xiang, S. Chandrasekhar, B. Zhu, and R. W. Tkach, "Experimental demonstration of fiber nonlinearity mitigation using digital phase conjugation," presented in OFC 2012, pp. 1-3.

51. S. L. Jansen, D. Van den Borne, B. Spinnler, S. Calabro, H. Suche, P. M. Krummrich, et al., "Optical phase conjugation for ultra long-haul phase-shift-keyed transmission," *Lightwave Technology, Journal of*, vol. 24, pp. 54-64, 2006.
52. D. M. Pepper and A. Yariv, "Compensation for phase distortions in nonlinear media by phase conjugation," *Optics Letters*, vol. 5, pp. 59-60, 1980/02/01 1980.
53. I. Phillips, M. Tan, M. F. Stephens, M. McCarthy, E. Giacomidis, S. Sygletos, et al., "Exceeding the Nonlinear-Shannon Limit using Raman Laser Based Amplification and Optical Phase Conjugation," *OFC*, San Francisco, California, 2014, p. M3C.1.
54. S. Watanabe, S. Kaneko, and T. Chikama, "Long-Haul Fiber Transmission Using Optical Phase Conjugation," *Optical Fiber Technology*, vol. 2, pp. 169-178, 4// 1996.
55. X. Liu, R. A. Chraplyvy, P. J. Winzer, W. R. Tkach, and S. Chandrasekhar, "Phase-conjugated twin waves for communication beyond the Kerr nonlinearity limit," *Nat Photon*, vol. 7, pp. 560-568, 2013.
56. T. Yoshida, T. Sugihara, K. Ishida, and T. Mizuochi, "Spectrally-efficient Dual Phase-Conjugate Twin Waves with Orthogonally Multiplexed Quadrature Pulse-shaped Signals," in *Optical Fiber Communication Conference*, San Francisco, California, 2014, p. M3C.6.
57. S. T. Le, E. Giacomidis, N. Doran, A. D. Ellis, and S. K. Turitsyn, "Phase-conjugated Subcarrier Coding for Fiber Nonlinearity Mitigation in CO-OFDM Transmission," presented at the *ECOC*, Cannes, France, paper We.3.3.2, 2014.
58. X. Liu, A. R. Chraplyvy, R. W. Tkach, and P. J. Winzer, "Communication Through Phase-Conjugated Optical Variants," *USA Patent*, 2012.
59. Y. Tian, Y.-K. Huang, S. Zhang, P. R. Prucnal, and T. Wang, "Demonstration of digital phase-sensitive boosting to extend signal reach for long-haul WDM systems using optical phase-conjugated copy," *Optics Express*, vol. 21, pp. 5099-5106, 2013/02/25 2013.
60. X. Yi, X. Chen, D. Sharma, C. Li, M. Luo, Q. Yang, et al., "Digital coherent superposition of optical OFDM subcarrier pairs with Hermitian symmetry for phase noise mitigation," *Optics Express*, vol. 22, pp. 13454-13459, 2014/06/02 2014.
61. S. T. Le, M. E. McCarthy, N. M. Suibhne, A. D. Ellis, and S. K. Turitsyn, "Phase-conjugated Pilots for Fiber Nonlinearity Compensation in CO-OFDM Transmission," presented at the *ECOC*, Cannes, France, paper We.2.3.1, 2014.
62. S. T. Le, K. Blow, and S. Turitsyn, "Power pre-emphasis for suppression of FWM in coherent optical OFDM transmission," *Optics Express*, vol. 22, pp. 7238-7248, 2014/03/24 2014.
63. F. Buchali, R. Dischler, and X. Liu, "Optical OFDM: A promising high-speed optical transport technology," *Bell Labs Technical Journal*, vol. 14, pp. 125-146, 2009.
64. D. A. Cleland, A. D. Ellis, and C. H. F. Sturrock, "Precise modelling of four wave mixing products over 400 km of step-index fiber," *Electronics Letters*, vol. 28, pp. 1171-1173, 1992.
65. B. Inan, S. Randel, S. L. Jansen, A. Lobato, S. Adhikari, and N. Hanik, "Pilot-tone-based nonlinearity compensation for optical OFDM systems," presented in *ECOC 2010*, pp. 1-3.
66. X. Liu, S. Chandrasekhar, P. J. Winzer, A. R. Chraplyvy, R. W. Tkach, B. Zhu, et al., "Scrambled coherent superposition for enhanced optical fiber communication in the nonlinear transmission regime," *Optics Express*, vol. 20, pp. 19088-19095, 2012/08/13 2012.
67. S. T. Le, T. Kanesan, M. McCarthy, E. Giacomidis, I. Phillips, M. F. Stephens, et al., "Experimental Demonstration of Data-dependent Pilot-aided Phase Noise Estimation for CO-OFDM," in *Optical Fiber Communication Conference*, San Francisco, California, 2014, p. Tu3G.4.

68. L. Son Thai, T. Kanesan, E. Giacomidis, N. J. Doran, and A. D. Ellis, "Quasi-Pilot Aided Phase Noise Estimation for Coherent Optical OFDM Systems," *Photonics Technology Letters, IEEE*, vol. 26, pp. 504-507, 2014.
69. D. Rafique and A. D. Ellis, "Impact of signal-ASE four-wave mixing on the effectiveness of digital back-propagation in 112 Gb/s PM-QPSK systems," *Optics Express*, vol. 19, pp. 3449-3454, 2011/02/14 2011.
70. S. L. Jansen, I. Morita, T. C. W. Schenk, and H. Tanaka, "121.9-Gb/s PDM-OFDM Transmission With 2-b/s/Hz Spectral Efficiency Over 1000 km of SSMF," *Lightwave Technology, Journal of*, vol. 27, pp. 177-188, 2009.
71. A. D. Ellis and W. A. Stallard, "Four wave mixing in ultra long transmission systems incorporating linear amplifiers," in *Non-Linear Effects in Fiber Communications, IEE Colloquium on*, 1990, pp. 6/1-6/4.
72. M. E. McCarthy, N. M. Suibhne, S. T. Le, P. Harper, and A. D. Ellis, "High Spectral Efficiency Transmission Emulation for Non-Linear Transmission Performance Estimation for High Order Modulation Formats," presented at the ECOC, Cannes, France, paper P.5.7, 2014.
73. S. T. Le, K. J. Blow, V. K. Menzentsev, and S. K. Turitsyn, "Comparison of numerical bit error rate estimation methods in 112Gbs QPSK CO-OFDM transmission," in *Optical Communication (ECOC 2013), 39th European Conference and Exhibition on*, 2013, pp. 1-3.
74. S. T. Le, K. J. Blow, V. K. Mezentsev, and S. K. Turitsyn, "Bit Error Rate Estimation Methods for QPSK CO-OFDM Transmission," *Lightwave Technology, Journal of*, vol. 32, pp. 2951-2959, 2014.

3 Summary and Conclusions

In this deliverable we presented BER over SNR/OSNR measurements of the candidates of the flexible transceiver. We started with N-WDM, here we used a noise-loading stage to measure the BER over SNR performance. For pulse shaping, a SRRC filter was used at the transmitter and the receiver. Three different ROF were used to characterize the transmission performance. It was observed that smaller ROF had a higher SNR penalty and this was explained by the associated eye diagrams. We observed a penalty for 16QAM and higher symbol rate due to the fact that for higher frequencies the ENOB of the converters is reduced. We showed the SNR penalty of QPSK and 16QAM with ROF=0.05, 0.125, and 0.25 to the theoretical limit. This was followed by the evaluation of N-FDM. Here we used 5 sub-channels. It was observed that the outer channels had lower performance due to the low pass characteristic of the devices. We presented our newly developed phase recovery algorithm and tested it to LPN and AWGN influence. Implemented block length was 32 and 64 symbols. It is observed that longer blocks perform worse for strong LPN but give advantage for AWGN. The hardware implementation runs up to 38 Gb/s. For real-time timing recovery we presented our technique that uses an adaptive filter in the time domain to correct the wrong sampling phase and the Gardner estimation algorithm to estimate the timing error.

We also showed that multi-tap equalization improves the performance of F-OFDM. We presented experimental results where 16QAM was transmitted over a distance of 1020 km. The studies showed that the introduced multi-tap equalization is more effective for F-OFDM than for C-OFDM. Here as well we measured BER over OSNR and the performance decrease due to CFO. In our test-bed with G.655 and G.652 fiber we measured 16QAM MB-OFDM with 200 Gbit/s and QPSK MB-OFDM with 100 Gbit/s. The implementation penalty between the two formats was as low as 0.8 dB. The BER over input power measurements showed ideal input power of -2 dBm for G.655 fiber and 0 dBm for G.652 fiber. As an alternative to the already shown modulation formats, offset-16QAM OFDM was presented. Experimental results for 38 Gbit/s were shown and the performance evaluation over OSNR and CD was presented.

A new pulse-shaping method to reduce the penalty of residual carrier frequency offset for CO-OFDM was introduced. Here two approaches were given. One is based on the time-frequency localization maximization (TFL) and the other based on the out-of-band energy minimization (OBE). The results showed a CFO of 1.25 MHz as the threshold. Below that value, TFL performs better and above OBE is superior. To reduce the time for BER calculation, good estimation techniques are needed to estimate the BER for high signal qualities. For this we presented estimation methods for CO-OFDM. The best estimation was based on the probability density function of the received QPSK symbols' phase. LPN for long symbol duration of CO-OFDM is harmful, it introduces common phase errors and intercarrier interference. Therefore, reliable LPN tracking and compensation are needed. We presented a blind phase noise compensation based on three test phases. Additionally, a quasi-pilot aided method for phase noise estimation was shown. Here we found that only 4 pilot subcarriers are needed for effective phase noise compensation if they are set in correlation with data subcarriers. To enable nonlinearity compensation we presented in the last section phase-conjugated pilots as a promising candidate.